AVOIDING SNAP-THROUGH INSTABILITY OF POST-BUCKLED BEAMS USING PIEZOELECTRIC ACTUATION

by

HANING XIU

(Under the Direction of R. Benjamin Davis)

ABSTRACT

Snap-through instability is a familiar phenomenon in structural mechanics. Post-buckled and curved structures experience dramatic snap-through instabilities when external loads from mechanical, fluid, or thermal environments result in a loss of local stability and a violent jump to a remote stable equilibrium. Fatigue caused by snap-through is a concern in many engineered systems because of the large stress reversals involved. Snap-through is typically avoided by designing structures to be robust in response to complex and/or uncertain loading environments. However, these traditional ways of ensuring stability are often at odds with other important design objectives, such as minimizing weight.

This study theoretically and experimentally investigates the strategic actuation of lightweight and flexible piezoelectric material to change the loads required to initiate snap-through of clamped-clamped post-bucked beams. It then studies the possibility of using piezoelectric actuation to traverse stable transitions between remote equilibria, thus avoiding snap-through behavior altogether. It also finds the changes of natural frequencies and mode shapes of post-buckled beams during the stable transitions. Finally, the study theoretically and experimentally identifies actuation strategies that stabilize equilibrium shapes of third- and fourth-order.

It is anticipated that the results of this study can be used to design new smart structures that have enhanced stability in the face of onerous loading environments. One possibility would be to embed piezoelectric actuators into advanced composite materials to enhance their stability without unduly sacrificing weight. Actuation can be used to enhance stability or alter structural shape. When not actuated, the piezoelectric elements could be used as health monitoring sensors or energy harvesters. The present theoretical model, which is cast in non-dimensional terms, enables a more general view of what is possible with the piezoelectric actuation and will allow researchers to more easily discern whether a candidate structure will be sufficiently amenable to piezoelectric actuation.

INDEX WORDS: Post-buckled beams, Piezoelectric actuation, Elastica theory, Snap-through, Stable transition, Mode shape, Higher-order shape

Avoiding Snap-Through Instability of Post-buckled Beams Using Piezoelectric Actuation

by

Haning Xiu

B.S., Nanjing University of Aeronautics and Astronautics, 2012

M.S., Beijing Institute of Technology, 2015

A Dissertation Submitted to the Graduate Faculty of The University of Georgia in Partial Fulfillment of the Requirements for the Degree

Doctor of Philosophy

Athens, Georgia

2020

AVOIDING SNAP-THROUGH INSTABILITY OF POST-BUCKLED BEAMS

USING PIEZOELECTRIC ACTUATION

by

HANING XIU

Major Professor: R. Benjamin Davis

Committee: Donald J. Leo
Xianqiao Wang
Mi Geum Chorzepa

Electronic Version Approved:

Ron Walcott
Interim Dean of the Graduate School
The University of Georgia
May 2020

Acknowledgements

There are many people that have earned my gratitude for their contribution to my time in graduate school. This dissertation would not have been possible without the aid and support from them. More specifically, I would like to thank four groups of people: my PhD committee members, my lab-mates, funding agencies, and my family.

Foremost, I would like to express my deepest appreciation to each of the members of my PhD Advisory Committee along with the faculty and staff of the College of Engineering at the University of Georgia whom have provided me with educational guidance. Dr. Donald J. Leo, Dr. Xianqiao Wang, and Dr. Mi Geum Chorzepa, served as my committee, gave me plenty of pertinent comments and suggestions on my dissertation, which enriched my research depth and scope. I am extremely grateful to thank Dr. R. Benjamin Davis for giving me this PhD opportunity to extend my education. On the academic level, as my major professor and mentor, he has mentored me on building my academic career—what and how I should do as a young researcher. Especially, he helped me greatly improve my writing ability of academic papers. I am profoundly grateful for his patience, motivation, enthusiasm, and immense knowledge. On a personal level, Dr. Davis treats me as a good friend and we talked about anything.

I would like to extend my sincere thanks to my past and present lab-mates who gave me invaluable help with my research. Ryan Romeo, Eetu Kohtanen, Ben Morris, and others took their efforts to help me setup experiments, debug computational programs, revise research papers, etc. I gratefully acknowledge that the research was supported by funding furnished by the Office of the

Vice President of Research and the College of Engineering at the University of Georgia. I am also grateful to the research and teaching assistantship from the College of Engineering.

Last but not least, I would like to express my deepest gratitude to my family and friends. Nobody has been more important to me in the pursuit of this degree than my wife, Yiwen. We met in 2016 and got married in 2019 at UGA. And we will have fruit of our love soon. Her continuous love and support are with me in whatever I pursue. Thanks should also go to my parents, who silently support me from afar.

Contents

List of Figures

List of Tables

Nomenclature

A_1, B_1, B_2, C_1 Intermediate terms in derivation of energy

a_1, a_2 Fraction of span with, without piezoelectric material

$\mathcal{B}$ Energy stored in the composite

b Beam width

D Electric displacement

d_{33} Piezoelectric constant related to elongation

E Electric field variable

e End shortening

$\boldsymbol{f}$ Objective function vector

$\boldsymbol{g}$ Equilibrium function vector

f Natural frequency

H Heaviside function

h Thickness

I Area moment of inertia

$\boldsymbol{J}$ Jacobian matrix

l Beam length

l_p Spacing between neighboring poles in piezoelectric material

l_Q Distance between the point of applied load and the origin

m moment

$\mathcal{P}$ Potential energy

p Axial reaction force

Q Lateral body-fixed load

q Lateral reaction force

S_p Elastic strain

s Arc-length coordinate

sp_1 Percentage of span between the left support and the beginning of the actuation region

sp_2 Percentage of span between the right support and the end of the actuation region

sp_3 Percentage of span between the left support and the end of the actuation region

T Axial stress

t Time

U Volume

$\boldsymbol{u}, \bar{\boldsymbol{u}}, \hat{\boldsymbol{u}}$ Vectors of variables

V Voltage applied to the piezoelectric material

$\boldsymbol{v}$ Vector of function

W Work done by external force

W_p Internal electrical energy in the piezoelectric material

Y Young's modulus

x, y Cartesian coordinates

y_0 Distance between the neutral axis and the geometric midplane of the substrate

Δy Deflection at the point of loading

α Shooting parameter

Γ Snap-through critical load factor

$\bar{\varepsilon}_{33}^S$ Permittivity at constant strain

δ, δ_0 Midpoint deflection, midpoint deflection in unloaded and unactuated case

ζ Damping

θ Beam angle

μ Mass per unit length

Π Strain energy

ρ Material density

σ Non-dimensional electromechanical coupling

ϕ Mid-point rotation angle

χ Electromechanical coupling coefficient

ψ Electromechanical coupling energy coefficient

ω Natural frequency

SUBSCRIPTS

$_{cr}$ Critical threshold

$_{d}$ Dynamic variable

$_{e}$ Value in static equilibrium

$_{eff}$ Effective

$_{eq}$ Mass equivalent

$_{p}$ Piezoelectric

$_{s}$ Substrate

SUPERSCRIPTS

* Dimensional quantity

Chapter 1

Introduction

1.1 Motivation

Modern engineering structures frequently need to be lightweight yet also able to withstand harsh loading environments. These competing requirements can manifest in structures that operate on the edge of stability. Snap-through is a familiar phenomenon to engineers and non-engineers alike. The startling pop of a cookie sheet baking in an oven is the oft-cited example of how snap-through is encountered in everyday life. Even young children are familiar with snap-through because it is commonly used to make toys that click or jump [1]. Post-buckled and curved structures, with aircraft fuselages [2–4], launch vehicles fairings [5, 6], and submarine hulls [7, 8] being a few examples, experience snap-through instabilities when subject to external loads from mechanical, fluid, or thermal environments. These external loads can cause structures to lose local stability and experience a dramatic jump to a remote stable equilibrium. The large nonlinear deformations and correspondingly large stress reversals associated with snap-through greatly decrease the service life of a structure and can pose a significant constraint on the structural integrity of advanced systems. Since snap-through is a nonlinear phenomenon, reliably predicting it is not trivial, especially when complex geometries, boundary conditions, and loading environments are involved.

Given these difficulties, a lightweight means to enhance the stability of structures by 1) increasing their critical snap-through loads, and/or 2) transitioning between remote equilibria along an entirely stable equilibrium path would be valuable innovations. It has been suggested [9–11] that these two innovations are theoretically possible with the advent of lightweight and highly flexible piezoelectric materials. However, neither idea has been explored in-depth, nor have these ideas been demonstrated experimentally. Addressing this research gap requires a modeling framework that generalizes the complex mechanics of highly deformed electromechanical systems.

A new electromechanically coupled elastica model for highly-deformed piezoelectric structures is developed in this dissertation. It is found that appropriately activated piezoelectric material can increase the snap-through loads of post-buckled beams. Further, through the intelligent actuation of multiple piezoelectric patches, the model demonstrates the possibility of circumventing snap-through altogether by following a stable path between remote equilibria. In addition, the modal behavior of the structure is observed during the stable transition. Higher-order equilibrium shapes of post-buckled beams can also be obtained using multiple piezoelectric patches. Ultimately, this research could enable a class of structures exhibiting enhanced stability in the face of demanding loads, and contribute new modeling approaches to exploit snap-through for the purposes of actuation, morphing, and energy harvesting.

1.2 Snap-Through Instability

Snap-through (or snapping) instability is a venerable topic in structural mechanics, with Timoshenko offering an early reference on the subject [12]. In the canonical example of an elastic arch subject to an increasing lateral point load, the mid-point deflects downward until a local stable equilibrium ceases to exist (point A in Fig. 1.1). The structure then rapidly snaps to a remote stable equilibrium (point B). If the structure is then unloaded, hysteresis is observed as the structure eventually snaps back to the original stable curve (point C). For shallow arches, snap-through occurs at a limit point (i.e., a point of vertical tangency in a deflection-load curve). For deeper arches, a bifurcation point occurs at a load that is lower than the limit point, and the structure will jump to a remote configuration before reaching the limit point [4].

To investigate snap-through behavior, Euler's elastica theory [13] is used in the present work. The elastica has a long history of being used to study the snap-through behavior beginning with Huddleston [14] in 1968. The elastica describes differential equations of post-buckled structures based on the geometrical nonlinear theory of large deflection. A distinct advantage of the elastica formulation is that the modifications required to consider the effects of extensibility [15], self-weight [16], initial imperfections [17], and various boundary conditions [18, 19] are relatively straightforward.

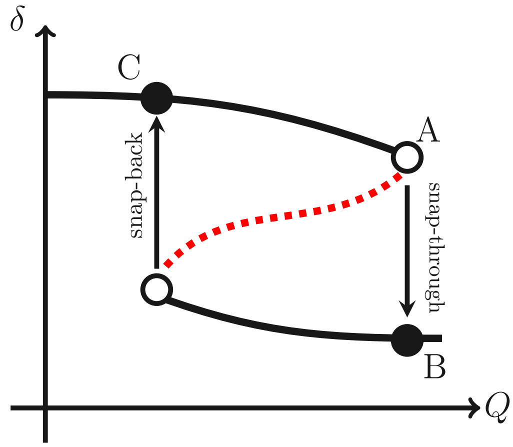

Figure 1.1. Deflection (δ) versus load (Q) diagram illustrating the concept of snap-through instability.

Snap-through remains an active area of research, especially in the context of dynamic loading, bistability, and switching between bistable equilibria. Recent research by Chen and his colleagues have considered the snap-through behavior of suddenly loaded structures [19], dynamic snapping due to step loads [15], and moving point loads [20]. Other researchers considered dynamic snap-through behaviors for MEMS applications [21–24]. Chandra et al. considered the complex nonlinear dynamics of transient snap-through in shallow arches [4], and the use of full-field digital image correlation (DIC) techniques to measure such behavior [25]. Several other efforts have considered bistable mechanisms exhibiting snap-through behavior [26–28].

1.3 Elastica Theory

The elastica theory, developed by Leonhard Euler, allows for very large scale elastic deflections of structures. The history of the elastica traces back to its first solution by James Bernoulli in 1691. The complete solution is most commonly attributed to Euler in 1744 because of his compelling mathematical treatment and illustrations [13]. The derivation of Euler's equations can also be found in Levien's report [13].

Huddleston [14, 29] used the shooting method to study the buckling of prismatic doubly-hinged arches of several height-to-span ratios under vertical concentrated load at the crown [30]. In 1974, DaDeppo and

Schmidt [31] investigated buckling behaviors of large prebuckling deflections of hingeless circular arches based on Euler's nonlinear theory of the inextensible curved elastica. It is found that non-shallow hingeless arches may buckle by either asymmetrical sidesway or symmetrical snap-through, depending on the relative magnitudes of the point load and the weight of the arch. Wang [32] wrote a review of the heavy (i.e., self-weight is included) elastica that included all relevant literature describing models of buckling, post-buckling and large deformation.

Later, extensibility was included in the elastica to solve buckling and post-buckling problems. Magnusson et al. [33] investigated snap-though behaviors based on the extensible elastica. Due to the extensibility of the beam axis, it is shown that the buckling load of the extensible elastica solution depends on the slenderness, and that for small slenderness, the bifurcation point becomes unstable. Chen and Tsao [34] studied the static snapping load of a hinged buckled beam under a midpoint force using three approaches—small-deformation theory, inextensible elastica, and extensible elastica. The results demonstrated that small-deformation theory fails to predict the static snapping load accurately in the large-deformation range, inextensible elastica fails to predict the static critical load satisfactorily in the small-deformation range, and only the extensible elastica theory can predict the static snapping load accurately both in the small- and large-deformation ranges.

1.4 Control of Structural Instability

Post-buckled and curved structures may experience snap-through instabilities from external loads. These external loads lead structures to lose local stability and violently jump to a remote stable equilibrium. Fracture and fatigue caused by snap-through is a concern in many engineered systems because of the large stress reversals involved. The large stress reversals decrease a structure's service life and pose constraints on the design of engineered systems. Snap-through is typically avoided by designing structures to be robust in response to complex and/or uncertain loading environments. However, these traditional ways of ensuring stability are often at odds with other important design objectives, such as minimizing weight.

External loads from mechanical, fluid, and thermal environments can induce snap-through instability by exceeding a critical snap-through load. Lightweight and flexible materials, such as piezoelectric materials or materials with thermo-mechanical properties, can be used to change structural instability. To provide further context for the current work, some background on inducing snap-through instability using external loads is presented, followed by discussions of controlling structural instability using piezoelectric actuation and thermo-mechanical materials.

1.4.1 Control of Structural Instability using External Loading

Chen and Hung [35] used elastica theory to study the snapping load of a buckled beam with large deformation under a point force at the midpoint. They were interested in the critical conditions under which snapping occurs. Three different models of point force are investigated: 1. the midpoint force is fixed on the buckled beam; 2. the point force stays on the central line in space, and 3. the point force is applied on the buckled beam through a rigid bar that is allowed to slide on the central line in space (see Fig. 1.2). They found "in the case when the buckled beam deforms symmetrically, there is no difference between these three models. However, in the case when the buckled beam deforms unsymmetrically, these three load models may predict different results". Later, Chen et al. [15] studied the transient response of a hinged extensible elastica under a step load at the midpoint, though emphasis is placed on the effect of extensibility on the dynamic snapping behavior.

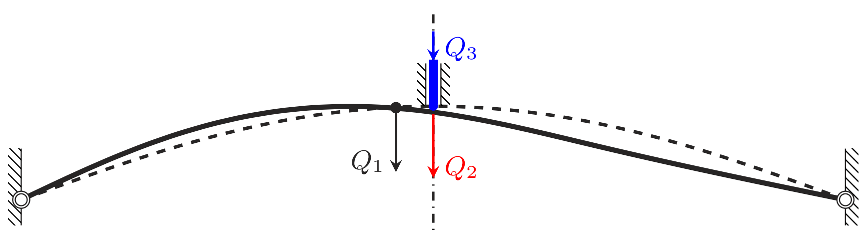

Figure 1.2. Three models of point force from Ref. [35]: mid-point body-fixed force, Q_1, mid-point force on the space central line, Q_2, and point force through a rigid bar to slide on the central line, Q_3.

Dynamic snap-through of shallow arches has also been investigated by Chen and Lin [20]. They studied the dynamic stability of a shallow arch under quasi-static and high-speed moving point forces. The analysis shows there is a static critical load in the sense that no static snap-through will occur as long as the point load is smaller than this critical load. There also exists a dynamic critical snap-through load when the point load travels with a nonzero speed, but it is smaller than the static critical load. There is also a finite speed zone between two critical speeds within which the arch runs the risk of dynamic snap-through. Das and Batra [36] studied symmetry breaking, snap-through instability, and pull-in instability of a bi-stable arch-shaped micro-electro-mechanical system (MEMS) under static and dynamic electric loads. For an electrically actuated MEMS, the applied electric potential has an upper limit. If this limit is exceeded, the elastic restoring force cannot balance the corresponding Coulomb force, and this causes the deformable electrode to collapse onto the rigid one. This phenomenon is called pull-in instability. They found for the dynamic problem, there are two distinct mechanisms of the snap-through instability—the 'direct' and the 'indirect', which are distinguished by the geometric parameters of the arch and the load types. Curves showing the critical load parameters versus arch heights indicate the stable and unstable parameter space, and can help in designing arch-shaped MEMS devices.

Excitation of bistable buckled beams to induce snap-through for the purpose of energy harvesting can be achieved by magnetic loading. Zhu and Zu investigated enhancing harvester functionality under low frequency and small amplitude excitation from a midpoint magnetic force [37]. A non-contact, nonlinear, repulsive magnetic force was applied to the center of a buckled-beam energy harvester, as shown in Fig. 1.3. There are several advantages of using magnetic excitation. For one, the nonlinearity from the magnetic force contributes to large-amplitude nonlinear vibrations, which are preferred for energy harvesting. The local magnetic levitation greatly reduces the operating frequency which is useful for low-frequency applications. Zhu and Zu then proposed a magnet-induced buckled-beam piezoelectric generator for broadband vibration-based energy harvesting at low frequencies. A magnet-induced force is used to compress the beam, and the system is capable of persistent snap-through when excited [38]. A similar work by Jiang et al. [39] shows that when an external mechanical force is applied to the base beneath the permanent magnet array, the magnetic force between the magnets on and off the beam varies periodically and can induce snapping.

1.4.2 Piezoelectric Control of Structural Instability

Piezoelectric materials deform mechanically due to an applied electric charge. They are used in an array of everyday products such as microphones, loud speakers, and remote controls. The most commonly used piezoelectric materials are synthetic ceramics, with lead zirconate titanate (PZT) being a well-known example. These materials tend to be extremely brittle, thus making them ill-suited to conforming to the highly deformed structures of interest here. In 1996, macro fiber composites (MFC) were developed by researchers at NASA [40]. Since they are thin, lightweight, and flexible, MFC are ideal for use in the current experi-

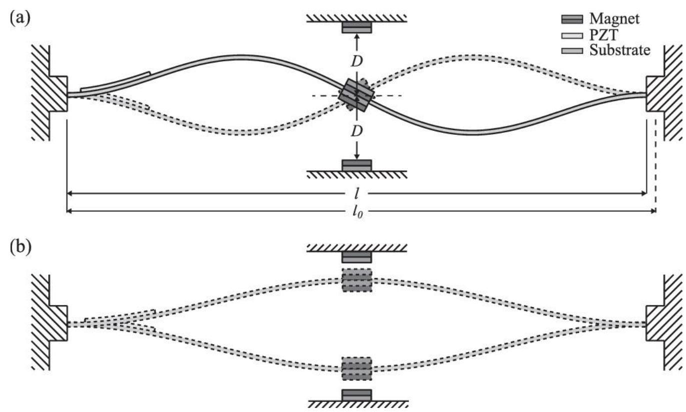

Figure 1.3. Schematic of Zhu and Zu's device with (a) two stable equilibriums and (b) two unstable equilibriums from Ref. [37].

ments. Fig. 1.4 shows the flexibility of an MFC patch. MFC is marketed commercially and has been widely studied in smart material applications (see e.g., Refs. [41–49]).

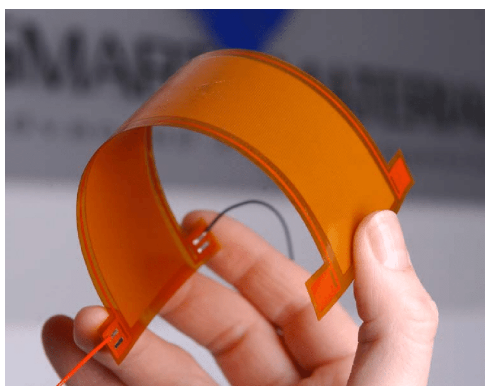

Figure 1.4. MFC actuator with large deformation [50].

Several studies have used piezoelectric material in conjunction with structures exhibiting snap-through; however, most of this research has studied systems in which snap-through is intentionally induced for the purposes of energy harvesting [9,17,51–59], low energy/high displacement actuation [9,60–62] or structural morphing [59,63–68]. Fig. 1.5 show typical applications of curved structures with piezoelectric actuators. A recent review paper by Hu and Burgueño [69] surveys the current landscape of this area of research and concludes "a research trend is emerging to explore the structural systems that can feature multistable events by varying material properties, using hybrid structural/mechanical systems, using hybrid materials, and adding constraints. The search for structural forms to achieve desirable snap-through instabilities is also being assisted by optimization methods, such as topology optimization."

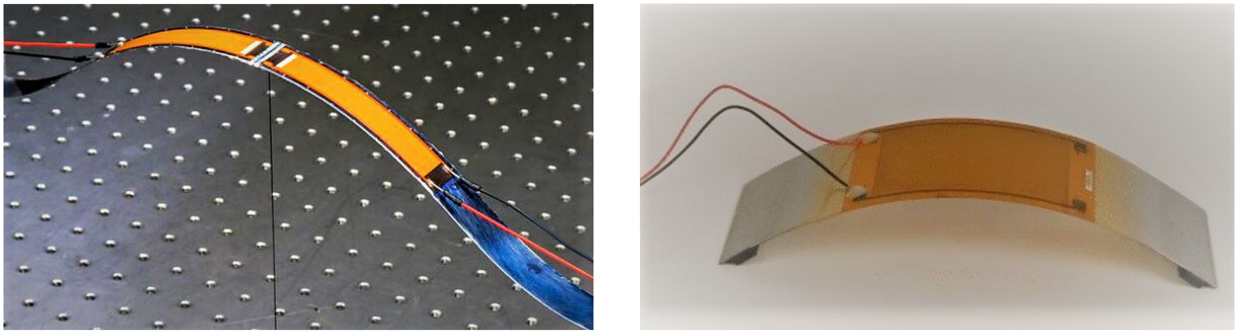

(a) (b)

Figure 1.5. Examples of post-buckled structures with piezoelectric films. (a) MFC bonded to a beam, and (b) MFC bonded to a plate [70].

The concept of using a piezocomposite actuator (MFC) bonded to one side of a substrate to induce snapping of the laminate is proposed by Schultz et al. [60, 61]. The theoretical model of the composite structure is based on the Ritz technique. Prediction of the shapes of the laminate and of the voltage needed to cause snap-through are compared and matched well with experiments. The idea that the critical loads leading to snap-through could be augmented through the use of piezoelectric actuation was mentioned in passing by Arrieta, et al. [71]. This observation was made as part of an experimental study that tried to dynamically induce snap-through in composite plates using MFC and a dynamic shaker. They found that the actuation of the MFC helped to reduce the amount of shaker force required to cause snap-through. They also found that the opposite could be true, though they did not investigate it further because increasing the loads required for snap-through was not the objective of the study.

Efforts to use piezoelectricity to invoke desired behavior in structures have not always been entirely successful. In a two-part theoretical/experimental study, Giannopoulos, et al. [72, 73] attempted to induce snap-through behavior in bimorph (i.e., piezoelectric material on both sides) beams with applications of low energy/high displacement actuators. Using Euler buckling theory they concluded that "the necessary actuation voltage to reach the critical point...for a simply supported beam exceeds the depolarization limit of the piezoelectric elements even for relatively small amount of vertical compression. Modified models with relaxed boundary conditions (spring) revealed that the voltage to perform snap through is much less and the importance of the boundary conditions cannot be underestimated."

In related work, Sridharan and Kim [74] investigated the potential for actuated piezoelectric patches to enhance the critical buckling load of imperfect columns. While they showed analytically that this strategy is possible, even modest increases in critical load required extremely high applied voltages ($\mathcal{O}\ 10^3$ volts—higher than the depolarization limit of most pizeoelectric materials). Overall, the researchers were quite negative on the prospect of using piezoelectric control as a means of preventing buckling, but noted that "...experimental corroboration is sorely needed to establish these conclusions on a firm footing and give them currency in the discipline of smart materials and structures" [74]. An inspection of the parameters used in Sridharan and Kim's analytical case study reveals that the column they considered was probably too stiff relative to the stabilizing effects offered by the actuators. The authors probably could have shown more promising results if they had considered a column with a lower flexural rigidity. Park and his colleague Kim showed how the large deflection of the composite panel can be suppressed using MFC actuators [75]. The numerical results indicated that MFC actuators can improve the performance of the panel; however, snap-through behavior can occur when excessive actuation of the MFC is applied to suppress the large deflection of the panel under aero-thermal loading. Recently, Aimmanee and Tichakorn [76] theoretically and experimentally considered piezoelectrically induced snap-through of post-buckled beams with various boundary conditions. For a steel substrate and a single MFC patch covering a portion of the substrate, they found the actuator lengths and placements that minimize the voltage required to induce snap-through.

Maurini, et al. [10] theoretically considered bending and axial piezoelectric actuation of a moderately post-buckled bimorph beam. Their model used an energy-based variational formulation and a two-mode Galerkin expansion. The authors call their model a "nonlinear extensible elastica model". While it is an elastica model in the sense that the problem is expressed in terms of arclength coordinates, its variational formulation makes it appear quite different from the discretized piezo-elastica formulation used here. Nevertheless, the Maurini, et al. [10] model yielded an intriguing result. By considering the contour of the Lagrangian of a post-buckled bimorph beam, they found that when adding a skew-symmetric component to the bending actuation, the beam can switch between the two buckled configurations without any instability. In other words, by traversing this new path, the system could avoid snap-through altogether. Maurini, et al. [10] recognized the important implications of this new path, and recommended that it be studied in the context of "complex structures such as deep arches, frames, and prestressed composite plates". They went on to add that "it remains to extend the present analysis to higher values of the buckling parameter, by including the effect of higher modes, and to investigate the effect of imperfections."

Subsequent research by Maurini and his collaborators considered shape control of bistable composite plates [11], and again identified stable paths linking remote equilibria. Some comprehensive studies [62, 66, 67] investigated stable equilibrium paths using bistable composites in depth. The identification of new stable equilibrium paths in piezoelectrically actuated structures is reminiscent of an investigation by the Lyman et al. [77]. It raises the intriguing possibility that multiple remote equilibria might each have a stable path connecting them using piezoelectrical actuation. Later, related research on the modeling, optimization, and control of bistable structures using piezoelectric actuation were studied in Refs. [78–81].

Structural morphing using piezoelectric smart materials [59, 63, 64, 66, 68, 79, 82–86] has also received significant attention for design of aerospace, micro-electro-mechanical and thermal-mechanical systems. Vos et al. [83, 84] proposed a new approach that post-buckled precompressed (PBP) piezoelectric actuators are integrated in a flexible wing structure to induce large deflections. PBP actuators can maintain low weight and power consumption, while extending control bandwidth. A semi-analytical composite structural model was built to predict the trailing-edge deflection due to piezoelectric actuation. When PBP actuators were activated, the trailing edge was forced to deform downward, leading to more lift on the wings. Later, Vos and his colleagues revealed different equilibrium states of a post-bucked piezoelectrically actuated beam. The beam was axially loaded and enhanced its imperfection (a proverse state) by applying active moments (positive voltage) from piezoelectric elements, but as the sign of the voltage was switched, the PBP element entered a converse-buckled state. Additionally, by increasing the axial force, the beam jumped followed by a higher-order snap-through to a remote proverse state [87]. Roe and Gandhi [85] designed a method for changing the shape of a wing using a trailing edge morphing beam comprised of smart and elastic materials. By actuating the smart material in the morphing beam, the shape of the the elastic material and the wing change accordingly. The new shape of the trailing edge illustrates a highly deformed buckled beam akin to a portion of the higher-order equilibrium shape of the post-buckled beam.

Zareie et al. [82] investigated the buckling control of morphing composite structures using multi-stable laminate by piezoelectric actuators. The results indicated that activating PZT increased the amount of deformation at the tail edge, which validated the structural morphing results from in Vos' research [84]. Betts et al. [52], Diaconu et al. [65], Bowen et al. [79], and Murray et al. [66], also conducted related research on modeling the shape morphing of plates and laminate using piezoelectric actuation.

In addition to creating morphing structures, smart materials can also be used to exploit the multi-stability of structures. In a recent review of buckling-related smart materials applications [69], several such multi-stable structures were described. Pham and Wang [88] proposed a quadristable mechanism (QM) which has a curved-beam bistable mechanism embedded within another curved-beam structure. Finite element models of the QM applying Euler's beam buckling theory are coupled and applied to double-clamped beams with fixed ends. Experiments showed some higher-order stable equilibrium shapes were possilbe. Dai et. al [89] developed a multi-stable lattice structure by assembling the simple bistable laminates. It contains tristable lattice cells and can offer three stable configurations. The critical snap-through loads are investigated for different stable states. Some of the stable lattice structures show configurations similar to the third- and fourth-order equilibrium shapes of a hinged-hinged post-buckled beam. A technique of energy harvesting at very low frequencies using the snap-through between multiple buckling modes of a beam with fixed-fixed ends was presented by Lajnef et. al [90]. In their research, multistable post-buckling equilibria are experimentally obtained by applying axial loads and correspond well with shapes from the finite element analysis. Pirrera and his collaborators [91] designed a morphing cylinder using a lattice of helices which have more stable states differing in their radii and length. They used composite materials to exploit the interplay between pre-stress, material properties, and structural geometry, and then demonstrated the multi-stability of the structure.

Smart materials applications aside, there is a subset of the literature focusing on the purely stucutural mechanics aspects of multi-stable systems. As early as 1992, Hwang and Perkins [92, 93] established a model and determined equilibria of a curved, axially moving beam. The model considers large static beam deformations, and motion from equilibrium is described using a nonlinear rod theory. Exact equilibrium solutions are obtained at both sub-critical and super-critical translation speeds, and bifurcations occur near the critical speed, leading to multiple beam equilibrium states. Local stability is predicted from the eigen-value problem governing the free response. Wickert [94] also investigated a similar beam model while using Euler column buckling model. Later, Raboud et. al [95] explored stability evaluation of flexible cantilever beams and found multiple equilibrium solutions (three typical shapes). Nayfeh and Emam [96] solved the nonlinear post-buckling problem for different boundary conditions and obtained a closed-form solution for the buckled configurations as a function of the applied axial load. They showed the static bifurcation for buckled configurations of a fixed–fixed beam and gave the relation to the applied axial load. When the axial load exceeds the first critical buckling load, the straight position loses stability and the beam buckles. Emam and Nayfeh [97] studied the post-buckled and free vibration behaviors of composite beams. They exactly solved the linear vibration problem around the first buckled configuration. Both the post-buckling analysis and the free vibration analysis in the post-buckling domain strongly depend on the layout of the laminate. Some works show higher-order equilibria of a post-buckled structure can be obtained theoretically, but little research has been conducted investigating higher-order stable equilibria.

1.4.3 Thermal Control of Structural Instability

Smart materials that have one property that can be significantly changed with temperature are the basis of applications involving thermo-mechanical behaviors [98–102]. Snap-through loads in such materials can sometimes be changed by changing temperature. Finite element (FE) analysis is commonly used to model snap-through instability of post-buckled structures involving thermal influences. Experiments are sometimes conducted to validates these FE models.

Lee and Kim [103] investigated the thermo-mechanical behaviors of functionally graded material (FGM) panels in hypersonic airflows. For the structural model, the thermo-mechanical characteristics were investigated according to the thermal and aerodynamic loads. They revealed that if the thermal or aerodynamic loads exceed a critical value, the panel snaps to the remote equilibrium position. A similar work done by Zhang et al. [104] studied the effects of thermo-mechanical loading on the bistable behavior and deformation process of anti-symmetric cylindrical shells. They indicated that the shape of the bistable composite shell can be adjusted by imposing different combinations of uniform temperature fields and through-thickness thermal gradients. This is helpful for applications of bistable structures in the aerospace industry, for instance. Przekop and Rizzi [105] investigated numerical simulation methods for the nonlinear response of structures combined with high-intensity random pressure fluctuations and thermal loading. The dynamic thermal bucking problem is studied by applying a uniformly distributed, positive temperature increment. A reduced-order FE method for predicting thermo-acoustic random response was presented. The effect of elevated temperature on the modal stiffness coefficients was examined and it was found that only the linear stiffness coefficients corresponding to low-frequency transverse displacement modes were affected by changing temperature and they vary linearly with temperature. A modal basis consisting of four types of modes (symmetric transverse, anti-symmetric transverse, symmetric in-plane, and anti-symmetric in-plane), shown in Fig. 1.6, accurately predicts the dynamic thermal buckling and thermal-acoustic response.

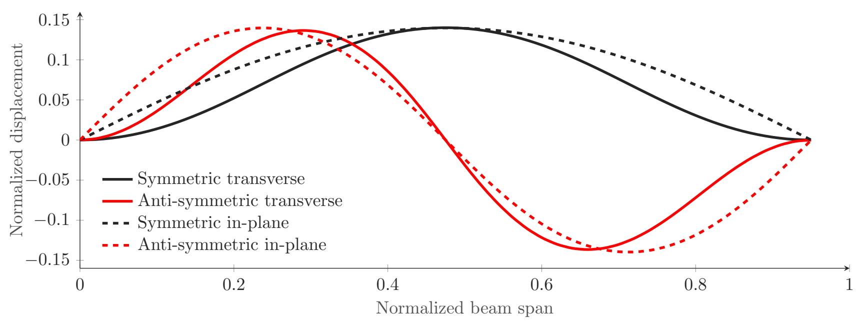

Figure 1.6. Lowest four types of modes of a post-buckled clamped beam from Ref. [105].

Snap-through due to a uniform lateral pressure in a thermally post-buckled sandwich beam is analyzed in Mirzaei's work [106]. Material properties of the face sheets and core are assumed to be temperature dependent. The results show that increasing the temperature results in higher thermal post-buckling deflection. In addition, as the induced post-buckling deflection increases, the upper and lower limit loads both increase and the intensity of the snap-through (snap-through amplitude between two remote equilibria) increases. Mattioni et al. [107] modeled the nonlinear flexural response of laminates that have piecewise variation of their planform lay-up and focused on the effects of thermal stresses on the resulting equilibrium shapes. They found that unsymmetric laminates may possess more than a single equilibrium configuration, and the solution thus bifurcates at a critical temperature. Stanciulescu et al. [108] identified a non-trivial (non-flat) configuration of the curved clamped-clamped beam at a critical temperature below which the beam will no longer experience snap-through under any magnitude of applied quasi-static load. The critical temperature is shown to successfully eliminate snap-through in dynamic simulations at quasi-static loading rates. In their study, they referred to the coupling between elastic deformation and thermal effects via the thermal strain terms in the equations of mechanical equilibrium and the structural elastic heating term in the heat equation. Structural morphing and snap-through behavior of hybrid laminate shells driven solely by temperature change were studied by Eckstein et al. [109]. Thermally-driven structures were characterized by their ability to exhibit a shape change in response to thermal loading. They demonstrate that the tailorability of composite materials combined with the geometrically nonlinear large-displacement response of thin shells can yield thermal bimorph devices with highly nonlinear displacement response to temperature change.

Researchers are also interested in snap-through control combining thermal effects and piezoelectric actuation. Park and Kim [75] studied the characteristics of thermal post-buckling of the composite panel embedded with MFC actuators. The Newton–Raphson method is used to calculate the aero-thermal large deflection of the panel, and the cylindrical arclength method [110, 111] is adopted to describe the snap-through behavior of the panel. They found that in-plane actuation using MFC can increase the critical temperature and decrease the large deflections caused by thermal loading. They also found that aero-thermal large deflections can be suppressed by out-of-plane actuation of MFC. Dano and Jullière [112, 113] investigated the use of MFC actuators to compensate and actively control thermally induced deformations in composite structures. A uniform temperature change is applied to induce a large change in the structural shape, and the MFC are actuated to compensate for the thermally induced distortion. The results show that MFC actuators can eliminate thermal deformations when a sufficient voltage is applied. Moreover, a control algorithm is implemented to actively control the closed loop response of the structure. The model includes structural, thermal and piezoelectric fields. Studies in Refs. [75, 112, 113] make a comprehensive "thermo-piezoelectric-mechanical" coupling model to investigate the stability of post-buckled structures.

Lastly, it is noted that at room temperatures, snap-through instability of post-buckled structures is only mildly influenced by thermal changes, and in general, deformations caused by temperature changes are relatively small compared to the changes induced by piezoelectric actuators.

1.5 Current Work

The idea of using lightweight and flexible piezoelectric materials to control structural instabilities of post-buckled beams is proposed. A new electromechanically coupled elastica model is developed with extensions accounting for the influence of elongating piezoelectric films bonded to the beam. The model's discretized formulation is implemented for the physical systems of interest, is not limited to moderate displacements, and can be adapted to account for different boundary conditions. The present theoretical model, which is cast in non-dimensional terms, enables a more general view of what is possible with piezoelectric actuation and allows researchers to discern whether a candidate structure will be sufficiently amenable to piezoelectric actuation. The electromechanical coupling parameter can therefore be used as a metric for designing realistic systems capable of circumventing snap-through.

The configuration of primary interest involves piezoelectric materials bonded to clamped-clamped post-buckled beams. The model of this system is presented in Chapter 2 and expresses the piezoelectric coupling effect in terms of a new non-dimensional parameter, σ, that can be easily calculated for candidate substrate/actuator configurations. In Chapter 3, static equilibrium positions and their stability are computed across a large configuration space using numerical integration and a shooting method. Results indicate that the effect of piezoelectric actuation on critical snap-through load depends on the degree to which the beam is buckled, the location of the external load, the placement of the piezoelectric material, and the applied actuation voltage. Experiments are performed to validate the numerical results and provide a physical demonstration of changing snap-through loads with piezoelectric actuation. Experimental results demonstrate that critical snap-through loads can be altered by factors ranging from 0.4 to 2.0, and numerical results indicate that even larger changes to snap-through loads are physically realizable.

Next, in Chapter 4, the avoidance of snap-through instability is demonstrated by invoking stable transitions between remote equilibria. Specifically, this is achieved with mildly post-buckled clamped-clamped beams with two axial piezoelectric actuators bonded to their surface. Through the intelligent control of the two actuators, stable transitions between remote equilibria can be traversed, thus circumventing snap-through. Given the limitations of existing piezoelectric actuators, stable transitions are only possible in a subset of substrate/actuator configurations. Experiments are conducted to verify the numerical results and physically demonstrate stable transitions between remote equilibria.

In Chapter 5, natural frequencies and modes of the beams are identified numerically and experimentally during the stable transitions. The changes of equilibrium shapes, first four frequencies, and their mode shapes are studied using axial piezoelectric actuators. It is found that the direction of the beam's movement in the first two modes always changes during a stable transition. The first and third natural frequencies usually decrease while the second and fourth ones increase with increases the voltage. The magnitude of normalized dynamic deflection for different actuation regions at select σ values are also studied.

Finally, in Chapter 6, the stability of higher-order equilibrium shapes of clamped-clamped post-buckled beams under piezoelectric actuation are determined. It is assumed three or four piezoelectric patches are distributed along the beam. In certain situations, stable third- and fourth-order equilibrium shapes can be achieved with three and four piezoelectric patches, respectively. Effects of actuation region are studied to find the parameter space associated with these stable equilibria. Experiments are performed to verify the numerical results and show physical higher-order equilibrium shapes.

The primary contributions of this work are as follows:

1. Elastica theory is extended to include a new non-dimensional parameter that describes the influence of piezoelectric actuation on a structure;
2. Results indicate the physical configurations and actuation strategies altering stability most profoundly;
3. The threshold for achieving stable transitions is given in terms of the non-dimensional electromechanical coupling parameter;
4. Stable transition paths are found to exhibit a strong dependence on the magnitude and location of the external load in addition to the actuation voltage and actuated patch span;
5. Natural frequencies and mode shapes are calculated for different stable transition paths;
6. Stable higher-order equilibrium shapes of post-buckled beam can be achieved under piezoelectric actuation;
7. Experiments validate the results of the numerical model and demonstrate how piezoelectric actuation can change snap-through loads, invoke stable transitions between remote equilibria, and stabilize higher-order equilibrium shapes. The natural frequencies and modes along a stable transisition path are also experimentally validated.

Chapter 2

Electromechanically Coupled Elastica Model

The electromechanical system of a post-buckled beam with piezoelctric film bonded to its surface is based on elastica theory with allowances for piezoelectric actuation. Elastica theory establishes the structural geometry in terms of an arc-length coordinate and presumes that the structure is slender, isotropic, and hyperelastic [13, 17, 114]. A non-dimensional electromechanical coupling term models the influences of the piezoelectric material.

An inextensible beam of length l^*, thickness h_s^*, and width b^* is assumed to be post-buckled, clamped on both ends and shortened by an amount of e^*. Piezoelectric material of thickness h_p^* covers one side of the beam, as shown in Fig. 2.1. The origin of the coordinate system is at the left support. Different voltages, V_1, V_2, and up to V_n are applied to each patch of piezoelectric material.

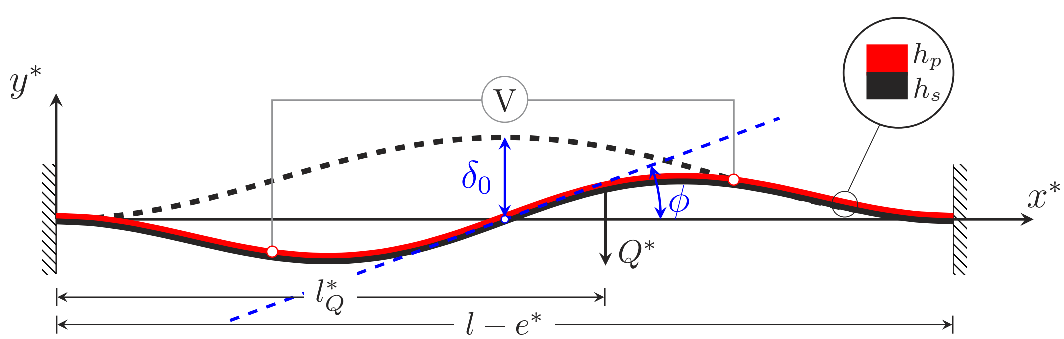

Figure 2.1. Schematic of a clamped-clamped post-buckled beam with flexible piezoelectric material bonded across the span.

Consider an inextensible post-buckled beam of length l, width b, and thickness h_s, as shown in Fig. 2.1. The superscript * is used to distinguish dimensional quantities from the corresponding non-dimensional quantities to be defined later. (Dimensional quantities that do not have a non-dimensional counterpart are denoted without a superscript.) One side of the beam is covered with a piezoelectric material of thickness h_p. The beam has clamped supports on both ends and is shortened by an amount e^*. The coordinate system is fixed with the origin at the left support. The beam is subject to a lateral body-fixed point load, Q^*, which is applied at a distance from the origin given by l_Q^*. A voltage, V, is applied to the piezoelectric patch. The patch length is variable. Different piezoelectric patches are bonded to the beam for different actuation schemes, and several different voltages can be applied to each patch. The structural behavior is captured with two parameters: mid-point deflection, δ, and mid-point rotation angle, ϕ.

Since piezoelectric material is placed on only one side of the substrate (unimorph), the composite structure is asymmetric and its neutral axis is not located at the geometric midplane of the composite. The placement of the neutral axis is specified by y_0 which is defined as the distance from the geometric midplane of the substrate, as shown in Fig. 2.2. This places the interface between substrate and the piezoelectric material at a distance from the neutral axis of $h_s/2 - y_0$. As Brissaud et al. [115] showed, y_0 for the present configuration is given by

$$y_0 = \frac{Y_p h_p (h_s + h_p)}{2(Y_s h_s + Y_p h_p)}. \tag{2.1}$$

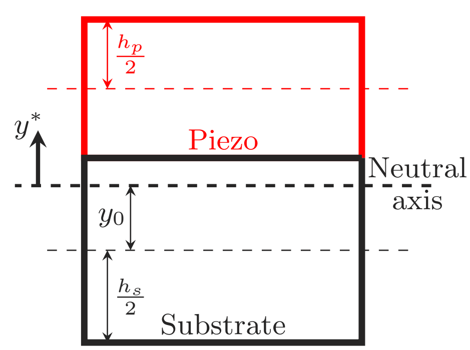

Figure 2.2. Cross-section of composite beam with neutral axis shown.

2.1 Bending Moment in the Composite Beam

The bending moment of the composite beam relative to the neutral axis is given by [116]

$$m^* = b\left(\int_{-\frac{h_s}{2}-y_0}^{\frac{h_s}{2}-y_0} T_s y^* dy^* + \int_{\frac{h_s}{2}-y_0}^{h_p+\frac{h_s}{2}-y_0} T_p y^* dy^*\right), \tag{2.2}$$

where T_s and T_p are the stress in the substrate and piezoelectric material. The stress in the substrate is given by Hooke's law, $T_s = Y_s y^* \frac{d\theta}{ds^*}$, where Y_s is the Young's modulus of the material and $d\theta/ds^*$ is the curvature.

The following constitutive equations for an elongating piezoelectric layer are assumed [117]

$$\begin{bmatrix} T_p \\ D_p \end{bmatrix} = \begin{bmatrix} \bar{c}_{33}^E & -\bar{e}_{33} \\ \bar{e}_{33} & \bar{\varepsilon}_{33}^S \end{bmatrix} \begin{bmatrix} S_p \\ E_p \end{bmatrix}, \tag{2.3}$$

where T_p and D_p represent the stress and electric displacement, respectively, and $\bar{c}_{33}^E$ is the elastic stiffness (i.e., Young's modulus) in the 3-direction (i.e., longitudinal direction) of the beam under constant electric field. Going forward, $\bar{c}_{33}^E$ is denoted Y_p. The parameter $\bar{e}_{33}$ is the piezoelectric constant related to elongation and is given by $\bar{e}_{33} = Y_p d_{33}$, where d_{33} is the piezoelectric constant more commonly given in the specifications of piezoelectric materials. Finally, $\bar{\varepsilon}_{33}^S$ is the permittivity at constant strain, S_p is the strain, and E_p is electric field component given by $E_p = -V/l_p$, where V is the applied voltage and l_p is the spacing between neighboring positive and negative poles of the piezoelectric material. The over-bar denotes an effective constant under plane-stress conditions. Assuming the mechanical strain in the piezoelectric is due to bending only, Eq. (2.3) gives the following relationship for stress in the piezoelectric layer

$$T_p = Y_p(S_p - d_{33}E_p) = Y_p\left(y^*\frac{d\theta}{ds^*} + d_{33}\frac{V}{l_p}\right). \tag{2.4}$$

Using the expressions for T_s and T_p in Eq. (2.2), the moment in the composite beam becomes

$$m^* = b\left(\int_{-\frac{h_s}{2}-y_0}^{\frac{h_s}{2}-y_0} Y_s y^{*2}\frac{d\theta}{ds^*}dy^* + \int_{\frac{h_s}{2}-y_0}^{h_p+\frac{h_s}{2}-y_0} Y_p\left(y^{*2}\frac{d\theta}{ds^*} + y^*\frac{d_{33}V}{l_p}\right)dy^*\right), \tag{2.5}$$

$$m^* = bY_s \frac{d\theta}{ds^*} \frac{y^{*3}}{3}\bigg|_{-\frac{h_s}{2}-y_0}^{\frac{h_s}{2}-y_0} + bY_p \frac{d\theta}{ds^*} \frac{y^{*3}}{3}\bigg|_{\frac{h_s}{2}-y_0}^{h_p+\frac{h_s}{2}-y_0} + bY_p \frac{d_{33}V}{l_p} \frac{y^{*2}}{2}\bigg|_{\frac{h_s}{2}-y_0}^{h_p+\frac{h_s}{2}-y_0}. \tag{2.6}$$

Evaluating Eq. (2.6) results in an expression for bending moment

$$m^* = YI \frac{d\theta}{ds^*} + \chi V, \tag{2.7}$$

where YI is the flexural rigidity of the composite beam, including the component of substrate and piezoelectric film, i.e.,

$$YI = b\left(Y_s\left(\frac{h_s^3}{12} + h_s y_0^2\right) + Y_p\left(\frac{h_p^3}{12} + h_p\left(\frac{h_s+h_p}{2} - y_0\right)^2\right)\right), \tag{2.8}$$

and χ is the electromechanical coupling coefficient given by

$$\chi = \frac{bd_{33}Y_p h_p}{l_p}\left(\frac{h_s}{2} + \frac{h_p}{2} - y_0\right). \tag{2.9}$$

2.2 Equilibrium Equations and Stability Analysis

The following non-dimensional parameters are defined:

$$\begin{aligned} &(s, x, y, e, l_Q) = \frac{1}{l}\left(s^*, x^*, y^*, e^*, l_Q^*\right), \quad \sigma = \frac{\chi V l}{YI}, \\ &(p_0, q_0, Q) = \frac{l^2}{\pi^2 YI}\left(p_0^*, q_0^*, Q^*\right), \quad m = \frac{m^* l}{YI}, \quad \omega = \sqrt{\frac{\mu l^4}{\pi^2 YI}}\omega^*, \end{aligned} \tag{2.10}$$

where p_0^* and q_0^* are the axial and lateral reaction forces at the origin ($s^* = 0$), ω^* is the natural frequency, and $\mu = \rho_s b h_s + \rho_p b h_p$ is the mass per unit length of the composite beam. The non-dimensional parameter σ captures the effect of piezoelectric actuation.

Accounting for the presence of the body-fixed lateral load at $s^* = l_Q^*$, the equation for the moment at any point on the beam is related to the axial and lateral load at the supports and the applied point load by

$$m^* = -q_0^* x^* + p_0^* y^* - Q^*(x^* - x^*_{(s^*=l_Q^*)})H(s^* - l_Q^*), \tag{2.11}$$

where H is the Heaviside step function. Differentiating Eq. (2.11) with respect to s^* and using non-dimensional parameters, the spatial derivative of the moment is obtained

$$\frac{dm}{ds} = \pi^2 \left(-q_0 \frac{dx}{ds} + p_0 \frac{dy}{ds} - Q \frac{dx}{ds} H(s - l_Q) \right), \tag{2.12}$$

where the x and y position of the beam can be inferred from geometry as

$$\frac{dx}{ds} = \cos\theta, \quad \frac{dy}{ds} = \sin\theta. \tag{2.13}$$

Substituting Eqs. (2.10) into Eq. (2.7), and Eqs. (2.13) into Eq. (2.12), the dimensionless equilibrium equations (along with Eqs. (2.13)) are

$$\frac{d\theta}{ds} = m - \sigma, \tag{2.14}$$

$$\frac{dm}{ds} = \pi^2 \left(-q_0 \cos\theta + p_0 \sin\theta - Q \cos\theta H(s - l_Q) \right). \tag{2.15}$$

Note that the electromechanical coupling term, σ, appears in the equilibrium equations in the same manner as an initial imperfection. Critical snap-through loads, Q_{cr}, are known to increase linearly with initial imperfection for shallow arches [118], and are therefore expected to increase linearly with increasing σ, at least for mildly post-buckled structures.

The boundary conditions of a clamped-clamped post-buckled beam at the origin are

$$x|_{s=0} = 0, \quad y|_{s=0} = 0, \quad \theta|_{s=0} = 0. \tag{2.16}$$

At the right end of the beam, the boundary conditions are

$$x|_{s=1} = 1 - e, \quad y|_{s=1} = 0, \quad \theta|_{s=1} = 0. \tag{2.17}$$

Eqs. (2.13)–(2.15) are used to find the equilibrium positions of post-buckled beams with piezoelectric film bonded to one surface. Stability is determined using a standard approach [119, 120] that assumes small amplitude harmonic oscillations about a given equilibrium position, i.e.,

$$\begin{aligned}
&x(s,t) = x_e + x_d \sin\omega t, \quad y(s,t) = y_e + y_d \sin\omega t, \\
&\theta(s,t) = \theta_e + \theta_d \sin\omega t, \quad m(s,t) = m_e + m_d \sin\omega t, \\
&p(s,t) = p_0 + p_d \sin\omega t, \quad q(s,t) = q_0 + q_d \sin\omega t,
\end{aligned} \tag{2.18}$$

where subscripts e and d denote static and dynamic quantities and ω is the non-dimensional natural frequency.

The non-dimensional partial differential equations for the axial and lateral reaction forces are [121]

$$\frac{\partial p(s,t)}{\partial s} = \frac{\partial^2 x(s,t)}{\partial t^2}, \quad \frac{\partial q(s,t)}{\partial s} = \frac{\partial^2 y(s,t)}{\partial t^2}. \tag{2.19}$$

Substituting Eqs. (2.18) into Eqs. (2.13)–(2.15) and (2.19) gives

$$\begin{aligned}
&\frac{\partial x_e}{\partial s} + \frac{\partial x_d}{\partial s}\sin\omega t = \cos(\theta_e + \theta_d \sin\omega t), \\
&\frac{\partial y_e}{\partial s} + \frac{\partial y_d}{\partial s}\sin\omega t = \sin(\theta_e + \theta_d \sin\omega t), \\
&\frac{\partial \theta_e}{\partial s} + \frac{\partial \theta_d}{\partial s}\sin\omega t = m_e - \sigma + m_d \sin\omega t, \\
&\frac{\partial m_e}{\partial s} + \frac{\partial m_d}{\partial s}\sin\omega t = \pi^2 \left[-(q_0 + q_d \sin\omega t)\cos(\theta_e + \theta_d \sin\omega t)\right. \\
&\qquad \left. +(p_0 + p_d \sin\omega t)\sin(\theta_e + \theta_d \sin\omega t) - Q\cos(\theta_e + \theta_d \sin\omega t)H(s - l_Q)\right], \\
&\frac{\partial p_d}{\partial s}\sin\omega t = \frac{\partial^2}{\partial t^2}(x_d \sin\omega t), \\
&\frac{\partial q_d}{\partial s}\sin\omega t = \frac{\partial^2}{\partial t^2}(y_d \sin\omega t).
\end{aligned} \tag{2.20}$$

Assuming small oscillations about equilibrium, second-order quantities can be neglected and Eqs. (2.20) become

$$\begin{aligned}
&\frac{\partial x_d}{\partial s} = -\theta_d \sin\theta_e, \quad \frac{\partial y_d}{\partial s} = \theta_d \cos\theta_e, \quad \frac{\partial \theta_d}{\partial s} = m_d, \\
&\frac{\partial m_d}{\partial s} = \pi^2 \left((p_0\theta_d - q_d)\cos\theta_e + (p_d + q_0\theta_d)\sin\theta_e + Q\theta_d \sin\theta_e H(s - l_Q)\right), \\
&\frac{\partial p_d}{\partial s} = -\omega^2 x_d, \quad \frac{\partial q_d}{\partial s} = -\omega^2 y_d.
\end{aligned} \tag{2.21}$$

Upon solving Eqs. (2.21), stability is determined from the sign of ω^2—positive values indicate that the equilibrium position is stable while negative values denote instability. Consequently, the critical snap-through loads correspond to cases where $\omega^2 = 0$.

2.3 Numerical Solution Method

To determine equilibrium positions and their stability, the beam is discretized into a specified number of segments (100 segments are used here), and Eqs. (2.13)–(2.15) and (2.21) are solved using a Runge-Kutta numerical integration scheme in conjunction with a shooting method. Newton's Method is used to iteratively adjust the shooting parameters until the right-end boundary values are met within a specified tolerance (10^{-9} is used here). More information on the use of shooting methods to solve the elastica can be found in Santillan [16]. The solution procedure consists of three parts that will be detailed presently.

2.3.1 Equilibrium Positions for $Q = 0$ and $\sigma = 0$

In the first part, the first four equilibria corresponding to $Q = 0$ and $\sigma = 0$ (see Fig. 2.3) are found by specifying the end shortening parameter e, and performing the shooting method with a vector, $\boldsymbol{\alpha} = \{m_0, p_0, q_0\}^T$, as the shooting parameters. The boundary values at $s = 1$, Eqs. (2.17), act as the vector-valued objective functions.

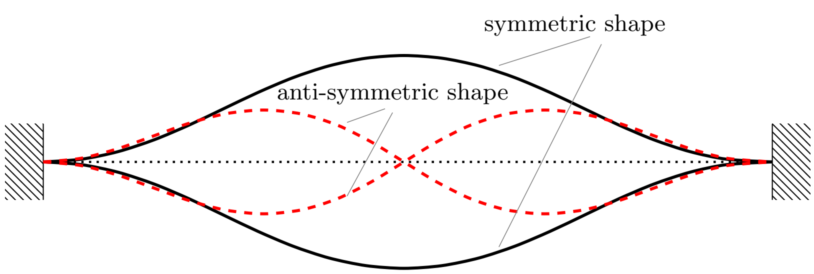

Figure 2.3. First four equilibrium shapes of an unloaded clamped-clamped post-buckled beam. Solid lines indicate stable symmetric shapes, and dashed lines show the unstable anti-symmetric shapes.

Unknown variables in Eqs. (2.13)–(2.15) can be rewritten into a vector $\boldsymbol{u} = \{x, y, \theta, m, s\}^T$. The equilibrium equations are now

$$\boldsymbol{g}(\boldsymbol{u}) = \frac{d\boldsymbol{u}}{ds}, \quad \boldsymbol{u} = \{x, y, \theta, m, s\}^T. \tag{2.22}$$

A new vector function, $\boldsymbol{v}$, is defined as

$$\boldsymbol{v}(s) = \frac{\partial \boldsymbol{u}}{\partial \alpha_i}, \tag{2.23}$$

where α_i is an element of the vector $\boldsymbol{\alpha}$. The derivative of $\boldsymbol{v}$ with respect to s is

$$\frac{d\boldsymbol{v}}{ds} = \frac{d}{ds}\left(\frac{\partial \boldsymbol{u}}{\partial \alpha}\right) = \frac{\partial}{\partial \alpha}\left(\frac{d\boldsymbol{u}}{ds}\right) = \frac{\partial}{\partial \alpha}\boldsymbol{g}(\boldsymbol{u}) = \frac{d\boldsymbol{g}}{d\boldsymbol{u}}\frac{\partial \boldsymbol{u}}{\partial \alpha} = \frac{d\boldsymbol{g}}{d\boldsymbol{u}}\boldsymbol{v}. \tag{2.24}$$

The new differential equations, including equilibrium equations and objective functions of shooting method, are

$$\frac{d\boldsymbol{u}}{ds} = \boldsymbol{g}(\boldsymbol{u}), \quad \frac{d\boldsymbol{v}}{ds} = \frac{d\boldsymbol{g}(\boldsymbol{u})}{d\boldsymbol{u}}\boldsymbol{v}. \tag{2.25}$$

Combining $\boldsymbol{u}$ and $\boldsymbol{v}$ into the vector $\bar{\boldsymbol{u}}$, Eqs. (2.25) becomes

$$\frac{d\bar{\boldsymbol{u}}}{ds} = \begin{Bmatrix} \boldsymbol{g} \\ \frac{d\boldsymbol{g}}{d\boldsymbol{u}}\frac{\partial \boldsymbol{u}}{\partial m_0} \\ \frac{d\boldsymbol{g}}{d\boldsymbol{u}}\frac{\partial \boldsymbol{u}}{\partial p_0} \\ \frac{d\boldsymbol{g}}{d\boldsymbol{u}}\frac{\partial \boldsymbol{u}}{\partial q_0} \end{Bmatrix}, \quad \bar{\boldsymbol{u}} = \begin{Bmatrix} \boldsymbol{u} \\ \frac{\partial \boldsymbol{u}}{\partial m_0} \\ \frac{\partial \boldsymbol{u}}{\partial p_0} \\ \frac{\partial \boldsymbol{u}}{\partial q_0} \end{Bmatrix}, \tag{2.26}$$

where the shooting parameters are m_0, p_0, and q_0. For $Q = 0$ and $\sigma = 0$, each term of $d\bar{\boldsymbol{u}}/ds$ in Eqs. (2.26) is given by

$$\boldsymbol{g} = \begin{Bmatrix} \cos\theta \\ \sin\theta \\ m \\ \pi^2\left(-q_0\cos\theta + p_0\sin\theta\right) \\ 1 \end{Bmatrix}, \tag{2.27}$$

$$\frac{d\boldsymbol{g}}{d\boldsymbol{u}}\frac{\partial \boldsymbol{u}}{\partial m_0} = \begin{Bmatrix} -\sin\theta\frac{\partial\theta}{\partial m_0} \\ \cos\theta\frac{\partial\theta}{\partial m_0} \\ \frac{\partial m}{\partial m_0} \\ \pi^2\left(q_0\sin\theta + p_0\cos\theta\right)\frac{\partial\theta}{\partial m_0} \\ 0 \end{Bmatrix}, \tag{2.28}$$

$$\frac{d\boldsymbol{g}}{d\boldsymbol{u}}\frac{\partial \boldsymbol{u}}{\partial p_0} = \left\{\begin{array}{c} -\sin\theta\frac{\partial\theta}{\partial p_0} \\ \cos\theta\frac{\partial\theta}{\partial p_0} \\ \frac{\partial m}{\partial p_0} \\ \pi^2\left(q_0\sin\theta + p_0\cos\theta\right)\frac{\partial\theta}{\partial p_0} + \pi^2\sin\theta \\ 0 \end{array}\right\}, \tag{2.29}$$

$$\frac{d\boldsymbol{g}}{d\boldsymbol{u}}\frac{\partial \boldsymbol{u}}{\partial q_0} = \left\{\begin{array}{c} -\sin\theta\frac{\partial\theta}{\partial q_0} \\ \cos\theta\frac{\partial\theta}{\partial q_0} \\ \frac{\partial m}{\partial q_0} \\ \pi^2\left(q_0\sin\theta + p_0\cos\theta\right)\frac{\partial\theta}{\partial q_0} - \pi^2\cos\theta \\ 0 \end{array}\right\}. \tag{2.30}$$

The vector of objective functions, $\boldsymbol{f}(\boldsymbol{\alpha})$, is now defined as the difference between the resulting values from an iterated $\boldsymbol{\alpha}$ and the right-end boundary value, i.e.

$$\boldsymbol{f}(\boldsymbol{\alpha}) = \left\{\begin{array}{c} x(s,\boldsymbol{\alpha}) - (1-e) \\ y(s,\boldsymbol{\alpha}) \\ \theta(s,\boldsymbol{\alpha}) \end{array}\right\}_{s=1} = \left\{\begin{array}{c} x(1,\boldsymbol{\alpha}) - (1-e) \\ y(1,\boldsymbol{\alpha}) \\ \theta(1,\boldsymbol{\alpha}) \end{array}\right\}. \tag{2.31}$$

When the objective function $\boldsymbol{f}(\boldsymbol{\alpha}) = 0$ at $\boldsymbol{\alpha}_k$, the shooting parameters, $\boldsymbol{\alpha}_k$, satisfy the exact right-end boundary conditions. Here, a tolerance of $||\boldsymbol{f}(\boldsymbol{\alpha}_k)|| \leqslant 10^{-9}$ is used. The vector-form of the Newton iteration equation is given by

$$\boldsymbol{\alpha}_{k+1} = \boldsymbol{\alpha}_k - \boldsymbol{J}_{\boldsymbol{\alpha}_k}^{-1}\boldsymbol{f}(\boldsymbol{\alpha}_k), \quad \boldsymbol{J}_{\boldsymbol{\alpha}_k} = \left[\frac{\partial f_j}{\partial \alpha_i}\right]_{\boldsymbol{\alpha}_k}, \tag{2.32}$$

where the components of the Jacobian matrix are found from $\frac{\partial \boldsymbol{u}}{\partial \alpha_i}$ in Eqs. (2.26), i.e.,

$$\boldsymbol{J}_{\boldsymbol{\alpha}_k} = \begin{bmatrix} \frac{\partial x}{\partial m_0} & \frac{\partial x}{\partial p_0} & \frac{\partial x}{\partial q_0} \\ \frac{\partial y}{\partial m_0} & \frac{\partial y}{\partial p_0} & \frac{\partial y}{\partial q_0} \\ \frac{\partial \theta}{\partial m_0} & \frac{\partial \theta}{\partial p_0} & \frac{\partial \theta}{\partial q_0} \end{bmatrix}_{s=1}. \tag{2.33}$$

Equilibria of the post-buckled beam for $Q = 0$ and $\sigma = 0$ can be determined by solving differential equations Eqs. (2.26) using Runge-Kutta integration method with initial guess of $\bar{\boldsymbol{u}}_0 = \{0,0,0,m_0,0,0,0,0,1,0,0,0,0,0,0,0,0,0,0,0\}^T$, and the Newton iteration equation, Eq. (2.32).

2.3.2 Equilibrium Positions for $Q \neq 0$ and $\sigma \neq 0$

In the second part, equilibrium shapes are found across a range of external loads, Q, and electromechanical coupling parameters, σ. The values of Q and σ are incremented gradually from zero in steps of 0.02. At each value, initial guesses are also supplied for m_0, p_0, and q_0. For each subsequent load step, the final values of m_0, p_0, and q_0 from the previous step are used as initial guesses.

For $Q \neq 0$ and $\sigma \neq 0$, each term of $d\bar{\boldsymbol{u}}/ds$ in Eqs. (2.26) is modified to

$$\boldsymbol{g} = \begin{Bmatrix} \cos\theta \\ \sin\theta \\ m - \sigma \\ \pi^2 \left(-q_0 \cos\theta + p_0 \sin\theta - Q\cos\theta H(s - l_Q)\right) \\ 1 \end{Bmatrix}, \tag{2.34}$$

$$\frac{d\boldsymbol{g}}{d\boldsymbol{u}}\frac{\partial \boldsymbol{u}}{\partial m_0} = \begin{Bmatrix} -\sin\theta \frac{\partial\theta}{\partial m_0} \\ \cos\theta \frac{\partial\theta}{\partial m_0} \\ \frac{\partial m}{\partial m_0} \\ \pi^2 \left(q_0 \sin\theta + p_0 \cos\theta + Q\sin\theta H(s - l_Q)\right) \frac{\partial\theta}{\partial m_0} \\ 0 \end{Bmatrix}, \tag{2.35}$$

$$\frac{d\boldsymbol{g}}{d\boldsymbol{u}}\frac{\partial \boldsymbol{u}}{\partial p_0} = \begin{Bmatrix} -\sin\theta \frac{\partial\theta}{\partial p_0} \\ \cos\theta \frac{\partial\theta}{\partial p_0} \\ \frac{\partial m}{\partial p_0} \\ \pi^2 \left(q_0 \sin\theta + p_0 \cos\theta + Q\sin\theta H(s - l_Q)\right) \frac{\partial\theta}{\partial p_0} + \pi^2 \sin\theta \\ 0 \end{Bmatrix}, \tag{2.36}$$

$$\frac{d\boldsymbol{g}}{d\boldsymbol{u}}\frac{\partial \boldsymbol{u}}{\partial q_0} = \begin{Bmatrix} -\sin\theta \frac{\partial\theta}{\partial q_0} \\ \cos\theta \frac{\partial\theta}{\partial q_0} \\ \frac{\partial m}{\partial q_0} \\ \pi^2 \left(q_0 \sin\theta + p_0 \cos\theta + Q\sin\theta H(s - l_Q)\right) \frac{\partial\theta}{\partial q_0} - \pi^2 \cos\theta \\ 0 \end{Bmatrix}. \tag{2.37}$$

Equilibrium shapes for $Q \neq 0$ and $\sigma \neq 0$ are determined by solving Eqs. (2.26) with Eqs. (2.34)-(2.37), and the Newton iteration equation, Eq. (2.32).

2.3.3 Stability Determination

In the third part, the stability of the identified equilibrium is determined by using the dynamic axial and lateral loads, p_{d0} and q_{d0}, and natural frequency squared, ω^2, as shooting parameters, i.e., $\boldsymbol{\alpha} = \{p_{d0}, q_{d0}, \omega^2\}^T$.

The shooting parameters are iterated until x_d, y_d, and θ_d are equal to zero at $s = 1$ within a tolerance of 10^{-9}.

Variables in Eqs. (2.13)–(2.15) and (2.21) are rewritten into a vector $\boldsymbol{u}$, and the equilibrium equations for both static and dynamic quantities are

$$\boldsymbol{g}(\boldsymbol{u}) = \frac{d\boldsymbol{u}}{ds}, \quad \boldsymbol{u} = \{x_e, y_e, \theta_e, m_e, x_d, y_d, \theta_d, m_d, p_d, q_d, s\}^T. \tag{2.38}$$

Since the shooting parameters $\boldsymbol{\alpha}$ all correspond to the dynamic system, $\frac{\partial x_e}{\partial \alpha_i}$, $\frac{\partial x_e}{\partial \alpha_i}$, $\frac{\partial \theta_e}{\partial \alpha_i}$, $\frac{\partial m_e}{\partial \alpha_i}$ and $\frac{\partial s}{\partial \alpha_i}$ are all zero. The new vector function, $\boldsymbol{v}$, is then defined as

$$\boldsymbol{v}(s) = \frac{\partial \hat{\boldsymbol{u}}}{\partial \alpha_i}, \quad \hat{\boldsymbol{u}} = \{x_d, y_d, \theta_d, m_d, p_d, q_d\}^T. \tag{2.39}$$

Combining $\boldsymbol{u}$ and $\boldsymbol{v}$, and using the shooting parameters p_{d0}, q_{d0}, and ω^2, the new differential equations are

$$\frac{d\bar{\boldsymbol{u}}}{ds} = \left\{ \begin{array}{c} \boldsymbol{g} \\ \frac{d\boldsymbol{g}}{d\hat{\boldsymbol{u}}} \frac{\partial \hat{\boldsymbol{u}}}{\partial p_{d0}} \\ \frac{d\boldsymbol{g}}{d\hat{\boldsymbol{u}}} \frac{\partial \hat{\boldsymbol{u}}}{\partial q_{d0}} \\ \frac{d\boldsymbol{g}}{d\hat{\boldsymbol{u}}} \frac{\partial \hat{\boldsymbol{u}}}{\partial (\omega^2)} \end{array} \right\}, \quad \bar{\boldsymbol{u}} = \left\{ \begin{array}{c} \boldsymbol{u} \\ \frac{\partial \hat{\boldsymbol{u}}}{\partial p_{d0}} \\ \frac{\partial \hat{\boldsymbol{u}}}{\partial q_{d0}} \\ \frac{\partial \hat{\boldsymbol{u}}}{\partial (\omega^2)} \end{array} \right\}. \tag{2.40}$$

Each term of $d\bar{\mathbf{u}}/ds$ in Eqs. (2.40) is given by

$$\boldsymbol{g} = \left\{ \begin{array}{c} \cos\theta_e \\ \sin\theta_e \\ m_e - \sigma \\ \pi^2 \left(-q_0 \cos\theta_e + p_0 \sin\theta_e - Q\cos\theta_e H(s - l_Q)\right) \\ -\theta_d \sin\theta_e \\ \theta_d \cos\theta_e \\ m_d \\ \pi^2 \left((p_0\theta_d - q_d)\cos\theta_e + (p_d + q_0\theta_d)\sin\theta_e + Q\theta_d \sin\theta_e H(s - l_Q)\right) \\ -\omega^2 x_d \\ -\omega^2 y_d \\ 1 \end{array} \right\}, \tag{2.41}$$

$$
\frac{d\boldsymbol{g}}{d\hat{\boldsymbol{u}}}\frac{\partial\hat{\boldsymbol{u}}}{\partial p_{d0}} = \begin{Bmatrix} -\sin\theta_e \frac{\partial\theta_d}{\partial p_{d0}} \\ \cos\theta_e \frac{\partial\theta_d}{\partial p_{d0}} \\ \frac{\partial m_d}{\partial p_{d0}} \\ \pi^2\left((q_0\sin\theta_e + p_0\cos\theta_e + Q\sin\theta_e H(s-l_Q))\frac{\partial\theta_d}{\partial p_{d0}} + \sin\theta_e\frac{\partial p_d}{\partial p_{d0}} - \cos\theta_e\frac{\partial q_d}{\partial p_{d0}}\right) \\ -\omega^2\frac{\partial x_d}{\partial p_{d0}} \\ -\omega^2\frac{\partial y_d}{\partial p_{d0}} \end{Bmatrix}, \tag{2.42}
$$

$$
\frac{d\boldsymbol{g}}{d\hat{\boldsymbol{u}}}\frac{\partial\hat{\boldsymbol{u}}}{\partial q_{d0}} = \begin{Bmatrix} -\sin\theta_e \frac{\partial\theta_d}{\partial q_{d0}} \\ \cos\theta_e \frac{\partial\theta_d}{\partial q_{d0}} \\ \frac{\partial m_d}{\partial q_{d0}} \\ \pi^2\left((q_0\sin\theta_e + p_0\cos\theta_e + Q\sin\theta_e H(s-l_Q))\frac{\partial\theta_d}{\partial q_{d0}} + \sin\theta_e\frac{\partial p_d}{\partial q_{d0}} - \cos\theta_e\frac{\partial q_d}{\partial q_{d0}}\right) \\ -\omega^2\frac{\partial x_d}{\partial q_{d0}} \\ -\omega^2\frac{\partial y_d}{\partial q_{d0}} \end{Bmatrix}, \tag{2.43}
$$

$$
\frac{d\boldsymbol{g}}{d\hat{\boldsymbol{u}}}\frac{\partial\hat{\boldsymbol{u}}}{\partial(\omega^2)} = \begin{Bmatrix} -\sin\theta_e \frac{\partial\theta_d}{\partial(\omega^2)} \\ \cos\theta_e \frac{\partial\theta_d}{\partial(\omega^2)} \\ \frac{\partial m_d}{\partial(\omega^2)} \\ \pi^2\left((q_0\sin\theta_e + p_0\cos\theta_e + Q\sin\theta_e H(s-l_Q))\frac{\partial\theta_d}{\partial(\omega^2)} + \sin\theta_e\frac{\partial p_d}{\partial(\omega^2)} - \cos\theta_e\frac{\partial q_d}{\partial(\omega^2)}\right) \\ -\omega^2\frac{\partial x_d}{\partial p_{d0}} - x_d \\ -\omega^2\frac{\partial y_d}{\partial p_{d0}} - y_d \end{Bmatrix}. \tag{2.44}
$$

The vector of objective functions, $\boldsymbol{f}(\boldsymbol{\alpha})$, is now defined for dynamic quantities of the beam:

$$
\boldsymbol{f}(\boldsymbol{\alpha}) = \begin{Bmatrix} x_d(1,\boldsymbol{\alpha}) \\ y_d(1,\boldsymbol{\alpha}) \\ \theta_d(1,\boldsymbol{\alpha}) \end{Bmatrix}. \tag{2.45}
$$

The Jacobian matrix for dynamic quantities can be found from $\frac{\partial\hat{\boldsymbol{u}}}{\partial\alpha_i}$ in Eqs. (2.40), i.e.,

$$
\boldsymbol{J}_{\boldsymbol{\alpha}_k} = \begin{bmatrix} \frac{\partial x_d}{\partial p_{d0}} & \frac{\partial x_d}{\partial q_{d0}} & \frac{\partial x_d}{\partial(\omega^2)} \\ \frac{\partial y_d}{\partial p_{d0}} & \frac{\partial y_d}{\partial q_{d0}} & \frac{\partial y_d}{\partial(\omega^2)} \\ \frac{\partial\theta_d}{\partial p_{d0}} & \frac{\partial\theta_d}{\partial q_{d0}} & \frac{\partial\theta_d}{\partial(\omega^2)} \end{bmatrix}_{s=1}. \tag{2.46}
$$

The natural frequency squared can be iterated by solving Eqs. (2.40) with initial guess of $\bar{\boldsymbol{u}}_0 = \{0, 0, 0, m_0, 0, 0, 0, m_{d0}, p_{d0}, q_{d0}, 0, 0, 0, 0, 0, 1, 0, 0, 0, 0, 0, 0, 1, 0, 0, 0, 0, 0, 0\}^T$, and the Newton iteration equation Eq. (2.32), where m_{d0} is the dynamic moment at the left end, which is set to be 10^{-9}.

2.4 Potential Energy of the Composite Beam

The potential energy ($\mathcal{P}^*$) of the actuated beam is the sum of the energy stored in the composite ($\mathcal{B}^*$) and the negative work (W) applied by the external force. Without external or dissipative forces, the energy stored in the composite is the strain energy, Π, minus the internal electrical energy of the piezoelectric, (W_p) [116]. The strain energy is the elastic energy stored in the deformed structure. It is computed by integrating strain energy density over the entire volume of the beam [122]. The strain energy density of the post-buckled composite beam is given by

$$d\Pi = \frac{1}{2} TSdU = \frac{1}{2} T_s S_p dU_s + \frac{1}{2} T_p S_p dU_p, \tag{2.47}$$

where $S_p = y^* \frac{d\theta}{ds^*}$ is the bending strain in the composite, and U_s and U_p are volumes of the substrate and the piezoelectric material, respectively. The total strain energy of the composite is

$$\Pi = \int_U d\Pi dU = \frac{1}{2} \left(\int_{U_s} T_s S_p dU_s + \int_{U_p} T_p S_p dU_p \right). \tag{2.48}$$

Substituting stress S_p, $T_s = Y_s y^* \frac{d\theta}{ds^*}$, and Eq. (2.4) into Eq. (2.48) leads to

$$\begin{aligned} \Pi =& \frac{Y_s b}{2} \int_0^l \int_{-\frac{h_s}{2} - y_0}^{\frac{h_s}{2} - y_0} \left(y^* \frac{d\theta}{ds^*} \right)^2 dy^* ds^* \\ &+ \frac{Y_p b}{2} \int_0^l \int_{\frac{h_s}{2} - y_0}^{\frac{h_s}{2} + h_p - y_0} y^* \frac{d\theta}{ds^*} \left(y^* \frac{d\theta}{ds^*} + \frac{d_{33} V}{l_p} \right) dy^* ds^*, \end{aligned} \tag{2.49}$$

$$\begin{aligned} \Pi =& \frac{bY_s}{2} \int_0^l \int_{-\frac{h_s}{2} - y_0}^{\frac{h_s}{2} - y_0} y^{*2} \left(\frac{d\theta}{ds^*} \right)^2 dy^* ds^* \\ &+ \frac{bY_p}{2} \int_0^l \int_{\frac{h_s}{2} - y_0}^{\frac{h_s}{2} + h_p - y_0} \left(y^{*2} \left(\frac{d\theta}{ds^*} \right)^2 + \frac{d_{33} V}{l_p} y^* \frac{d\theta}{ds^*} \right) dy^* ds^*. \end{aligned} \tag{2.50}$$

Evaluating Eq. (2.50), three separate terms are obtained

$$\begin{aligned} A_1 &= \frac{bY_s}{2}\int_0^l \int_{-\frac{h_s}{2}-y_0}^{\frac{h_s}{2}-y_0} y^{*2}\left(\frac{d\theta}{ds^*}\right)^2 dy^* ds^* \\ &= \frac{bY_s}{2}\left(\frac{h_s^3}{12}+h_s y_0^2\right)\int_0^l \left(\frac{d\theta}{ds^*}\right)^2 ds^*, \end{aligned} \tag{2.51}$$

$$\begin{aligned} B_1 &= \frac{bY_p}{2}\int_0^l \int_{\frac{h_s}{2}-y_0}^{\frac{h_s}{2}+h_p-y_0} y^{*2}\left(\frac{d\theta}{ds^*}\right)^2 dy^* ds^* \\ &= \frac{bY_p}{2}\left(\frac{h_p^3}{12}+h_p\left(\frac{h_s+h_p}{2}-y_0\right)^2\right)\int_0^l \left(\frac{d\theta}{ds^*}\right)^2 ds^*, \end{aligned} \tag{2.52}$$

$$\begin{aligned} B_2 &= \frac{bY_p}{2}\int_0^l \int_{\frac{h_s}{2}-y_0}^{\frac{h_s}{2}+h_p-y_0} \frac{d_{33}V}{l_p} y^* \frac{d\theta}{ds^*} dy^* ds^* \\ &= \frac{bY_p d_{33} h_p (h_s+h_p-2y_0)}{4l_p}\int_0^l V\frac{d\theta}{ds^*} ds^*. \end{aligned} \tag{2.53}$$

Converting Eq. (2.7) to $d\theta/ds^* = m^*/YI - \chi V/YI$ and substituting it and Eqs. (2.8) and (2.9) into Eqs. (2.51)–(2.53) gives

$$\begin{aligned} A_1 + B_1 &= \frac{1}{2}YI\int_0^l \left(\frac{m^*}{YI}-\frac{\chi V}{YI}\right)^2 ds^* = \frac{1}{2YI}\int_0^l (m^*-\chi V)^2 ds^*, \\ B_2 &= \frac{1}{2}\chi\int_0^l V\left(\frac{m^*}{YI}-\frac{\chi V}{YI}\right) ds^* = \frac{1}{2YI}\int_0^l (m^*\chi V - \chi^2 V^2) ds^*. \end{aligned} \tag{2.54}$$

The strain energy of the composite can then be simplified to

$$\begin{aligned} \Pi &= A_1 + B_1 + B_2 \\ &= \frac{1}{2YI}\int_0^l (m^*-\chi V)^2 ds^* + \frac{1}{2YI}\int_0^l (m^*\chi V - \chi^2 V^2) ds^* \\ &= \frac{1}{2YI}\int_0^l (m^{*2} - m^*\chi V) ds^*. \end{aligned} \tag{2.55}$$

The internal electrical energy of the piezoelectric is given by [116]

$$W_p = \frac{1}{2}\int\limits_{U_p} E_p D_p dU_p, \tag{2.56}$$

which from Eq. (2.3) can be written as

$$W_p = \frac{1}{2}\int\limits_{U_p} \frac{V}{l_p}\left(-Y_p d_{33} y^* \frac{d\theta}{ds^*} + \bar{\varepsilon}_{33}^S \frac{V}{l_p}\right) dU_p, \tag{2.57}$$

$$W_p = \frac{b}{2}\int_0^l \int_{\frac{h_s}{2}-y_0}^{\frac{h_s}{2}+h_p-y_0} \frac{V}{l_p}\left(-Y_p d_{33} y^* \frac{d\theta}{ds^*} + \bar{\varepsilon}_{33}^S \frac{V}{l_p}\right) dy^* ds^*. \tag{2.58}$$

Evaluating Eq. (2.58), leads to $W_p = -B_2 + C_1$, where C_1 given by

$$C_1 = \frac{b}{2}\int_0^l \int_{\frac{h_s}{2}-y_0}^{\frac{h_s}{2}+h_p-y_0} \left(\bar{\varepsilon}_{33}^S \frac{V^2}{l_p^2}\right) dy^* ds^* = \frac{b h_p \bar{\varepsilon}_{33}^S}{2 l_p^2}\int_0^l V^2 ds^*. \tag{2.59}$$

The internal electrical energy is then simplified to

$$W_p = -B_2 + C_1 = \frac{1}{2}\int_0^l \left(-\frac{\chi V}{YI}(m^* - \chi V) + \psi V^2\right) ds^*, \tag{2.60}$$

where ψ is an energy coefficient due to electromechanical coupling, defined as

$$\psi = \frac{b h_p \bar{\varepsilon}_{33}^S}{l_p^2}. \tag{2.61}$$

The energy stored in the composite is therefore

$$\mathcal{B}^* = \Pi - W_p = \frac{1}{2}\int_0^l \left(\frac{m^{*2}}{YI} - \left(\psi + \frac{\chi^2}{YI}\right) V^2\right) ds^*. \tag{2.62}$$

Eq. (2.62) gives energy when the piezoelectric material is active. For the unactuated case, the energy, $\mathcal{B}^*$, simplifies to the strain energy in the composite:

$$\mathcal{B}^* = \Pi = \frac{1}{2}\int_0^l \frac{m^{*2}}{YI} ds^*. \tag{2.63}$$

If the thickness of the piezoelectric film is assumed to be zero, the flexural rigidity simplifies to the flexural rigidity of the substrate, i.e., $Y_s I = Y_s b h_s^3/12$.

Applying an external mechanical force to the beam, the total potential energy is

$$\mathcal{P}^* = \mathcal{B}^* - W = \frac{1}{2}\int_0^l \left(\frac{m^{*2}}{YI} - \left(\psi + \frac{\chi^2}{YI}\right) V^2\right) ds^* - Q^* \Delta y^*, \tag{2.64}$$

where Δy^* is the deflection at the point of loading. Using non-dimensional parameters m, s, σ, Q and Δy, Eq. (2.64) can be converted to a dimensionless quantity:

$$\begin{aligned}\mathcal{P}^* &= \frac{1}{2}\int_0^l \left(\frac{YIm^2}{l^2} - \left(\psi + \frac{\chi^2}{YI}\right)\frac{YI^2\sigma^2}{\chi^2 l^2}\right) d(ls) - \frac{\pi^2 YI}{l^2} Ql\Delta y \\ &= \frac{YI}{2l}\int_0^1 \left(m^2 - \left(\frac{YI\psi}{\chi^2} + 1\right)\sigma^2\right) ds - \frac{\pi^2 YI}{l} Q\Delta y,\end{aligned} \tag{2.65}$$

$$\mathcal{P} = \frac{l\mathcal{P}^*}{YI} = \frac{1}{2}\int_0^1 \left(m^2 - \left(\frac{YI\psi}{\chi^2} + 1\right)\sigma^2\right) ds - \pi^2 Q\Delta y. \tag{2.66}$$

For unloaded cases, the potential energy simplifies to the energy stored in the composite, $\mathcal{P} = \mathcal{B}$, where $\mathcal{B} = l\mathcal{B}^*/YI$.

2.5 Conclusions

The elastica model of a clamped-clamped beam is extended to account for the effects of piezoelectric actuation. The model can be exercised across a large configuration space to uncover the topologies and actuation strategies that change structural stability most profoundly. The model development begins with the bending moment of the composite beam, and finds the non-dimensional equilibrium equations. Static equilibria and their stability are computed using a Runge-Kutta numerical integration and a shooting method. The potential energy of the composite is derived to provide another means of assessing the stability of the system.

Chapter 3

Changing the Critical Snap-Through Loads of Post-buckled Beams

3.1 Overview and Theory

This chapter studies the extent to which the strategic placement and actuation of piezoelectric materials bonded to clamped-clamped post-buckled beams can influence the loads at which snap-through occurs. The electromechanical system is modeled using elastica theory with an extension to account for the influence of piezoelectric actuation. The results indicate that the effect of piezoelectric actuation on critical snap-through load depends on the degree to which the beam is buckled, the location of the external load, the placement of the piezoelectric material, and the applied actuation voltage. Experiments are performed to validate the numerical results and provide a physical demonstration of changing snap-through loads with piezoelectric actuation. Experimental results demonstrate that critical snap-through loads can be altered by factors ranging from 0.4 to 2.0, and numerical results indicate that even larger changes to snap-through loads are physically realizable.

An inextensible beam is assumed to be post-buckled and clamped both ends, as shown in Fig 3.1. Piezoelectric material is assumed to cover the top surface of the beam across its entire span. The voltage, V, is applied to the piezoelectric patch. The actuation patch length is variable. The actuation region (patch span) is specified with the parameters, sp_1 and sp_2, which denote the percent of span between $s = 0$ and the beginning of the actuated region, and between $s = 1$ and the end of the actuated region, respectively.

The non-dimensional parameter σ captures the effect of piezoelectric actuation, which is proportional to the voltage on the beam.

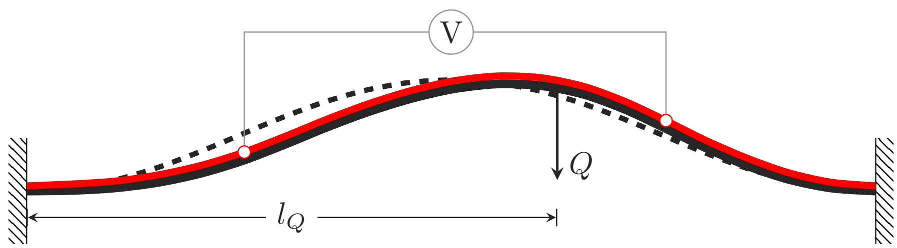

Figure 3.1. Schematic of a clamped-clamped post-buckled beam bonded with one piezoelectric patch on its top surface.

Equilibrium shapes and stability are calculated for various values of Q and σ using the model presented in Chapter 2; however, it is helpful to evaluate some practical limits on the value of σ to determine what values might be realistically achievable. The definition of σ is given as part of Eqs. (2.10). It can be evaluated with knowledge of the thicknesses and Young's moduli of the subratrate and piezoelectric material along with knowledge of d_{33}, V, l_p. For the P1-type (elongating) MFC, $d_{33} = 460$ pm/V, $Y_p = 30.34$ GPa, $h_p = 0.3$ mm, $l_p = 0.45$ mm, and the maximum/minimum actuation voltages are 1500/-500 volts [123]. Fig. 3.2 shows the value of σ/l versus the substrate thickness, h_s, assuming a steel substrate ($Y_s = 200$ GPa). This assumes the piezoelectric material is bonded to the top of the beam and actuated with 1500 and -500 volts.

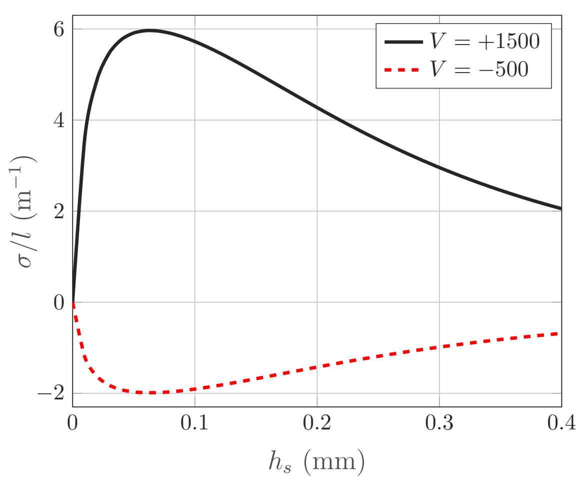

Figure 3.2. Value of σ/l versus the thickness of the substrate, h_s for the steel substrate.

In the subsequent results, the values of σ are limited to a range of -0.8 to 2. This is consistent with beams with a steel substrate, and where $h_s \approx 0.25$ mm and $l \approx 0.6$ m. The piezoelectric material is assumed to cover the entire beam, but only a portion is actuated. In practice, this can be achieved by bonding several patches of piezoelectric material to the entire beam, but actuating only some of the patches.

3.2 Load-Deflection Curves and Stability Analysis

Load-deflection curves and their corresponding natural frequency maps are shown in Figs. 3.3-3.5 for three end shortening values ($e = 0.01$, 0.05, 0.10). For each value of end shortening, $\sigma = 0$ and $\sigma = 2$ cases are considered. Deflection is shown in terms of the non-dimensional mid-point deflection, δ, normalized by the mid-point deflection, δ_0, when $Q = 0$. For the three values of e, these normalization constants are found to be $\delta_0 = 0.0635$, 0.1401, and 0.1949. In each case, the load is located at the mid-point ($l_Q = 0.5$) and piezoelectric material from 25% to 75% of span is assumed to be actuated.

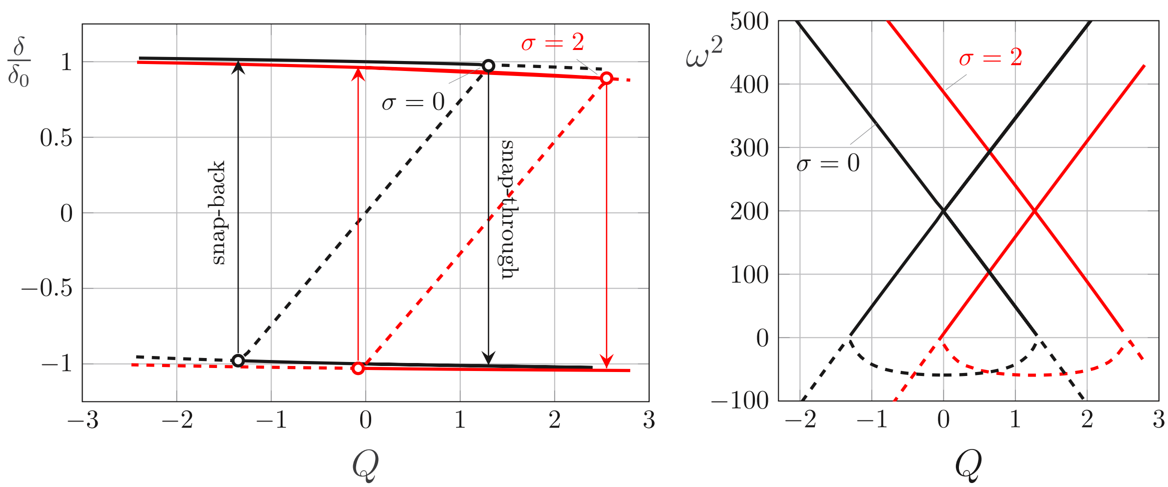

(a) (b)

Figure 3.3. (a) Normalized mid-point deflection, δ/δ_0, and (b) non-dimensional natural frequency squared, ω^2, versus non-dimensional load, Q, for $e = 0.01$, $\sigma = 0$ (black) and $\sigma = 2$ (red). Stable (unstable) paths are indicated with solid (dashed) lines.

In each case, the load-deflection curves show an increase in critical snap-through load when the piezoelectric material is actuated. In fact, the difference between the non-dimensional critical snap-through loads with and without actuation is the same for all three values of end shortening (i.e., $Q_{cr}(\sigma = 2) - Q_{cr}(\sigma =$

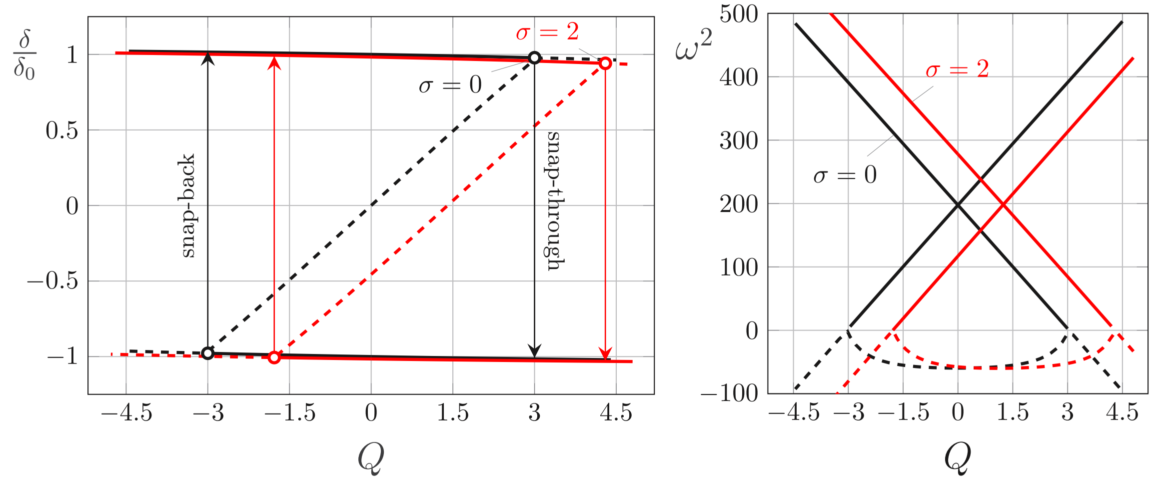

(a) (b)

Figure 3.4. (a) Normalized mid-point deflection, δ/δ_0, and (b) non-dimensional natural frequency squared, ω^2, versus non-dimensional load, Q, for $e = 0.05$, $\sigma = 0$ (black) and $\sigma = 2$ (red). Stable (unstable) paths are indicated with solid (dashed) lines.

$0) = 1.24$). However, since critical load increases with increasing end shortening, the percentage increase in critical load under actuation decreases as end shortening increases. Similarly, the effect of actuation on the mid-point position at snap-through diminishes with increases to end shortening. When $e = 0.01$, the normalized mid-point position at snap-through is 0.89 with actuation and 0.98 without (in Fig. 3.3(a)). When $e = 0.10$, this difference is significantly reduced, and the normalized mid-point position at snap-through are 0.95 and 0.97 with and without actuation (in Figs. 3.5(a)).

The natural frequency maps in Figs. 3.3(b)-3.5(b) show that, under actuation, the curves representing natural frequency shift to the right (i.e., toward higher values of Q). A consequence of this shift is that upon unloading, the load at which the snap-back occurs is higher than it might otherwise be. In other words, the region of hysteresis has roughly the same area regardless of whether actuation is used. The implication here is that under dynamic loading, the effect of a constantly applied voltage may not appreciably change the forcing amplitudes and frequencies at which the system exhibits persistent snap-through. One possible strategy for expanding the hysteresis region (and thus raise the boundary of persistent snap-through) would be to apply a voltage in the structure's original configuration and then reverse it in the structure's snapped configuration. Investigating the effectiveness of this strategy is a subject for future work.

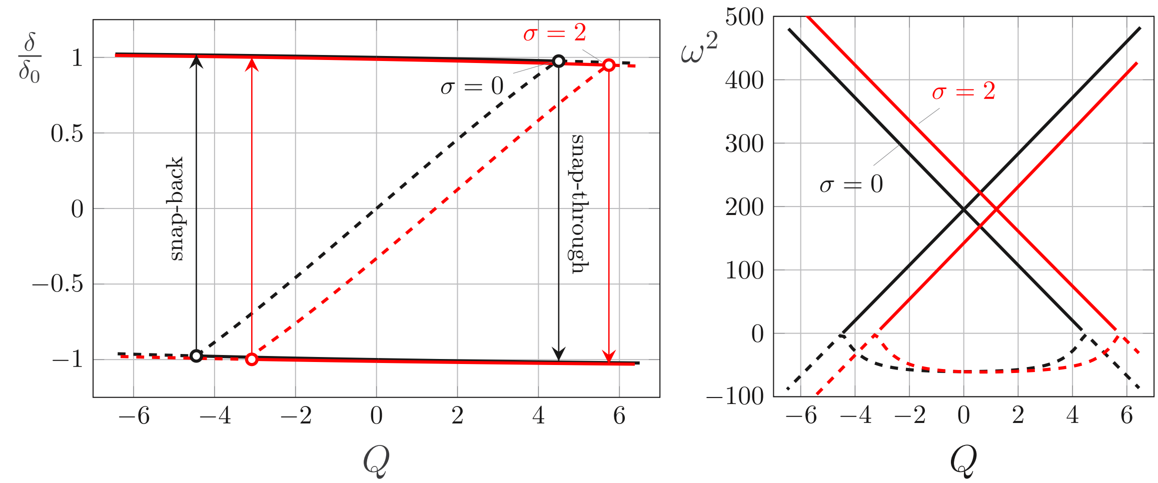

(a) (b)

Figure 3.5. (a) Normalized mid-point deflection, δ/δ_0, and (b) non-dimensional natural frequency squared, ω^2, versus non-dimensional load, Q, for $e = 0.10$, $\sigma = 0$ (black) and $\sigma = 2$ (red). Stable (unstable) paths are indicated with solid (dashed) lines.

3.3 Parameter Study of Changing Critical Loads

3.3.1 Effects of End Shortening and Actuation Voltage

The influence of end shortening and actuation voltage on critical snap-through load are studied for the case in which the external load is positioned at the beam mid-point ($l_Q = 0.5$) and the piezoelectric material is actuated from 25% to 75% of span. Fig. 3.6 shows the non-dimensional critical snap-through load versus the non-dimensional electromechanical coupling parameter for various values of end shortening. Consistent with the fact that the electromechanical coupling parameter manifests in the equilibrium equations in a manner akin to an initial imperfection, the results indicate a linear relationship between critical load and electromechanical coupling. As suggested by the load-deflection results in Fig. 3.3-3.5, the slopes of lines in Fig. 3.6 are equivalent.

Fig. 3.7 shows how critical snap-through loads and the corresponding mid-point deflection at snap-through vary with end shortening. In Fig. 3.7 (a), the critical load factor ($Q_{cr}(\sigma)/Q_{cr}(0)$) is computed across a range of e values. The results indicate that, relative to the unactuated case, actuation is most

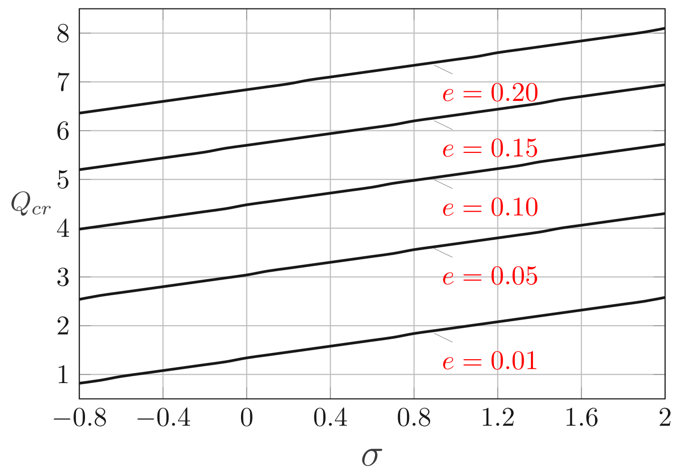

Figure 3.6. Theoretical critical snap-through loads, Q_{cr}, versus electromechanical coupling parameter, σ, with $l_Q = 0.5$ and different end shortenings. The piezoelectric material is actuated from 25% to 75% of span.

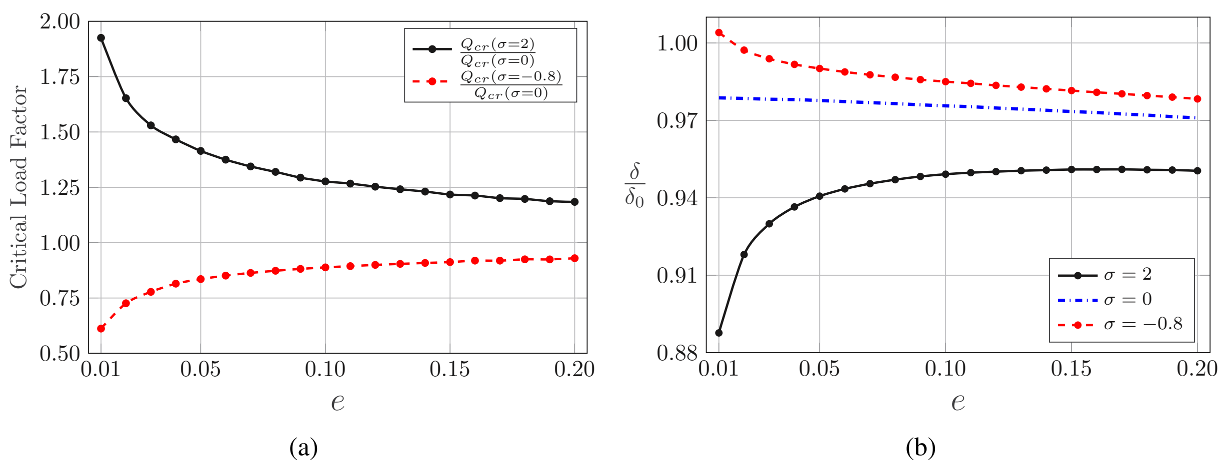

Figure 3.7. (a) Theoretical critical snap-through load factor versus non-dimensional end shortening, e, with electromechanical coupling parameter, $\sigma = -0.8$ and $\sigma = 2$. (b) Mid-point deflection at critical snap-through load versus non-dimensional end shortening, e, with $\sigma = -0.8$, $\sigma = 0$, and $\sigma = 2$. The piezoelectric material is actuated from 25% to 75% of span and the load is located at the mid-point ($l_Q = 0.5$).

effective in changing critical loads for low values of end shortening. For $e > 0.10$, actuation is relatively ineffective. Similarly, actuation does little to influence the mid-point position at snap-through when e is large. However, for small values of e, the difference between the mid-point positions at snap-through in the actuated and unactuated cases is considerable. This trend was also observed in load-deflection curves.

3.3.2 Effects of Load Location

In this part of the parameter study, the end shortening, the electromechanical coupling parameter, and the region of actuation are held fixed while the location of the point load are varied. The piezoelectric material is again assumed to cover the entire top surface of the beam, but only a portion of the material is actuated. In general, the actuated region can be discontinuous and a different voltages applied to each patch; however, in the present study, attention is restricted to continuous actuation regions with a constant applied voltage. In an early study using MFC to induce snap-through in post-buckled beams, Cazottes et al. found that actuator position had a strong influence on the actuation voltages required to achieve snap-through [62].

Fixing the end shortening at $e = 0.05$, and varying σ, the non-dimensional critical snap-through loads and their corresponding factor ($Q_{cr}(\sigma)/Q_{cr}(0)$) are shown versus load location in Fig. 3.8. Results are shown for three different actuation regions: $sp_1 = 20\%$, $sp_2 = 40\%$; $sp_1 = sp_2 = 25\%$; and $sp_1 = 50\%$, $sp_2 = 20\%$. Four different values of σ ranging from -0.8 to 2.0 are considered. For the unactuated ($\sigma = 0$) case, the critical loads are independent of the actuation region, and the curve has a local maximum when the external load is applied at the mid-point [124].

Considering the case in which the actuation region is symmetric about the center of the beam (Fig. 3.8 (c) and (d)), it is observed that the critical snap-through load curves are symmetric about $l_Q = 0.5$. Here, actuation shifts these curves vertically, with positive values of σ increasing snap-through loads and negative values decreasing them. Comparing actuated snap-through loads relative to the unactuated snap-through loads in Fig. 3.8 (d) it is observed that actuation is more effective at changing critical loads when the external force is applied away from the mid-point.

The situation is more complicated when the actuation region is not symmetric about the center of the beam. Fig. 3.8 (a) and (b) correspond to the case in which the actuation is from 20% to 60% of span. Here, positive values of σ have the effect of shifting the local maximum toward lower values of l_Q and increasing snap-through loads when l_Q is less than about 0.45. A negative value of σ has the converse effect. When $l_Q > 0.6$ (i.e., the load is located beyond the actuation region), actuation has only a small effect on critical load. In Fig. 3.8 (b), the maximum critical load factors occur at the same values of l_Q as the local maxima in Fig. 3.8 (a). For large positive values of σ, snap through loads can be increased by factors greater than two while negative values of σ can result critical load factors as low as 0.5. As l_Q increases beyond the values

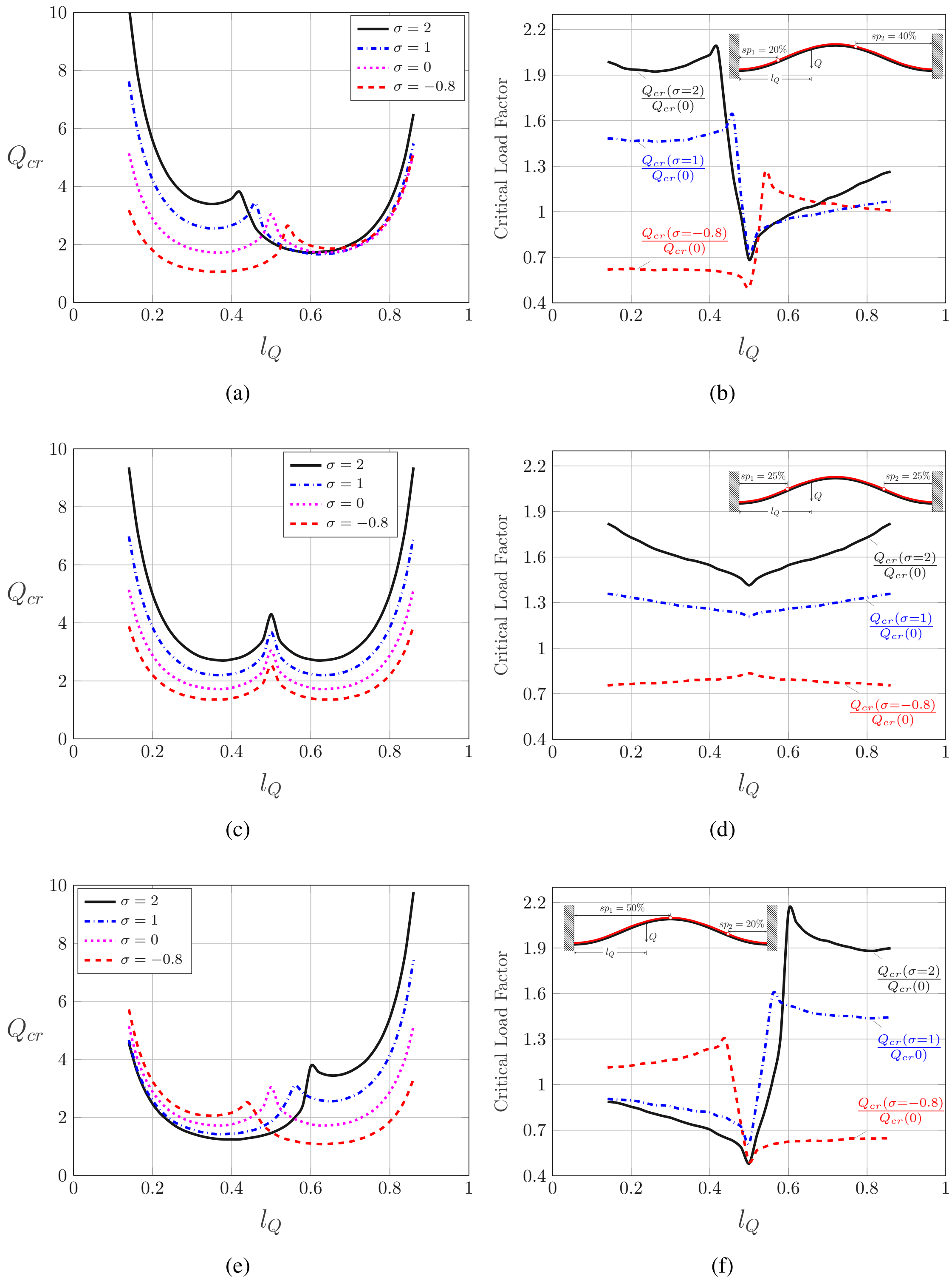

Figure 3.8. Theoretical critical snap-through loads and load factors versus non-dimensional load placement, l_Q, with the end shortening $e = 0.05$. The piezoelectric material is actuated from: (a) and (b) 20% to 60% of span, (c) and (d) 25% to 75% of span, (e) and (f) 50% to 80% of span.

corresponding to the local maxima in the critical snap-through load curves, critical load factors decrease sharply for positive values of σ and increase sharply for negative σ values. This indicates that piezoelectric actuation suddenly loses efficacy for load placements just beyond the values corresponding to the local maxima in the critical load curves.

In Fig. 3.8 (e) and (f), the actuation region is from 50% to 80% of span. Positive values of σ have the effect of shifting the local maximum toward higher values of l_Q and increasing snap-through loads when l_Q is greater than about 0.6. Negative values of σ shift the local maximum toward lower values of l_Q. For $l_Q < 0.4$, positive values of σ have the effect of decreasing critical snap-through loads while negative values increase them. In contrast to the previous case, piezoelectric actuation is now most effective for l_Q values above the values corresponding to the local maxima in the critical load curves.

3.3.3 Effects of Actuation Region

Now consider the case of a variable actuation region that is centered at the beam mid-point (i.e., $sp_1 = sp_2$) with $l_Q = 0.5$ and $e = 0.05$. Critical snap-through loads and the normalized mid-point deflection at snap-through are shown in Fig. 3.9. Results in Fig. 3.9 (a) show that, for centered actuation regions with $l_Q = 0.5$, actuation is most effective in changing critical load when the actuation region is from 25% to 75% of span. Note that when the actuation region covers the entire span, the actuation effects cancel and there is no change in critical snap-through loads. In Fig. 3.9 (b), it is observed that when σ is positive and the actuation region is from 25% to 75% of span, the beam mid-point deflections at snap-through are considerably higher than in the case of an unactuated beam; however, for negative values of σ, the mid-point of the actuated beam deflects very little at snap-through. This suggests a link between critical load factor and mid-point deflection at snap-through. Higher critical load factors correspond to large deflections at snap-through, and vice versa.

Surface plots of critical load factors across the range of all possible actuation regions are shown in Fig. 3.10 for $e = 0.05$ and $\sigma = 1$. Results correspond to six different placements of the external load in the range of $0.2 \leqslant l_Q \leqslant 0.5$. Attention is restricted to cases where $l_Q < 0.5$ because results for $l_Q > 0.5$ mirror those for $l_Q < 0.5$. The bounds of the actuation regions are defined in terms of the span percentages sp1 and sp2, which are constrained to obey $sp_1 + sp_2 \leqslant 100\%$. This places all possible actuation regions in a triangular

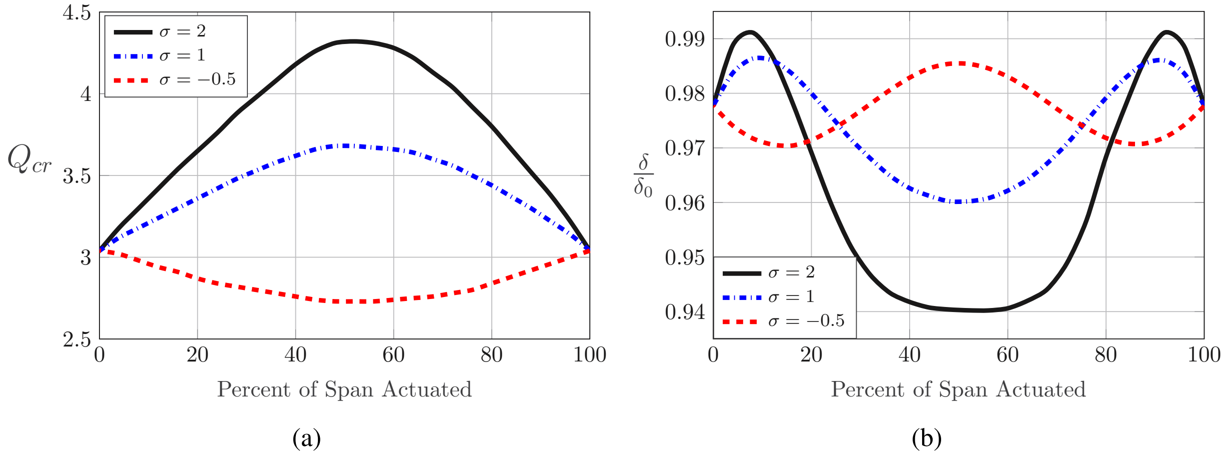

Figure 3.9. (a) Theoretical critical snap-through load and (b) normalized theoretical mid-point deflection versus the percent of span actuated. In all cases, the actuated region is assumed to be centered on the beam, and $e = 0.05$.

area where the (0%, 0%) vertex and the $sp_1 = 100\% - sp_2$ line correspond to an unactuated beam. The (100%, 0%) and (0%, 100%) vertices correspond to an actuation region spanning the entire beam.

The subplots in Fig. 3.10 show that changes to snap-through load due to piezoelectric actuation are sensitive to both actuation region and load placement, especially as l_Q approaches 0.5. As the external load moves from $l_Q = 0.4$ to $l_Q = 0.5$, the area centered near $sp_1 = 20\%, sp_2 = 60\%$ undergoes a transition where actuation regions in this area go from strongly increasing critical load to strongly decreasing it. Interestingly, the area centered near $sp_1 = 60\%, sp_2 = 20\%$ does not undergo a similar transition, with actuation regions in this area decreasing critical snap-through loads regardless of load placement. Consequently, at $l_Q = 0.5$, only a small subset of possible actuation regions can increase critical load.

3.3.4 Accounting for Actuator Weight

It is observed that piezoelectric actuation can increase critical snap-through loads by a factor of two or more. Since the piezoelectric material adds weight, it is reasonable to question whether similar increases in snap-through load can be achieved by simply thickening the substrate such that it has the same mass as the piezoelectrically actuated beam. The answer to this question is configuration specific; yet, some insight can

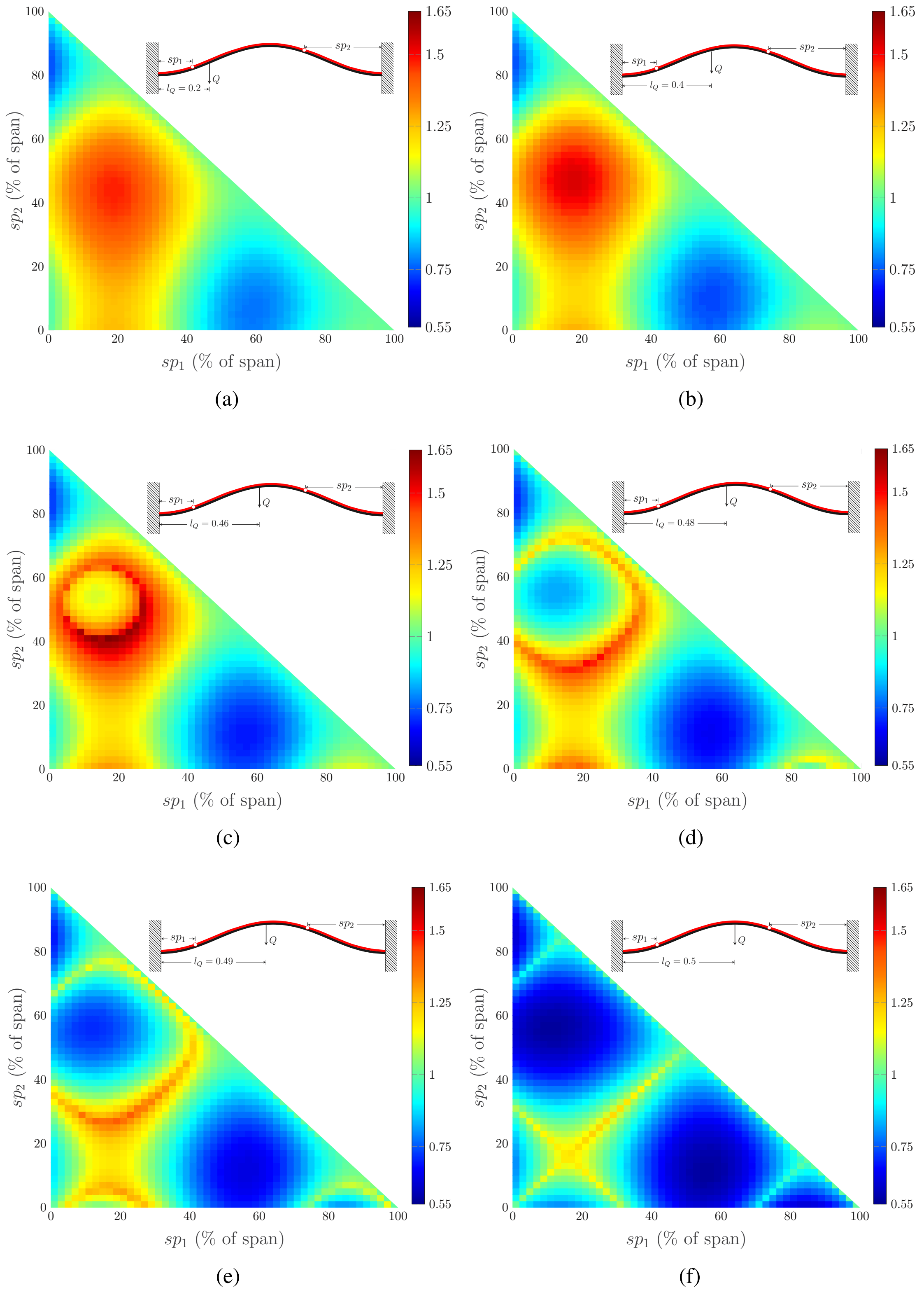

Figure 3.10. Theoretical critical snap-through load factors across the range of possible piezoelectric patch spans, sp_1 and sp_2. The beam is loaded at (a) $l_Q = 0.2$, (b) $l_Q = 0.4$, (c) $l_Q = 0.46$, (d) $l_Q = 0.48$, (e) $l_Q = 0.49$ and (f) $l_Q = 0.50$.

be gained by considering the case of MFC bonded to common substrate materials and actuated in a typical manner.

First, it is recognized that a substrate-only beam will have the same mass as a beam with piezoelectric material covering one side when its thickness is $h_{eq} = h_s + h_p\rho_p/\rho_s$. The corresponding flexural rigidity will be $YI_{eq} = Y_s b h_{eq}^3/12$. Critical snap-through load is proportional to flexural rigidity, so the ratio of the flexural rigidity of the substrate-only equivalent mass beam to that of the unimorph beam (i.e., $\Gamma_{eq} = YI_{eq}/YI$) is the critical snap-through load factor between the two cases. If this factor is higher than the critical load factor corresponding to actuation (denoted Γ_p), than it would likely be more practical to increase snap-through loads by employing a substrate-only equivalent mass beam.

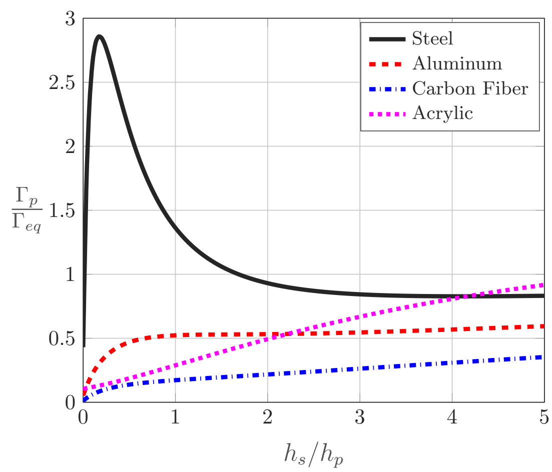

Figure 3.11. Ratio of actuated and mass-equivalent critical load factors for common substrate materials. Here, $e = 0.01$, $V = 1500$ volts, $l = 1$ m, and the actuation region is from 25% to 75% of span.

Fig. 3.11 shows the ratio of Γ_p to Γ_{eq} for some common substrate materials. These curves assume that MFC ($Y_p = 30.34$ GPa, $\rho_p = 5440$ kg/m^3, $h_p = 0.3$ mm) is bonded to one side of the beam across its entire span, and the MFC and the substrate are assumed to have the same width. The actuated critical load factor is taken to be $\Gamma_p = 0.5\sigma + 1$, which corresponds to the $e = 0.01$ line shown in Fig. 3.6 where the actuation region is from 25% to 75% of span. The electromechanical coupling parameter, σ, is calculated using Eqs. (2.8), (2.9), and (2.10) with $V = 1500$ volts and $l = 1$ m. Curves for steel ($Y_s = 200$ GPa, $\rho_s = 7700$ kg/m^3), aluminum ($Y_s = 70$ GPa, $\rho_s = 2700$ kg/m^3), carbon fiber/epoxy composite ($Y_s = 100$ GPa, $\rho_s = 1800$ kg/m^3), and acrylic ($Y_s = 3$ GPa, $\rho_s = 1190$ kg/m^3) substrates are shown versus substrate thickness in the actuated beam, where the thickness is normalized by the MFC thickness.

Critical load ratios less than one suggest that increases in critical load due to piezoelectric actuation likely do not justify the additional weight of the MFC, while ratios greater than one indicate that employing piezoelectric actuation is a weight-saving strategy for increasing snap-through loads. Fig. 3.11 indicates that (at least in the assumed configuration) piezoelectric actuation is a weight-efficient approach to increasing snap-through loads for steel (if $h_s < 2h_p$), but not for aluminum, carbon fiber and acrylic substrates. However, this analysis assumes that the piezoelectric material covers the entire span. Since the largest increases in snap-through load occur when the actuation region covers only a portion of the span, it is likely that in practical applications, only a portion of a span will be covered with piezoelectric material, thus reducing the weight penalty associated with actuation. It is also noted that minimizing weight is not always the singular design objective. In some applications, embedded piezoelectric material can offer energy harvesting and/or health monitoring functionality while also providing a means to control structural stability.

3.4 Experimental Validation

3.4.1 Experimental Setup

To validate the theoretical results and physically demonstrate the ability to change snap-through load with piezoelectric actuation, an experiment is devised. The experimental set up is shown in Fig. 3.12. The test article is a 46 cm by 2 cm by 0.25 mm strip of spring steel ($\rho_s = 7700$ kg/m^3, $Y_s = 200$ GPa). Clamped-clamped post-buckled beams with end shortenings of $e = 0.01$, 0.04, and 0.10 are tested. Two patches of P1-type MFC ($\rho_p = 5440$ kg/m^3, $Y_p = 30.34$ GPa, $d_{33} = 460$ pm/V, and $l_p = 0.45$ mm [123]), each with active dimensions of 8.5 cm by 1.4 cm by 0.3 mm are placed end-to-end and bonded to top of the beam with epoxy. The MFC therefore covers roughly 50% of the beam's span.

Since the MFC partially covers the beam, an effective flexural rigidity of the composite beam is obtained for use when non-dimensionalizing critical load (in lieu of Eq. (2.8)). The effective flexural rigidity is calculated using

$$YI_{eff} = a_1 YI + a_2 YI_s, \tag{3.1}$$

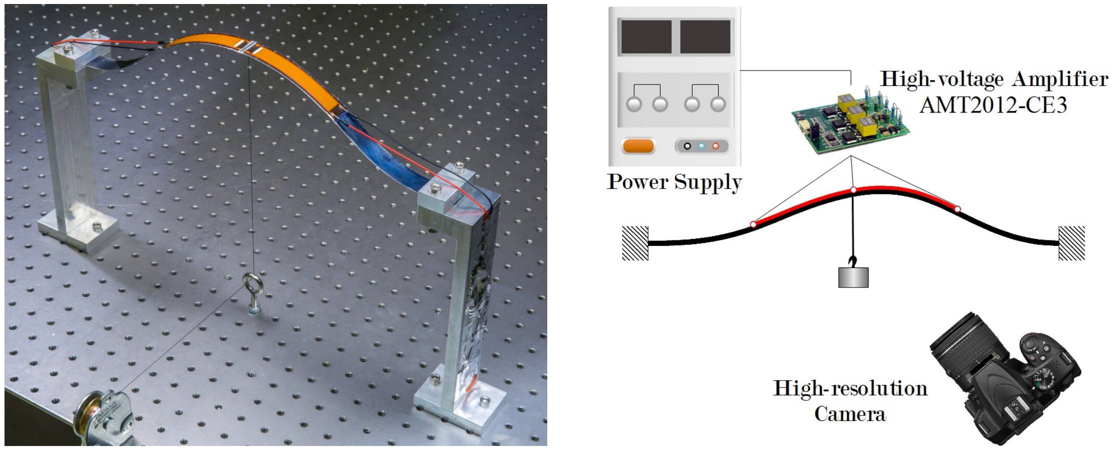

(a) (b)

Figure 3.12. (a) Experimental photo, and (b) schematic of the experimental setup with two MFC patches placed end-to-end at center span, covering roughly the center 50% of the beam.

where a_1 is the fraction of span with piezoelectric material, and a_2 is the fraction without. The flexural rigidity of the substrate is given by $YI_s = Y_s b h_s^3/12$. The effective flexural rigidity and other physical parameters of each tested configuration are shown in Table 3.1.

Table 3.1. Test parameters.

	$e = 0.01$	$e = 0.05$	$e = 0.10$
Length l (cm)	37.20	38.74	41.00
Patch covering span a_1	0.50	0.48	0.45
Effective flexural rigidity (Nm^{-2})	0.0109	0.0106	0.0102
σ with $V = 1200$ V	1.74	1.85	2.03

Force control is achieved by fixing a string to the beam near center span and routing it over a pulley. A container to which small masses are added is attached to the other end of the string and allowed to hang under gravity. Mass is added in 10-30 gram increments until snap-through occurs.

A custom image correlation procedure identifies the edge of the beam from a photograph and digitizes its position. Fig. 3.13 depicts the key steps in the image correlation process for the case of an unloaded and unactuated buckled beam. First, a digital camera is set up to focus on the edge of the beam and high-resolution photographs are obtained after each increment of mass is added (Fig. 3.13(a)). The resulting

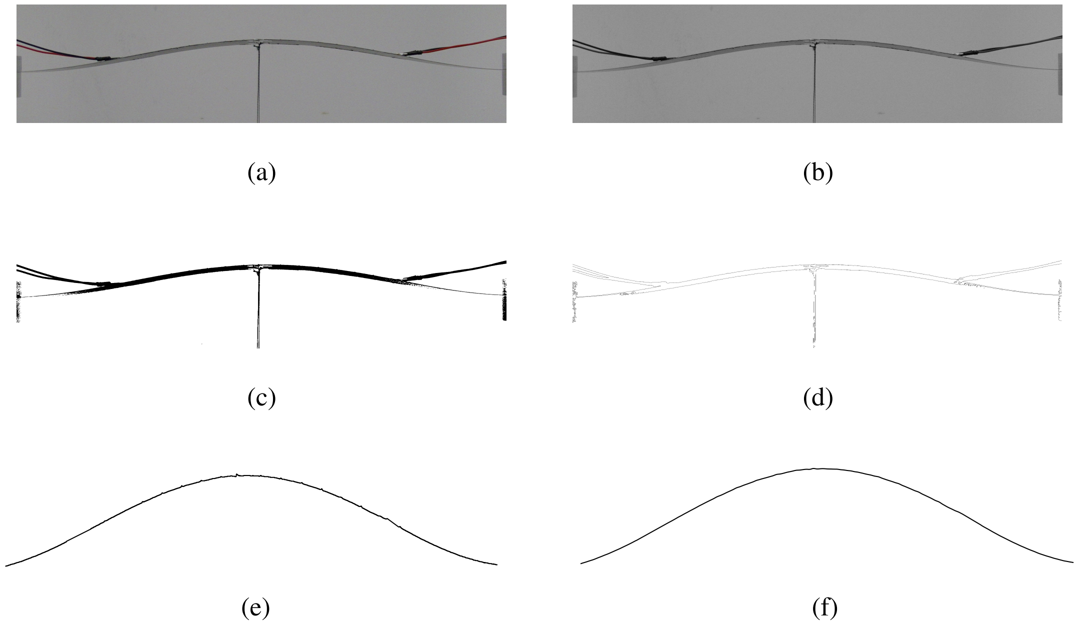

Figure 3.13. Image correlation process of an initially unloaded and unactuated beam for e = 0.01.

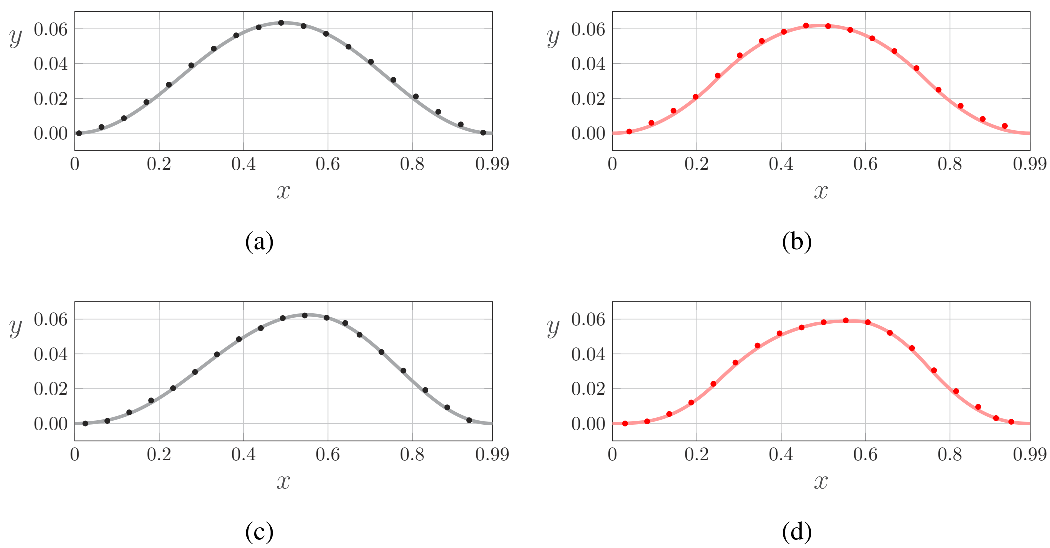

Figure 3.14. Theoretical (line) and experimental (marker) shapes of the unloaded beam for $e = 0.01$. (a) Beam unloaded and unactuated, (b) unactuated beam just prior to snap-through, (c) beam unloaded and actuated with 1200 volts, and (d) actuated beam just prior to snap-through.

true-color images are then converted to gray-scale intensity images (Fig. 3.13(b)) and an intensity threshold is used to convert the intensity images to black and white binary images (Fig. 3.13(c)). A Canny edge detector algorithm native to Matlab [125–127] then operates on the binary images to extract the edges of the black portions of the images. The Canny edge detector uses a multi-stage algorithm to detect a wide range of edges in images. As can be seen from Fig. 3.13(d), not all of the resulting edge data correspond to the beam itself. For instance, the beam supports, the actuator leads, and the string used for loading the beam are all clearly visible. These extraneous edge points are neglected by applying a set of rules that disallow any data found within a set of user-defined regions. Further, since the beam was photographed at a slightly oblique angle, some of the edge data corresponds to the back edge of the beam. This edge data was also ignored and the remaining data result in a digitized beam shape consisting of roughly 3500 points (Fig 3.13(e)). However, the shape of the curve remains somewhat noisy with artifacts from the edge detection algorithm. To smooth the shape, a 50 point moving average is applied and the final digitized beam shape is shown in Fig. 3.13(f). Fig. 3.14 (a) and (b) show image-processed experimental shapes of the unloaded beam, compared with theoretical ones, for the unactuated and actuated 1200 volt cases. Fig. 3.14 (c) and (d) show the corresponding shapes just prior to snap-through.

3.4.2 Theoretical and Experimental Data Comparison

Fig. 3.15 (a)–(c) show load-deflection curves for both unactuated ($V = 0$) and actuated ($V = 1200$ volts) cases across three end shortening values, $e = 0.01$, 0.05, and 0.10. For each value of end shortening, data are shown from three experimental trials. Since the lengths of the three beams are somewhat different, the values of the electromechanical coupling parameter used to generate the theoretical curves are specified to correspond to the given configuration under test, as shown in Table 3.1. The experimental beam shapes obtained via image correlation are numerically integrated to find the beam's mid-point. The corresponding normalized mid-point deflections are shown as the experimental results in Fig. 3.15 (a)–(c). In Fig. 3.15 (d), theoretical and experimental snap-through loads are plotted against voltage.

Across all experimental trials, mid-point deflections in the actuated and unactuated cases correlate well. The absolute percent differences between the theoretical and experimental snap-through loads are tabulated in Table 3.2. Unactuated snap-through loads are predicted within 5%, while the actuated snap-through loads agree even more closely with the theory.

Theoretical and experimental critical snap-through load factors ($Q_{cr}(\sigma)/Q_{cr}(0)$) are shown in Fig. 3.16 versus load location. Here, $e = 0.01$, $\sigma = 1.17$ and -0.58 ($V = 800$ and -400 volts), and the actuation

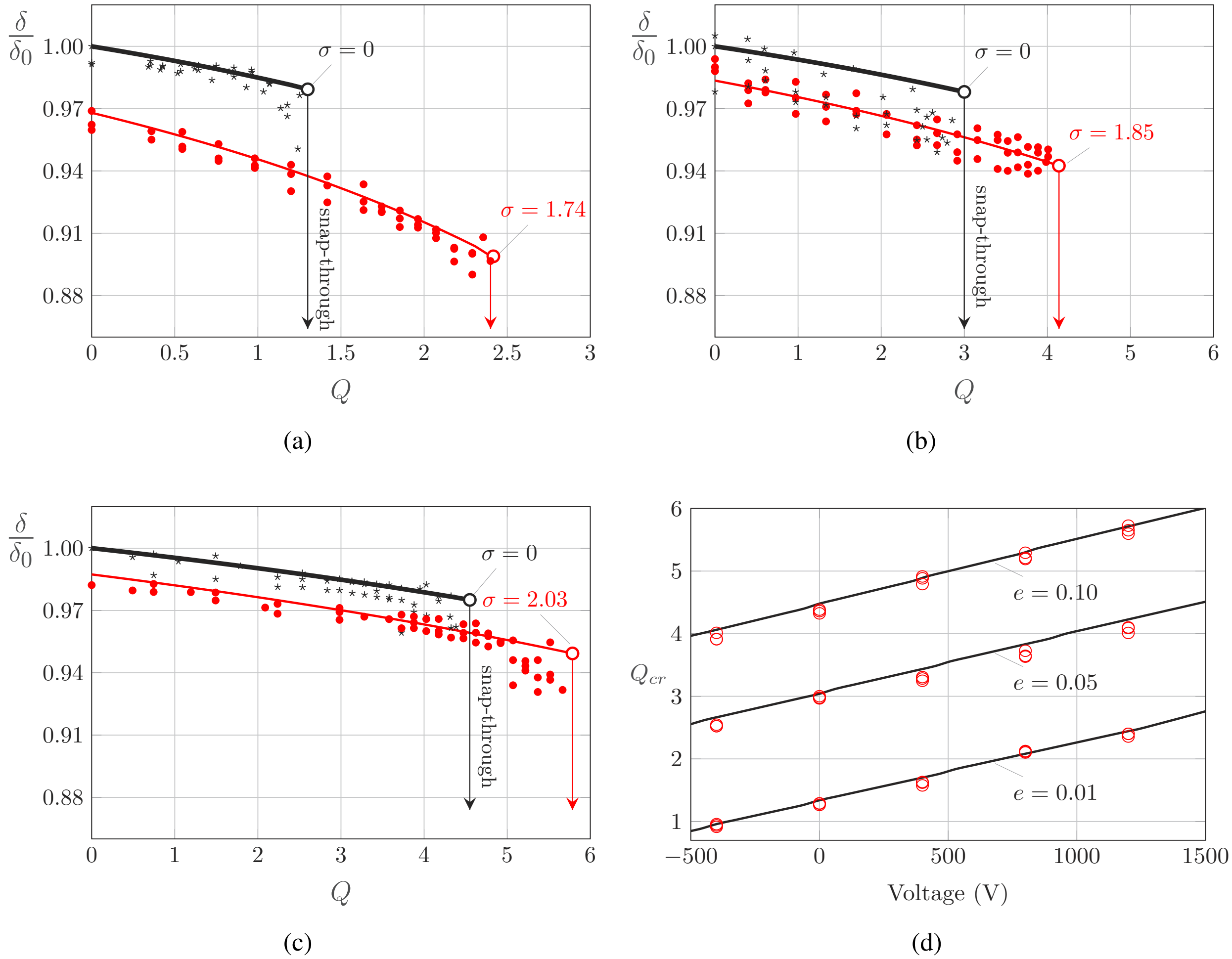

Figure 3.15. Normalized mid-point deflection versus non-dimensional load for unactuated (black) and actuated with 1200 volts (red) cases with three trials of experimental data (markers). (a) $e = 0.01$, $\sigma = 0$ and $\sigma = 1.74$, (b) $e = 0.05$, $\sigma = 0$, and $\sigma = 1.85$, and (c) $e = 0.10$, $\sigma = 0$, and $\sigma = 2.03$. (d) Theoretical critical snap-through loads and experimental data versus voltage for $e = 0.01, 0.05$, and 0.10.

Table 3.2. Average percent error of the experimental and theoretical critical snap-through loads.

	$e = 0.01$	$e = 0.05$	$e = 0.10$
Unactuated	3.07%	2.48%	4.69%
Actuated	1.16%	2.01%	2.91%

region is from 15% to 65% of span ($sp_1 = 15\%$; $sp2 = 35\%$). The clamped-clamped beam for the case of $e = 0.01$ in the first test is shifted to configure the actuation region of 15%–65% on the beam. The

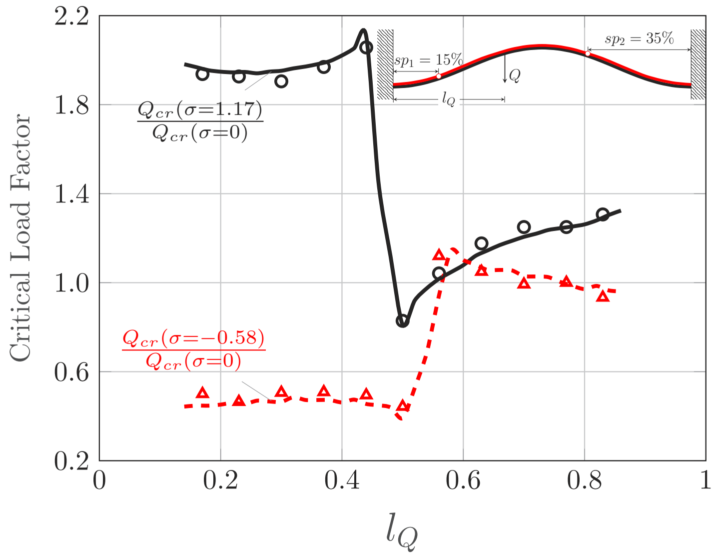

Figure 3.16. Theoretical and experimental critical snap-through load factors versus non-dimensional load location, l_Q, for $e = 0.01$ and $\sigma = 1.17$ and -0.58. Piezoelectric material is actuated from 15% to 65% of span.

experimental results confirm the theoretical behavior first observed in Fig. 3.8. Namely, sharp transitions in critical load factor occur when the load placement is near the center of the actuation region. The experimental data for $\sigma = 1.17$ confirms that when the external load is at roughly 45% of span, actuation doubles the critical snap-through load. However, after moving the external load to 50% of span, actuation decreases critical load by a factor of 0.75. Across all tested load locations, the average absolute percent difference between the theoretical and experimental results is 2.41% for $\sigma = 1.17$ and 6.64% for $\sigma = -0.58$.

3.5 Conclusions

The model presented in Chapter 2 is solved for the case of a point-loaded clamped-clamped beam. The model is cast in non-dimensional terms to enable a general study of the effects piezoelectric actuation on critical snap-through loads. Results are obtained across a large range of end shortenings and load locations. A range of possible actuation regions and actuation voltages are also considered. Experimental trials involving beams with different values of end shortening, different actuation regions, and voltages validate the numerical results across a large parameter space.

The model indicates that the effects of piezoelectric actuation manifest as an electromechanical coupling term, σ, that appears in the equilibrium equations in the same manner as an initial imperfection. Consequently, critical snap-through loads are found to increase linearly with increasing values of σ. Overall, actuation is found to affect critical loads most strongly at small values of end shortening. Critical snap-through loads are also found to exhibit a complicated interplay between the actuation region and the location of the external load, particularly as the load approaches mid-span.

It is expected that the results of this chapter can be used to design structures which have enhanced stability to overcome complex loading environments. One possibility would be to embed piezoelectric actuators into advanced composite materials to enhance their stability as needed. When not actuated, the piezoelectric elements could be used as health monitoring sensors or energy harvesters. These intelligent actuators/sensors could find applications in, for example, aircraft fuselages and in the hulls of ships and submarines.

Chapter 4

Stable Transitions between Remote Equilibria of Post-Buckled Beams

4.1 Overview

This chapter considers the extent to which a clamped-clamped post-buckled beam bonded to two elongating piezoelectric actuators can be made to stably transition between remote equilibria. The elastica model is used with an extension to account for the influence of piezoelectric actuator on the structure. It expresses this piezoelectric coupling effect in terms of a non-dimensional parameter, σ, that can be easily calculated for candidate substrate/actuator configurations. The threshold values of σ required to execute stable transitions under different actuation and loading situations are presented, and stable transition paths are found to exhibit a strong dependence on external load, load location, actuation region and actuation voltage. The lowest threshold values of σ occur when the beam is actuated from approximately 15 to 85 percent of its span. Experiments validate the numerical results and offer the first physical demonstrations of the use of piezoelectric actuators to achieve stable transitions between remote equilibria.

Consider an inextensible post-buckled beam that is clamped on both ends, as shown in Fig 4.1. Piezoelectric patches are assumed to cover the entire beam. Two different voltages, V_1 and V_2, are applied to two separate, but identical, piezoelectric patches. The patch length is variable, with one end of each patch at mid-span. The patch span is specified with the parameters, sp_1 and sp_3, which denote the percent of span between $s = 0$ and the beginning and the end of the actuated region. The corresponding non-dimensional parameter σ_1 is proportional to the voltage (V_1) applied to the first piezoelectric patch, which is assumed to be actuated from sp_1 to 50% of span. Similarly, σ_2 corresponds to the second patch, which is activated from 50% to sp_3 of span.

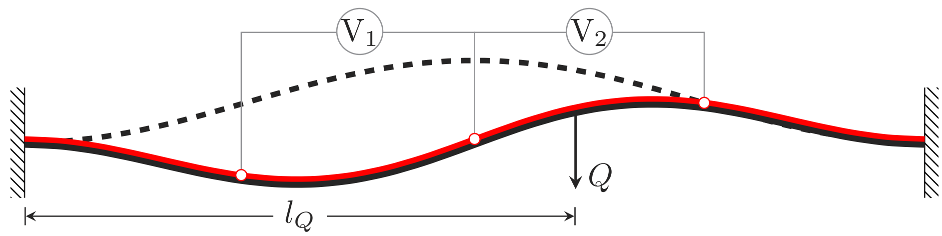

Figure 4.1. Schematic of a clamped-clamped post-buckled beam bonded with two piezoelectric patches on its top surface.

Parameter studies determining the threshold values of σ required to execute stable transitions under different actuation and loading situations are shown in the following sections. It is first helpful to evaluate the practical limits on the value of σ. (More details can be found in Chapter 3.) Fig. 4.2 shows the value of σ/l for some common substrates. Curves for steel (Y_s = 200 GPa), carbon fiber composite (Y_s = 100 GPa), aluminum (Y_s = 70 GPa), and acrylic (Y_s = 3 GPa) are shown versus the substrate thickness, h_s. This assumes the piezoelectric film is placed on the top side of the substrate and actuated with a positive voltage. Corresponding negative values of σ can be achieved by bonding the material to the bottom of the beam and actuating it with the same positive voltage. For this study, the values of σ are limited to a range of -2.5 to 2.5. This is a representative range for the case of a steel beam with $h_s \approx h_p$ and $l \approx 0.7$ m.

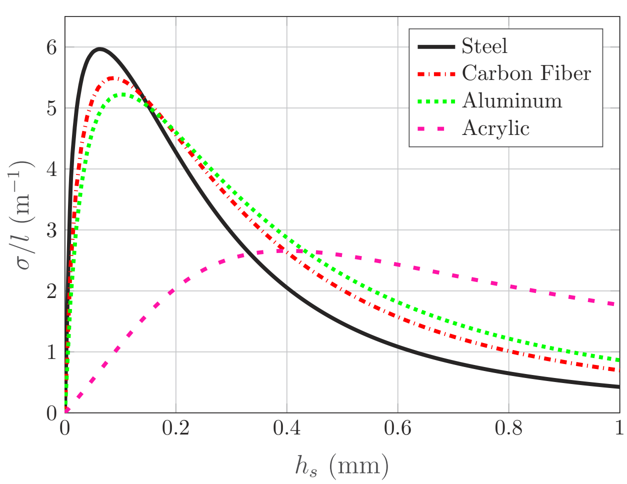

Figure 4.2. Value of σ/l versus the thickness of the substrate, h_s.

4.2 Load-Deflection-Angle Curves

Fig. 4.3 shows load-deflection-angle curves and corresponding dimensionless natural frequency squared for a mid-point load ($l_Q = 0.5$) and an end shortening of $e = 0.02$. Here, the mid-point deflection, δ, is normalized by δ_0 which is the mid-point deflection in the unloaded ($Q = 0$) and unactuated ($\sigma = 0$) case.

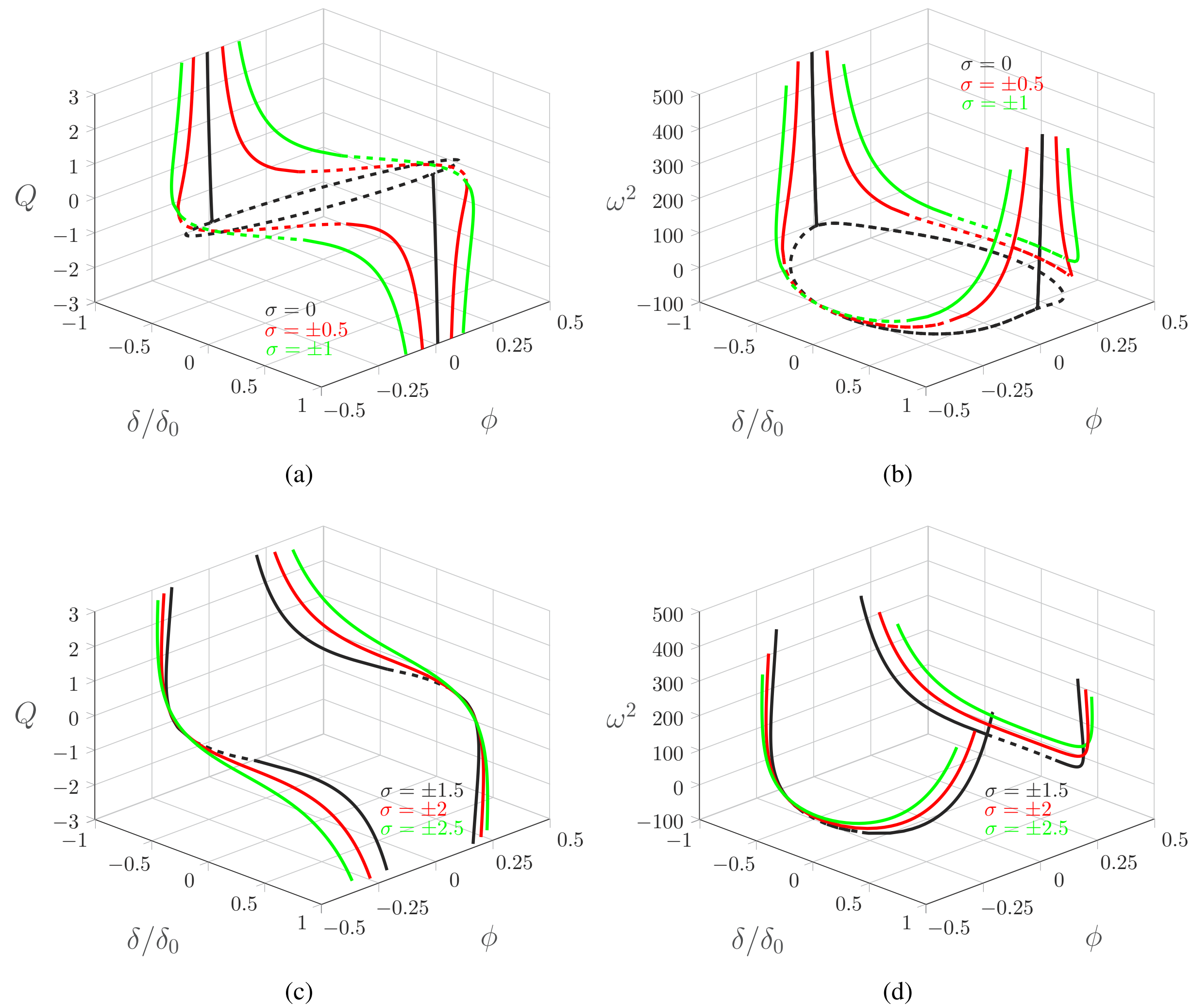

Figure 4.3. Non-dimensional load, Q, and non-dimensional natural frequency squared, ω^2, versus normalized mid-point deflection, δ/δ_0, and rotation angle at the beam mid-point, ϕ, for $e = 0.02$ and $l_Q = 0.5$. Actuation schemes are: (a) and (b) $\sigma = 0$, ± 0.5, and ± 1; (c) and (d) $\sigma = \pm 1.5$, ± 2, and ± 2.5. Stable (unstable) paths are indicated with solid (dashed) lines.

Energy stored in the composite is shown in Fig. 4.4. Here, $\bar{\varepsilon}_{33}^{S} = 7.68$ nF/m [128], and the piezoelectric film is assumed to be bonded to the entire top surface of the beam, but just 25% to 75% of the span is actuated.

The actuation region is divided into two identical patches, one from 25% to 50% of span and the other from 50% to 75% of span.

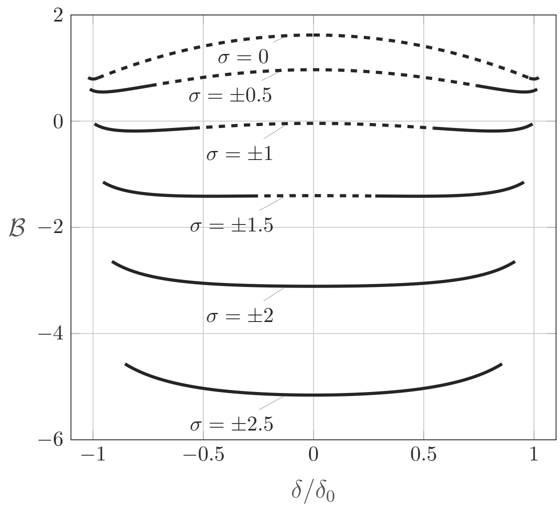

Figure 4.4. Non-dimensional energy stored in the composite, $\mathcal{B}$, versus normalized mid-point deflection, δ/δ_0 for $e = 0.02$ and $l_Q = 0.5$. Actuation schemes are: $\sigma = 0$, ± 0.5, ± 1, $\sigma = \pm 1.5$, ± 2, and ± 2.5. Stable (unstable) paths are indicated with solid (dashed) lines.

Actuation of the two patches is expressed in terms of σ_1 and σ_2. Six different actuation schemes are considered. In the first case (Fig. 4.3(a), black lines), the beam is not actuated, i.e., $\sigma_1 = \sigma_2 = 0$, and exhibits classical load-deflection-angle behavior with only unstable paths linking the remote stable equilibria. These unstable paths correspond to hilltops in the energy curves (Fig. 4.4). In the moderately actuated cases, the beam is actuated in a skew-symmetric manner with $\sigma_1 = -\sigma_2 = \pm 0.5$, ± 1, and ± 1.5. The load-deflection-angle curves indicate that actuation places the beam into an S-shaped configuration where the mid-point deflects considerably before the beam becomes unstable. The enhanced stability of these cases is indicated by energy curves with gradually shallower hilltops. In the most highly actuated cases, $\sigma_1 = -\sigma_2 = \pm 2$ and ± 2.5, and the paths linking the remote equilibria are entirely stable as indicated by energy curves ($\mathcal{B}$) that are entirely concave up, and natural frequency curves that are entirely positive.

4.3 Load-Actuation Maps

Surfaces representing possible equilibria and their associated stability are shown in Fig. 4.5 for a beam with $e = 0.02$. An external mid-point load and a skew-symmetric actuation strategy are assumed. Fig. 4.5(a)-

(c) show the normalized mid-point deflections versus Q and σ for actuation regions of 10% to 90%, 25% to 75%, and 30% to 70% of span, and an end shortening of $e = 0.02$. Stable and unstable equilibra are indicated with black and red dots, respectively.

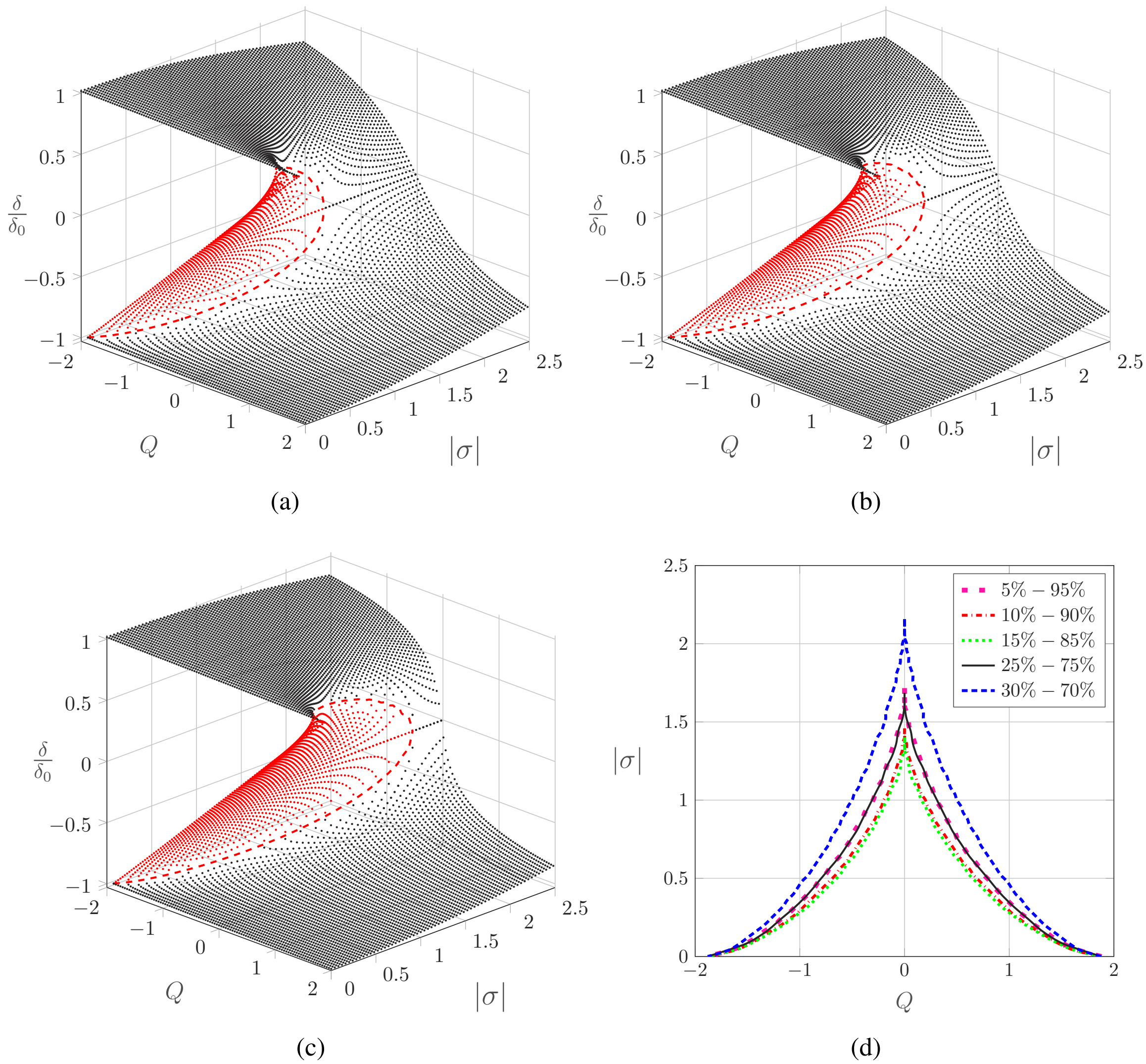

Figure 4.5. Normalized mid-point deflection, δ/δ_0, versus non-dimensional load, Q, and the absolute value of electromechanical coupling, $|\sigma|$, for $e = 0.02$. The piezoelectric material is actuated from: (a) 10% to 90% of span; (b) 25% to 75% of span; (c) 30% to 70% of span. (d) Boundaries between the stable and unstable equilibria for different actuation regions.

When $|\sigma|$ is greater than 1.48 for the 10% to 90% of span case, 1.68 for the 25% to 75% of span case, and 2.16 for the 30% to 70% of span case, only one stable equilibrium is present for a given load and voltage. Boundaries dividing stable and unstable equilibria are shown with red dashed curves. Fig. 4.5(d) is a projection of the stability boundary onto the Q-σ plane for several different assumed actuation regions.

The curves show a mild sensitivity to changes in actuation region and indicate that an actuation region from 15% to 85% of span enables stable transitions with a minimum required voltage.

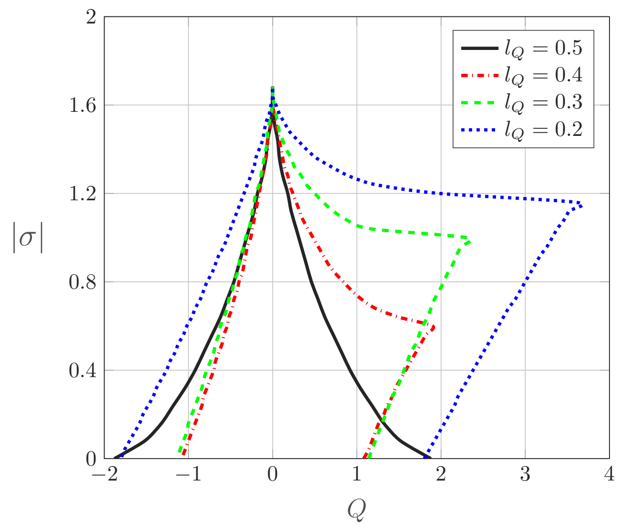

Figure 4.6. Boundaries between the stable and unstable equilibria in the Q-σ plane with an end shortening $e = 0.02$ with external point loads applied at different locations. The piezoelectric material is actuated from 25% to 75% of span.

Fig. 4.6 shows the boundaries between stable and unstable equilibria with external point loads applied at different locations. Here, $e = 0.02$ and the piezoelectric material is actuated from 25% to 75% of span. Fig. 4.6 indicates that non-mid-point loads lead to an asymmetric boundary, and the asymmetry becomes more distinct when the load location is closer to the clamped end. The boundaries corresponding to non-mid-point loads exhibit sharp corners at positive values of Q. The $|\sigma|$ values associated with these corners are $|\sigma| = 0.6$ for $l_Q = 0.4$, $|\sigma| = 1$ for $l_Q = 0.3$, and $|\sigma| = 1.16$ for $l_Q = 0.2$. Beyond the corner points, two stable and only one unstable equilibria can be obtained inside the boundary. Two stable and two unstable equilibria exist inside the boundary when $|\sigma|$ is lower than those breakpoints. Fig. 4.7 show examples of convergence between stable and unstable equilibria in both cases.

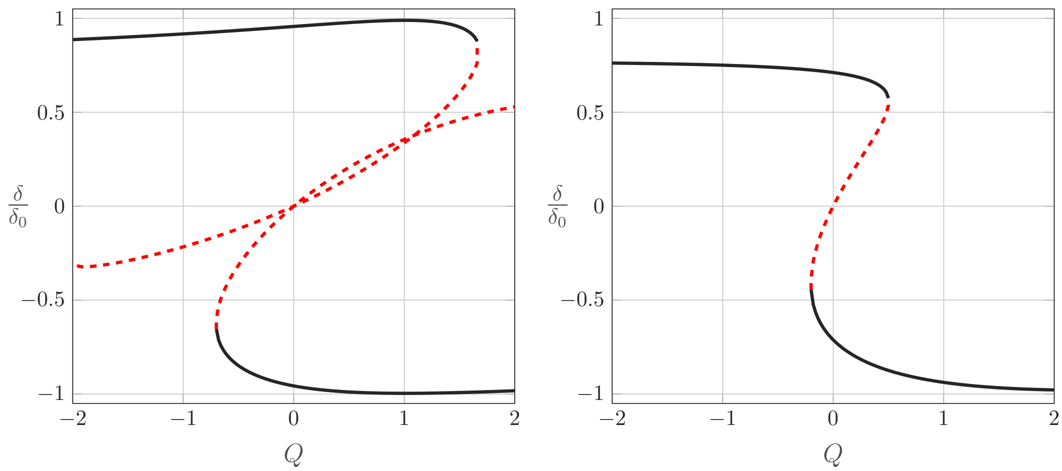

(a)

(b)

Figure 4.7. Normalized mid-point deflection, δ/δ_0, versus non-dimensional load, Q, for $e = 0.02$ and $l_Q = 0.3$. Actuation schemes are: (a) $|\sigma| = 0.5$, and (b) $|\sigma| = 1.2$. Stable (unstable) paths are indicated with solid (dashed) lines.

4.4 Effects of Actuation Voltage and Actuation Region

Fig. 4.8(a)-(c) show normalized mid-point deflections versus σ_1 and σ_2 for actuation regions of 10% to 90% of span, 25% to 75% of span, and 30% to 70% of span, and an end shortening of $e = 0.02$. Stable and unstable equilibria are indicated with black and red dots, respectively. Blue dots indicate that the corresponding equilibrium is unique and stable. Stable and unstable equilibria coexist for $|\sigma_{1,2}| \leqslant \sigma_{cr}$. When $|\sigma_1|$ or $|\sigma_2|$ is greater than the threshold σ_{cr}, a single stable equilibrium is present. A red dashed curve indicates the boundary between the stable and unstable equilibria. The threshold σ_{cr} for different actuation regions can be found in Fig. 4.8(d).

Fig. 4.8(d) plots the stability boundary for various actuation regions. The cusps of these boundaries represent the minimum value of σ required to fully execute a stable transition. This value is denoted σ_{cr}. It is clear from Fig. 4.8 that stable transitions can be achieved so long as σ_1 can be made greater than σ_{cr} and σ_2 can be made less than $-\sigma_{cr}$. To transition stably to a remote equilibrium, the actuation path must cross $\delta = 0$ while exceeding σ_{cr}. This threshold value can serve as a guide to designing physically realizable substrate/actuator combinations capable of executing stable transitions. Fig. 4.8(d) shows that

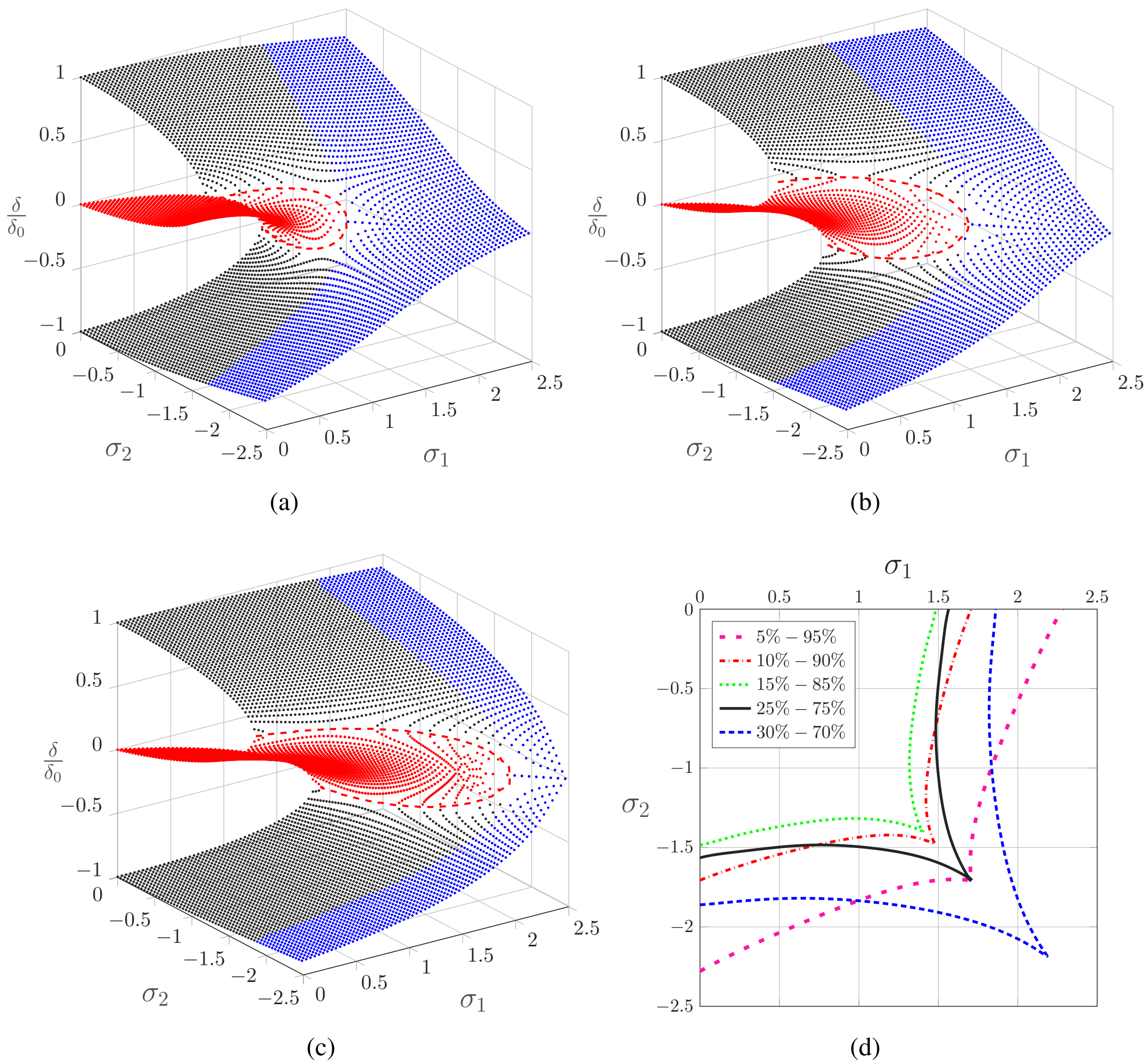

Figure 4.8. Normalized mid-point deflection, δ/δ_0, versus non-dimensional electromechanical coupling terms, σ_1 and σ_2 for $e = 0.02$ and $Q = 0$. The piezoelectric material is actuated from: (a) 10% to 90%, (b) 25% to 75%, and (c) 30% to 70% of span. (d) Boundaries between the stable and unstable equilibria for different actuation regions.

σ_{cr} behaves non-monotonically as the actuation region decreases in length. This is more clearly illustrated with the $e = 0.02$ curve in Fig. 4.9 where the values of σ_{cr} corresponding to actuation regions in Fig. 4.8(d) are marked with red dots. The stable transition requiring the least actuation voltage has an actuated region from 15% to 85% of span. Fig. 4.9 also illustrates that σ_{cr} behaves similarly for different values of the end shortening and increases monotonically with increases in end shortening.

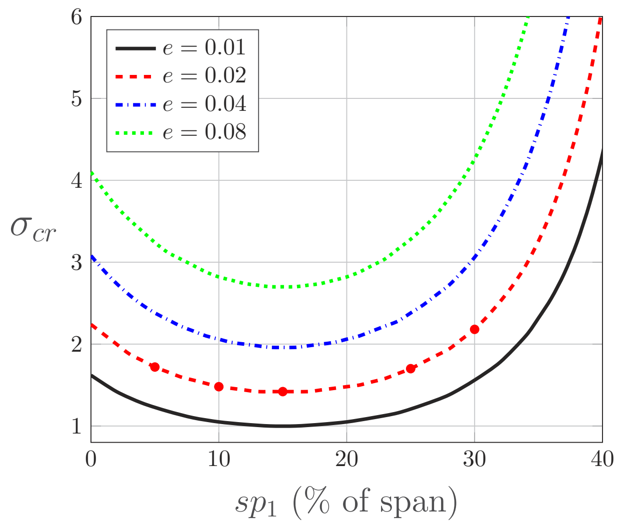

Figure 4.9. Minimum required value of non-dimensional electromechanical coupling term, σ_{cr}, versus the beginning location of the actuation region, sp_1, for different values of end shortening. The piezoelectric material is actuated with a value of σ from sp_1 to 50% of span and with a value of $-\sigma$ from 50% to $(100\% - sp_1)$ of span.

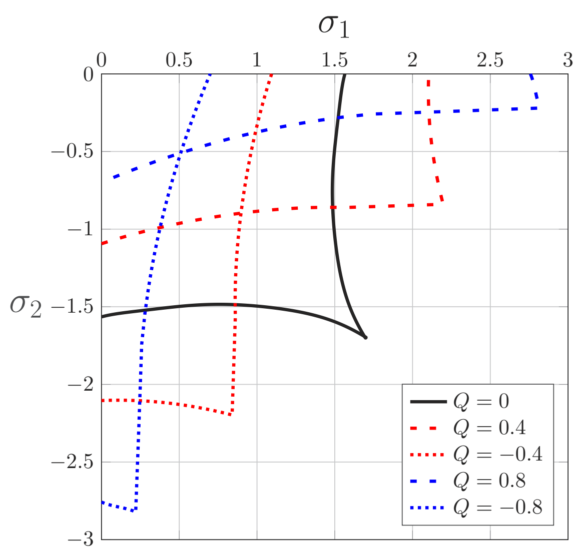

Figure 4.10. Boundaries between the stable and unstable equilibria for an end shortening $e = 0.02$ under different loads located at the mid-point ($l_Q = 0.5$). The piezoelectric material is actuated from 25% to 75% of span.

Fig. 4.10 shows the actuation boundary between the stable and unstable equilibria for $e = 0.02$ and mid-point loads of different magnitudes. The piezoelectric material is actuated from 25% to 75% of span.

Fig. 4.10 indicates that external loads cause an asymmetry in the stability boundary, with the asymmetry becoming more pronounced as the magnitude of the external load increases. Since values of σ exceeding three are difficult to achieve with realistic piezoelectric/substrate configurations, the results indicate that $Q \approx 0.8$ is the practical limit on external load when executing stable transitions between remote equilibria for $e = 0.02$.

4.5 Experimental Validation

4.5.1 Experimental Setup

To validate the numerical results and physically demonstrate stable transitions between remote equilibria, an experimental setup is designed, as shown in Fig. 4.11. The test article is a 50 cm $\times$ 2 cm $\times$ 0.25 mm strip of spring steel ($\rho_s = 7700$ kg/m^3, $Y_s = 200$ GPa). The setup includes two fixtures capable of clamping both ends of the beam with a desired end shortening. Piezoelectric material is bonded to the middle portion of the beam's span using two patches of P1-type MFC ($\rho_p = 5440$ kg/m^3, $Y_p = 30.34$ GPa, $d_{33} = 460$ pm/V, and $l_p = 0.45$ mm [123]). Each patch has an active dimension of 8.5 cm by 1.4 cm by 0.3 mm. One patch is bonded to the front of the beam with epoxy, and the other is bonded to the back. The two MFC patches are powered from -500 to 1500 volts by a high voltage amplifier (Smart Materials AMT2012-CE3). A high-resolution camera (JVC GC-PX100) obtains photographs of the beam at every actuated case, and a custom image processing procedure identifies the edge of the beam and digitizes its position.

Since the MFC partially covers the beam, an effective flexural rigidity and an effective mass ratio are used for non-dimensionalizing the natural frequencies. The effective flexural rigidity and mass per unit are calculated using

$$YI_{eff} = a_1 YI + a_2 YI_s, \quad \mu_{eff} = a_1 \mu + a_2 \mu_s, \tag{4.1}$$

where a_1 is the fraction of the beam bonded with MFC, and a_2 is the fraction without. The flexural rigidity of the substrate is given by $YI_s = Y_s b h_s^3/12$, and the mass ratio of the substrate is defined as $\mu_s = \rho_s b h_s$. The dimensional natural frequency is calculated by $f^* = \pi f / (l^2 \sqrt{\mu_{eff}/YI_{eff}})$. Parameters corresponding to unactuated test articles are shown in Table 4.1 along with a comparison between the experimental natural frequencies and the predicted values.

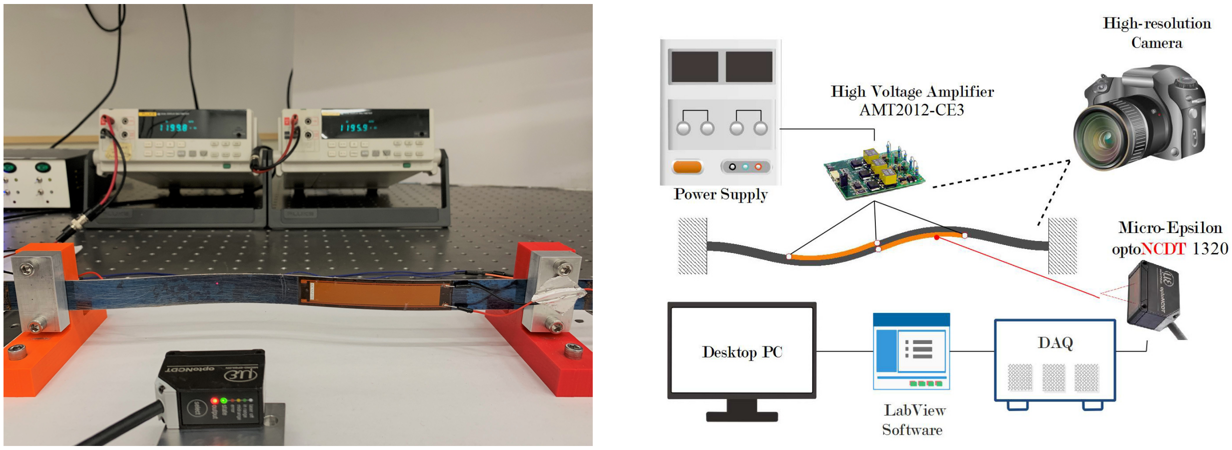

(a) (b)

Figure 4.11. (a) Photo, and (b) schematic of the experimental setup with two MFC patches placed each side of the beam, covering roughly the middle 50% of span.

Table 4.1. Parameters, natural frequencies, and damping ratios for the unactuated test articles.

	25%-75% of span	20%-80% of span
Length l (cm)	38.60	30.80
Patch covering span a_1	0.50	0.60
Effective flexural rigidity (Nm^{-2})	0.0117	0.0130
Effective mass ratio (kg/m)	0.0548	0.0581
Theory f^* (Hz)	21.72	34.93
Experiment f^* (Hz)	21.96	37.84
Experiment ζ	0.0125	0.0278

Fig. 4.12(a) is a representative displacement time history of the beam. The beam is undergoing free vibration while actuated with 1260 volts in one patch and 600 volts in the other. A small rubber tipped hammer is used to excite the beam, and the time history is measured by a laser optical displacement measurement sensor (Micro-Epsilon optoNCDT 1320). Fig. 4.12(b) shows the amplitude spectrum of the displacement time history for a point located near 60% of span. The first two resonance peaks are clearly visible and correspond to the first two damped natural frequencies. The resonant peaks in the amplitude spectra are used to calculate damping via the half-power point method. The natural frequency is obtained from $f = \bar{f}/\sqrt{1-\zeta^2}$, where $\bar{f}$ is the damped frequency, and ζ is the viscous damping ratio [129].

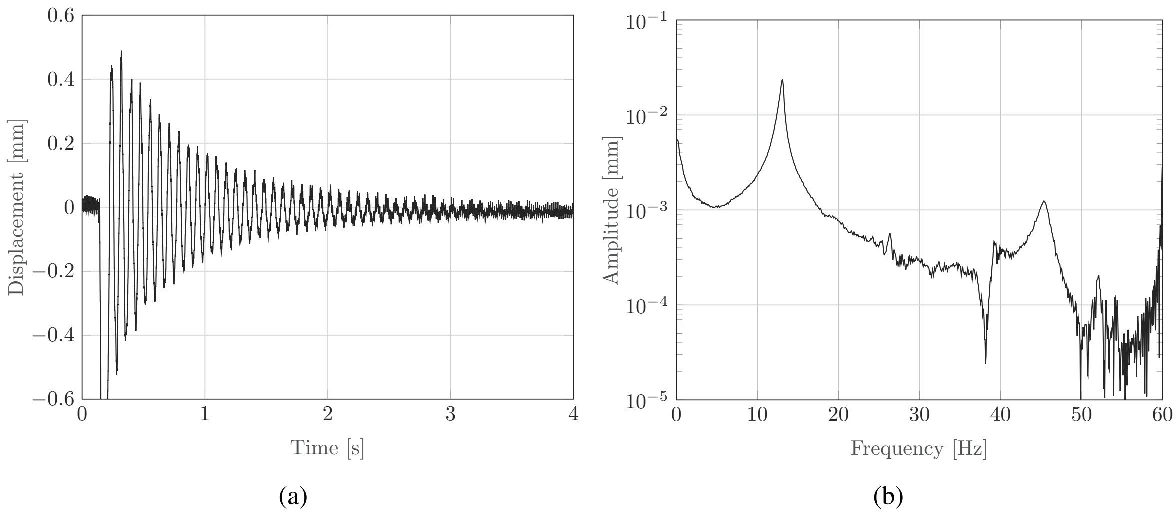

Figure 4.12. Example experimental data: (a) displacement time history, and (b) amplitude spectrum.

Separate voltages are applied to the two MFC patches. Since the patches are on opposite sides of the beam, a positive voltage is applied to each patch to create the asymmetric actuation pattern. Two different stable transition paths are implemented to verify predicted changes to the natural frequencies and mid-point deflections. In the first case, voltages V_1 and V_2 are changed simultaneously and always have the same magnitude. In the second case, V_1 and V_2 are controlled separately to obtain a loop transition path. In both cases, voltages are changed in 60 volt increments.

An image correlation procedure is used to digitize the beam's shape and extract mid-point deflections. Key steps of the image correlation process are shown in Fig. 4.13 for the case of an unloaded beam with 1260 volts applied. More details of the image correlation process can be found in Chapter 3.

4.5.2 Numerical and Experimental Data Comparison

Fig. 4.14 show normalized mid-point deflection versus σ for two stable transition paths. For each stable path, data are shown from three experimental trials. The beam's mid-point is identified by numerically integrating the beam's shape as obtained by the image correlation procedure. Across all experimental trials, mid-point deflections correlate well, especially in the case of $\sigma_1 \neq \sigma_2$ (loop path). In the case of $\sigma_1 = -\sigma_2$

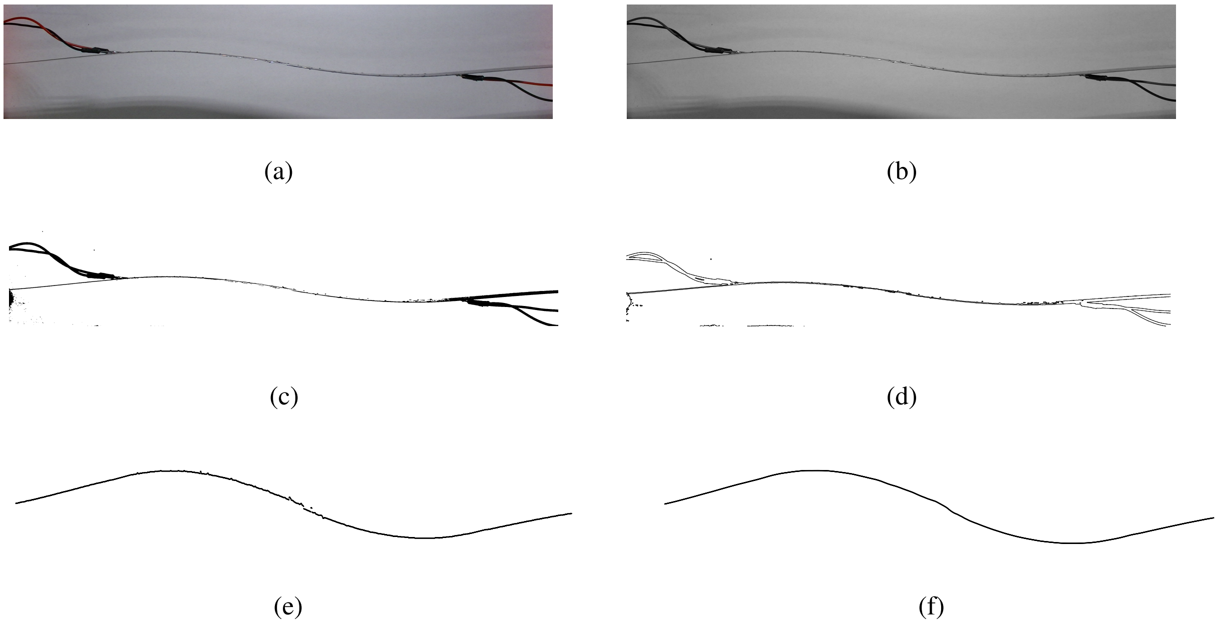

Figure 4.13. Image correlation process of an unloaded beam with $e = 0.02$ and ± 1260 volts applied. The true-color photos are converted to gray-scale images and then to black and white binary images. Contour profiles on the binary images are extracted by Canny algorithm, and points on the edge of the beams are saved and smoothed by a 50 point moving average.

(symmetry path), the match between experiment and theory is not quite as good, due to initial imperfections breaking the skew-symmetry presumed by the model.

Natural frequency maps corresponding to the actuation-deflection curves are shown in Fig. 4.15. Red dots in Fig. 4.15(a) show the transition from the primary post-buckled shape to the asymmetric shape ('S' shape), while black triangles indicate the transition from the 'S' shape to the remote post-buckled shape. When the mid-point deflection of the beam approaches zero (around $|\sigma| = 1.7$), the natural frequency stops decreasing and begins increasing slowly with increasing $|\sigma|$ values. The mid-point remains at zero as $|\sigma|$ increases. Experimental trials validate this behavior.

Experiments are also conducted for the case of actuation region of 20% to 80% of span. Voltage-deflection curves and corresponding non-dimensional natural frequency curves for 20% to 80% of span actuated are shown in Fig. 4.16 and Fig. 4.17. This group of experiments are used to validate the influence

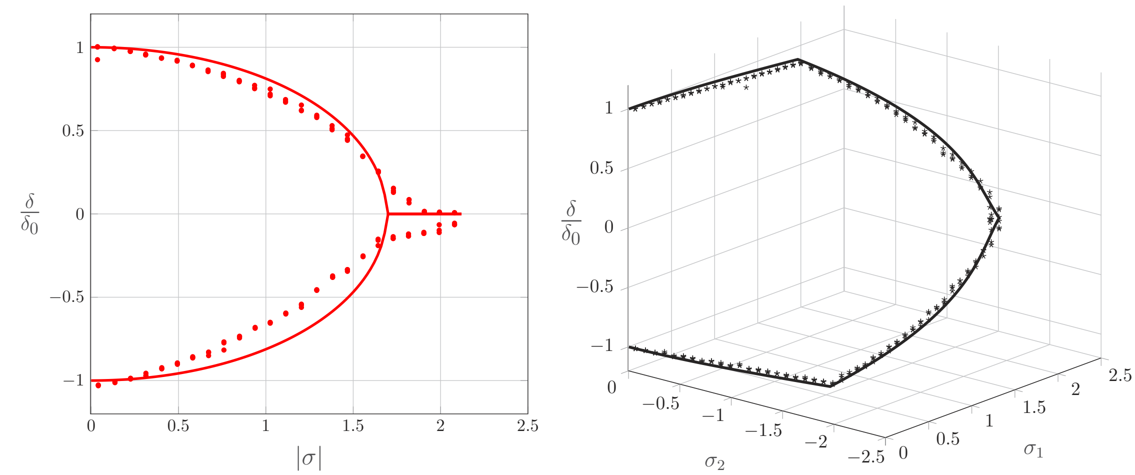

(a) (b)

Figure 4.14. Normalized mid-point deflection, δ/δ_0, versus non-dimensional electromechanical coupling parameters, σ_1 and σ_2, for $e = 0.02$ with three trials of experimental data (markers). (a) Symmetry path where $\sigma_1 = -\sigma_2$, and (b) loop path where $\sigma_1 \neq \sigma_2$. The piezoelectric material is actuated from 25% to 75% of span.

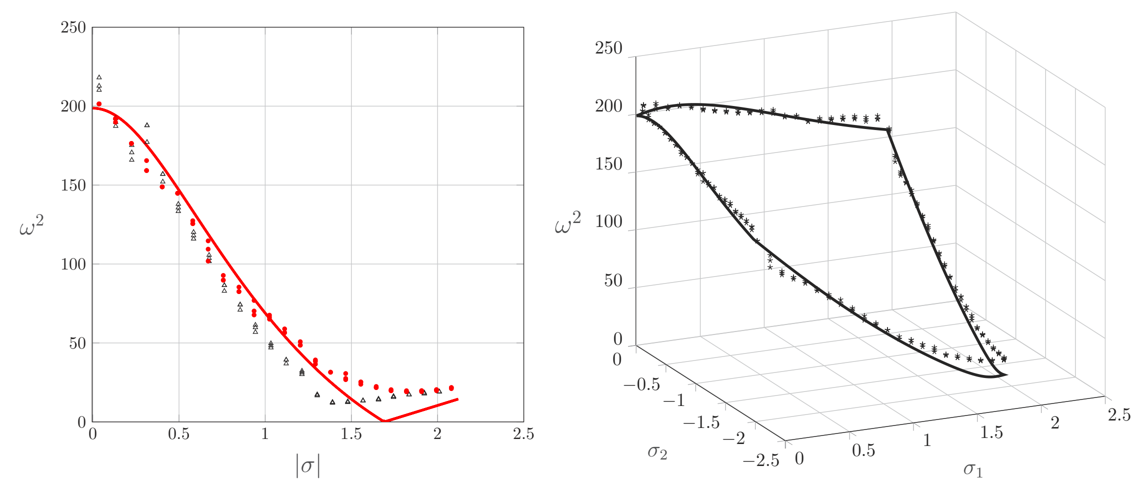

(a) (b)

Figure 4.15. Non-dimensional natural frequency squared, ω^2, versus non-dimensional electromechanical coupling parameters, σ_1 and σ_2, for $e = 0.02$. with three trials of experimental data (markers). Natural frequencies for (a) the symmetry path, and (b) the loop path. The piezoelectric material is actuated from 25% to 75% of span.

of different actuation regions. The actuation-deflection natural frequency results change only slightly with the relatively minor change in actuation regions.

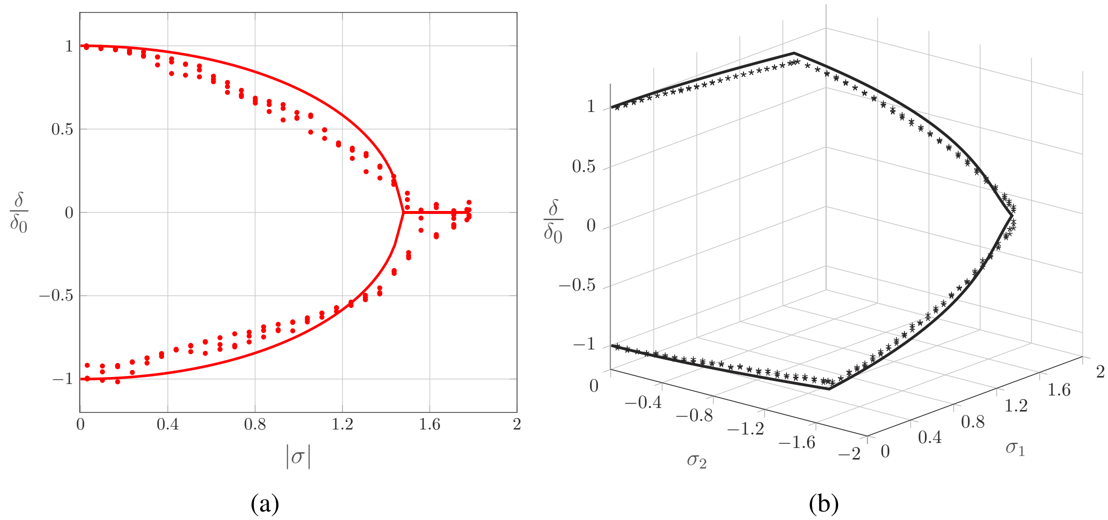

Figure 4.16. Normalized mid-point deflection, δ/δ_0, versus non-dimensional electromechanical coupling parameters, σ_1 and σ_2, for $e = 0.02$ with three trials of experimental data (markers). (a) Symmetry path where $\sigma_1 = -\sigma_2$, and (b) loop path where $\sigma_1 \neq \sigma_2$. The piezoelectric material is actuated from 20% to 80% of span.

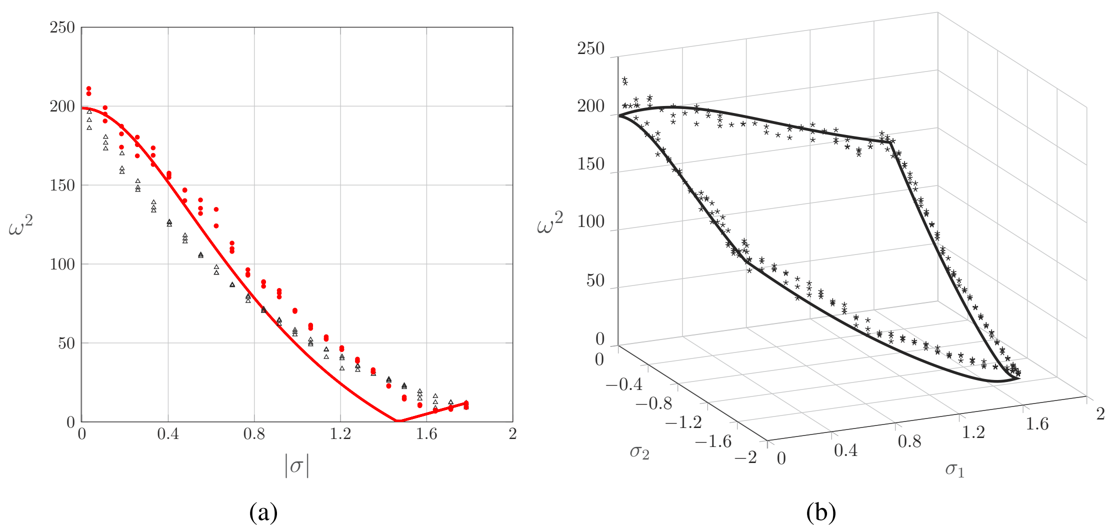

Figure 4.17. Non-dimensional natural frequency squared, ω^2, versus non-dimensional electromechanical coupling parameters, σ_1 and σ_2, for $e = 0.02$. with three trials of experimental data (markers). Natural frequencies for (a) the symmetry path, and (b) the loop path. The piezoelectric material is actuated from 20% to 80% of span.

4.6 Conclusions

Numerical and experimental results demonstrate that by using asymmetric actuation of two elongating piezoelectric patches, a clamped-clamped beam can be made to transition between remote equilibria without instability. The threshold for achieving stable transitions is given by a non-dimensional electromechanical coupling value of σ_{cr}. The critical threshold increases monotonically as the end shortening increases. However, σ_{cr} behaves non-monotonically with respect to the span of the actuation region. The minimum σ_{cr} occurs when the actuation region is approximately 15%-85% of span. Under mid-point loading and $e = 0.02$, results indicate that stable transitions can be practically achieved for non-dimensional forces up to $Q \approx 0.8$. Experiments involving different values of actuation voltages are conducted to verify the numerical results and give physical demonstrations of the stable transitions.

This study can be used to help design a class of smart structures that circumvent structural instability in the face of complicated loading environments. For example, piezoelectric actuators could be embedded into advanced composite materials avoid snap-through instability as needed. This work also includes new approaches for modeling the electromechanical actuation of highly deformed structures. It is expected that these modeling contributions can inform the design of smart devices that intentionally induce snap-through for the purposes of actuation, energy harvesting, or structural morphing.

Chapter 5

Modal Behavior During Stable Transitions of Post-buckled Beams

5.1 Overview

This chapter also considers a clamped-clamped post-buckled beam bonded to two elongating piezoelectric actuators to transition stably between remote equilibria. To address the dynamic analysis of post-buckled structures during stable transitions, this chapter theoretically and experimentally investigates the changes of first four natural frequencies and their corresponding mode shapes during the transition. Experiments are conducted to validate the numerically derived natural frequencies and mode shapes.

An inextensible beam is assumed to be post-buckled and clamped on both ends shortened by an amount of e. Piezoelectric material covers one side of the beam, as shown in Fig. 4.1. Two different voltages, V_1 and V_2, are applied to two piezoelectric patches on the left and right side of the beam with one end of each patch at mid-span. The patch span is specified with the parameters, sp_1 and sp_3. Two non-dimensional electromechanical coupling terms, σ_1 and σ_2, specify the actuation level of the two piezoelectric patches.

As shown in Chapter 4, controlling the σ values can promote stable transitions between remote equilibria. Each stable equilibrium shape has its own natural frequencies, with each having a corresponding mode shape. Mode shapes are identified from the lateral dynamic deflection, y_d, in Eqs. (2.21). The amplitude of a mode shape is arbitrary, and the mode shapes shown here are normalized by the maximum of the absolute value of the lateral dynamic deflection, $|y_d|_m$. This chapter is an extension of Chapter 4 focusing on the structural dynamic behavior during stable transitions. Two types of transitions are considered—one in which the transition is accomplished by changing the external load, and one in which the actuation levels are changed. For the latter type of transition, two actuation schemes are considered. The first actuation scheme is called the "symmetry path" and involves simultaneously changing the voltages in two piezoelectric patches such that the two voltages have the same magnitude. In the second scheme, called the "loop path", the voltages are changed to obtain desired values of σ_1 and σ_2 and in general do not have the same magnitude.

5.2 Stable Transitions by Changing External Load

A map of the mid-point deflections versus non-dimensional mid-point load, Q, for $e = 0.02$ and $|\sigma| = 2$ are shown in Fig. 5.1(a). The mid-point deflections are normalized by the midpoint deflection of the unloaded and unactuated post-buckled beam, δ_0. The piezoelectric material is assumed to be actuated from 25% to 75% of the span—a positive σ value is assumed from 25% to 50% of span and a negative σ is assumed on the other half of the active region. Provided $|\sigma|$ is sufficiently high, stable transitions can be achieved through a change in lateral load. At large negative values of load, the load acts to pull the beam up toward its unactuated and unloaded post-buckled shape (i.e., $\delta/\delta_0 = 1$). As the magnitude of the negative load is reduced, the actuated beam takes on more of an anti-symmetric 'S' shape with mid-point deflections near zero. As the lateral load becomes positive, the beam transitions stably toward it's remote post-buckled shape with $\delta/\delta_0 \approx -1$. The natural frequency map in Fig. 5.1(b) confirms the stable transition by showing that the square of the first natural frequency remains positive throughout the change in loading. The first and third natural frequencies increase monotonically as the magnitude of the load increases, while the the second and fourth natural frequencies have a peak at $Q = 0$. The peak in the fourth natural frequency at $Q = 0$ is particularly pronounced and represents an approximately 9% jump in natural frequency as Q approaches zero from either direction.

Fig. 5.2 shows different equilibrium shapes of the beam with the first and second mode shapes superimposed. Static equilibria and mode shapes are indicated with gray solid lines and black dashed lines, respectively. The values of Q considered in Fig. 5.2 are indicated with black squares in Fig. 5.1(a). The equilibria in Fig. 5.2 show the transition from the primary post-buckled equilibrium to the anti-symmetric

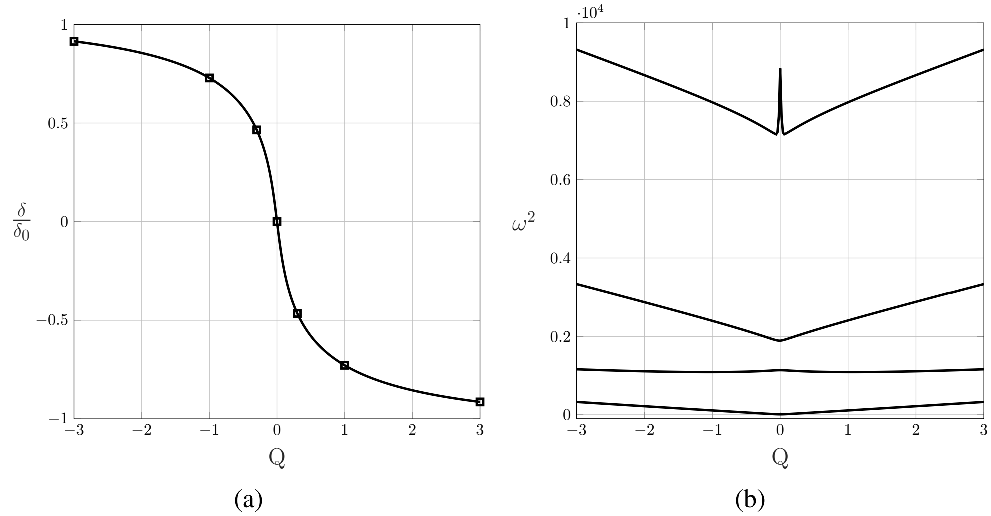

Figure 5.1. (a) Normalized mid-point deflection, δ/δ_0, and (b) first the four non-dimensional natural frequencies squared, ω^2, versus dimensionless mid-point load, Q, for $e = 0.02$ and $|\sigma| = 2.0$.

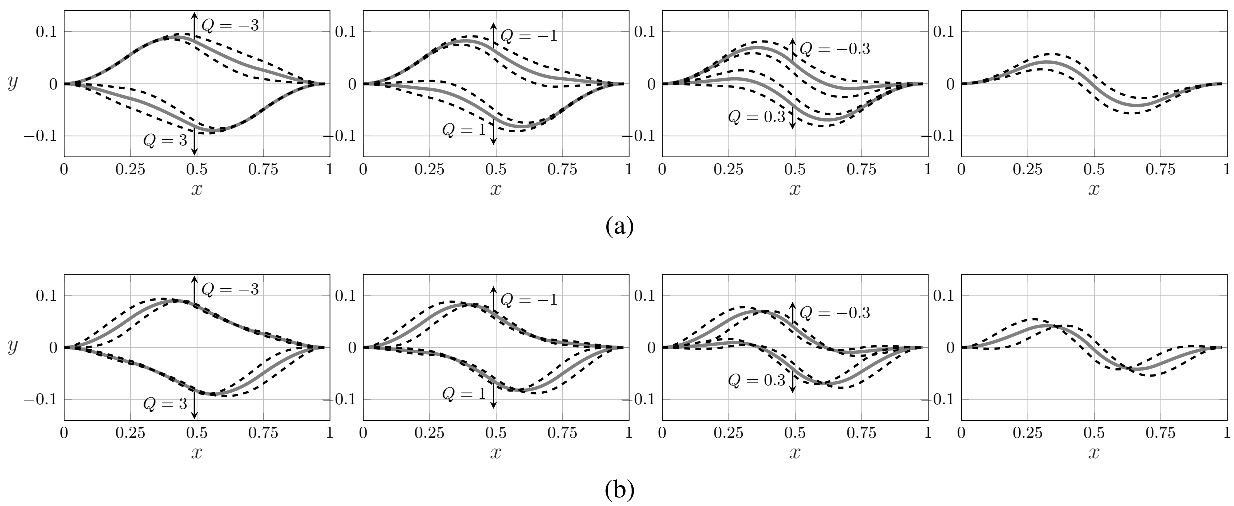

Figure 5.2. Equilibrium shapes of the beam for select values of Q for $|\sigma| = 2.0$ and $l_Q = 0.5$ and with the (a) first and (b) second mode shapes superimposed. A stable transition is achieved from the primary equilibrium to the remote equilibrium by changing Q.

(S-shaped) equilibrium at $Q = 0$, and then the transition to the remote post-buckled equilibrium. When Q is relatively large, the beam takes a shape resembling its post-buckled shape, but with the maximum deflection shifted to the left or right of $x = 0.49$. (Note that for the considered end shortening of $e = 0.02$, $x = 0.49$ corresponds to the mid-point of the unloaded and unactuated beam.) According to Fig. 5.2(a), the first mode shape is characterized by relatively little motion on the side of the beam at which the maximum static deflection occurs. The opposite trend it true in the case of the second mode. When the beam is in the ‘S’-shaped configuration, the first and second mode shapes are much more symmetric about the mid-point. It is also observed that the number of vibrational nodes is non-sequential, with the first mode having no nodes and the second mode having two.

5.3 Stable Transition by Changing Actuation Voltage

This section considers stable transitions that are executed by changing the actuation voltage applied to each piezoelectric patch. The piezoelectric material is again assumed to be active from 25% to 75% of the span. The actuation region is divided into two identical patches, one from 25% to 50% of span and the other from 50% to 75% of span. Two transition paths are considered for the unloaded ($Q = 0$) case: the symmetric path where $|\sigma|$ is a constant and a loop path where $\sigma_1 \neq -\sigma_2$.

5.3.1 Symmetric Path

Fig. 5.3 shows maps of normalized mid-point deflection and natural frequency versus $|\sigma|$ with $e = 0.02$. The symmetry path is executed by increasing $|\sigma|$ past a critical value (about 1.7 in this case) and then subsequently decreasing it while keeping $\sigma_1 = -\sigma_2$. The map of mid-point deflections indicates that upon increasing $|\sigma|$, the beam transitions from its primary post-buckled equilibrium to an anti-symmetric ‘S’ shape when $|\sigma|$ equals the critical value. Increases to $|\sigma|$ beyond this critical value do not appreciably change the shape of the anti-symmetric equilibrium, but do serve to stabilize the shape somewhat. This is evidenced in Fig. 5.3(b) where the first natural frequency increases as $|\sigma|$ is increased beyond 1.7. With respect to the higher-order natural frequencies, increasing σ results in a monotonic increase in the second natural frequency while the changes to the third and fourth natural frequencies are more complex. The third natural frequency experiences rapid reduction as $|\sigma|$ increases to 1.7. It then decreases very slowly. This decrease is followed by a slow increase near $|\sigma| = 3.5$. The second and third natural frequencies converge at $|\sigma| \approx 4.5$. The square of the fourth natural frequency exhibits a complicated trend in which it has a local maxima near $|\sigma| = 1$ followed by a roughly linear increase when $|\sigma| > 1.7$.

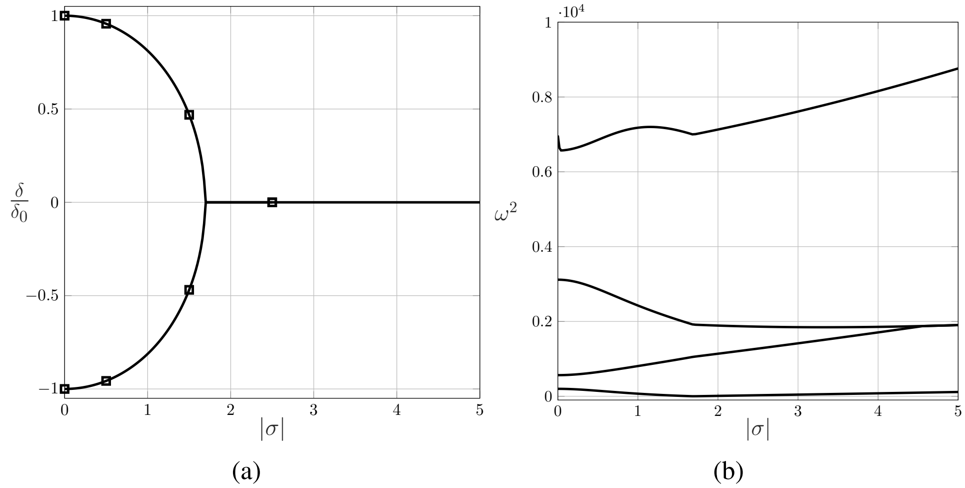

Figure 5.3. (a) Normalized mid-point deflection, δ/δ_0, (b) first four non-dimensional natural frequencies squared, ω^2, versus $|\sigma|$.

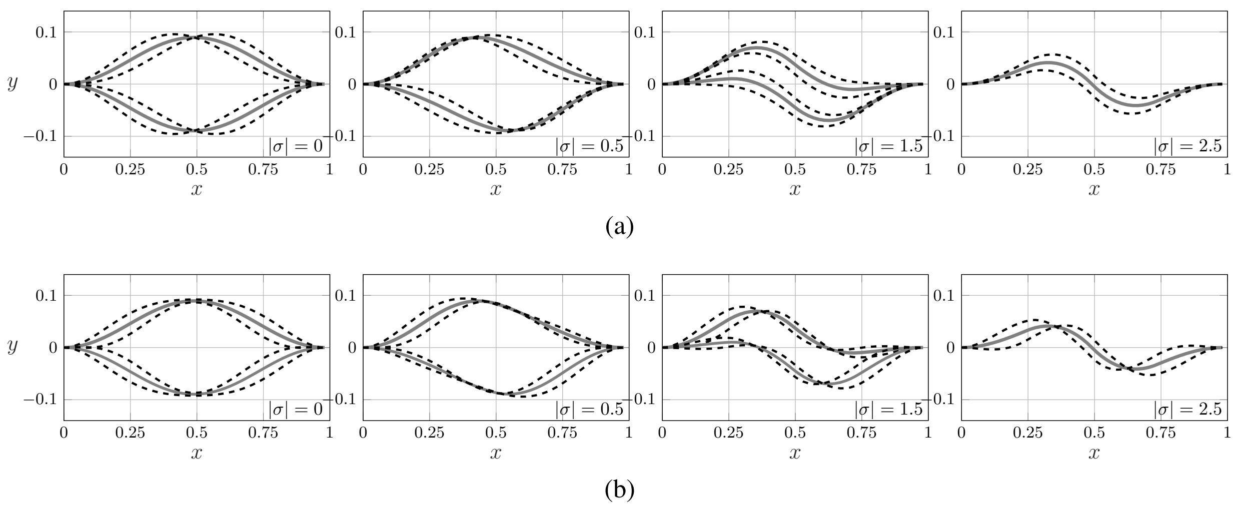

Figure 5.4. Equilibrium shapes of the beam with (a) first and (b) second mode shapes superimposed. Transition is achieved by changing $|\sigma|$.

Fig. 5.4 plots select equilibrium shapes of the beam undergoing a symmetry path transition. The first and second mode shapes are superimposed with dashed lines onto the solid lines indicating the static equilibrium shape. The values of $|\sigma|$ considered in Fig. 5.4 are denoted by black squares in Fig. 5.3(a). The nature of the mode shapes is similar to those observed when the stable transition was executed by changing external load. Namely, when the actuation causes the maximum of the beam's deflected shape to shift to one side of $x = 0.49$, the first mode shape becomes highly localized to the other side of the beam. The opposite effect is observed in the second mode. Another similarity is that when the beam is in the ‘S’-shaped configuration, the first and second mode shapes are again symmetric about the mid-point, with the first mode having no nodes and the second mode having two. Note that without actuation ($|\sigma| = 0$) or external load, only subtle differences can be observed between the first two mode shapes. However, animations of these mode shapes reveal that the first mode oscillates with primarily side-to-side motion while the second mode oscillates primarily in the lateral direction.

5.3.2 Loop Path

Fig. 5.5 maps the normalized mid-point deflection and the first two natural frequencies squared for a post-buckled beam executing a stable transition via a loop path. In this case, the actuation parameter associated with the two piezoelectric patches are given by σ_1 and σ_2, respectively. The loop path involves increasing σ_1 to a maximum value and then decreasing σ_2 to a minimum value. Next, σ_1 is decreased to zero followed by decreasing σ_2 to zero. In general, the first two natural frequencies separate as actuation levels are increased, with the first natural frequency decreasing while the second increases.

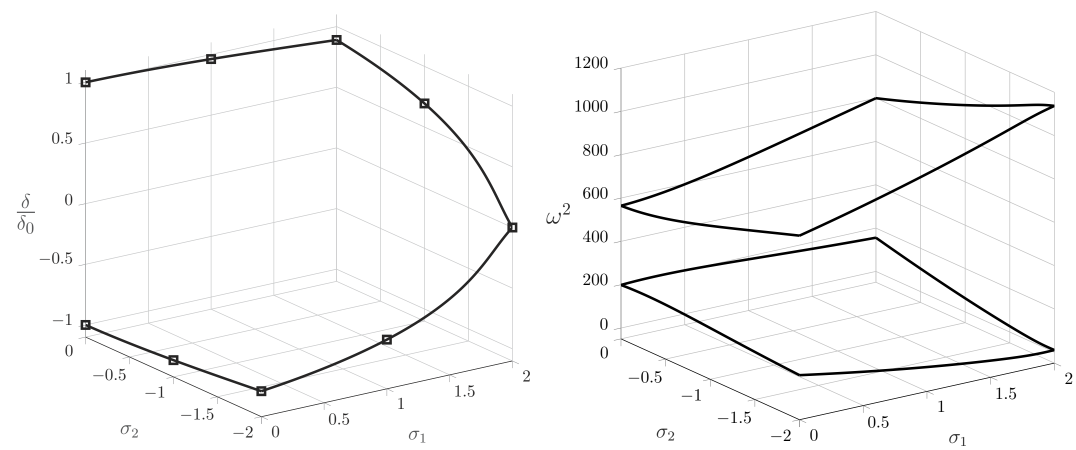

(a) (b)

Figure 5.5. (a) Normalized mid-point deflection, δ/δ_0, and (b) first two non-dimensional natural frequencies squared, ω^2, versus σ_1 and σ_2, for a loop path.

Fig. 5.6 shows select equilibrium shapes (corresponding to the markers in Fig. 5.5(a)) with mode shapes superimposed. It demonstrates the transition from the primary equilibrium to the anti-symmetric equilibrium (increasing σ_1 to 2 and decreasing σ_2 to -2), and the transition from the anti-symmetric equilibrium to the

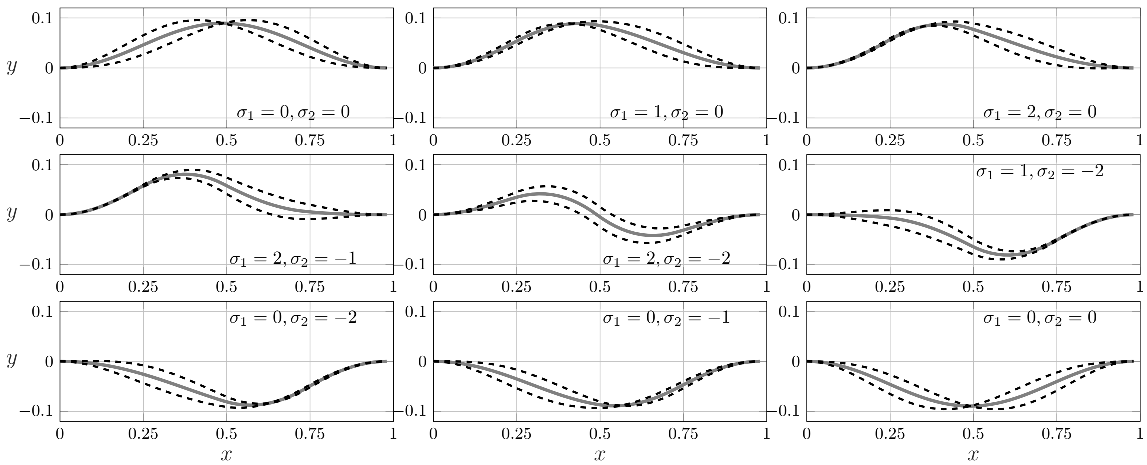

(a)

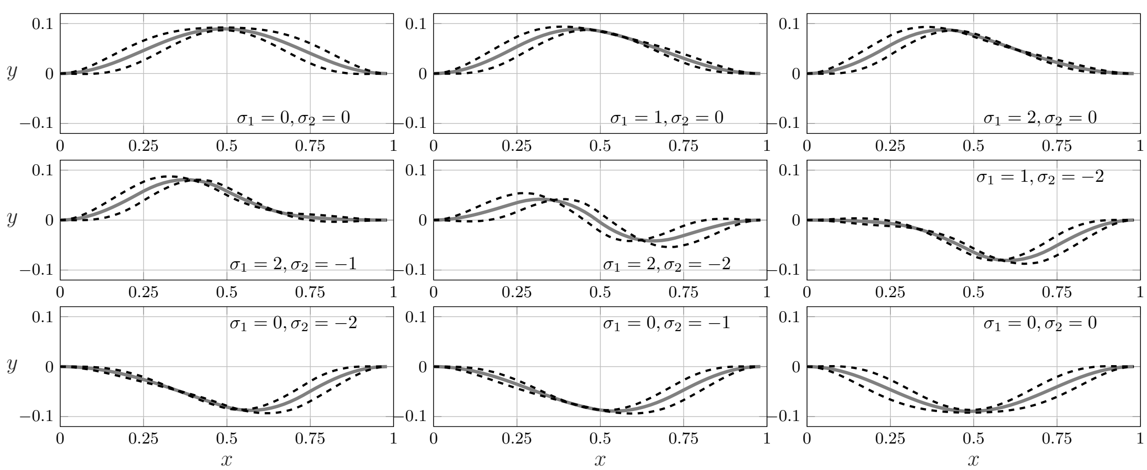

(b)

Figure 5.6. Equilibrium shapes of the beam with (a) first and (b) second mode shapes superimposed. Transition is achieved by changing σ_1 and σ_2 separately.

remote symmetric equilibrium (decreasing σ_1 and increasing σ_2 back to zero). Static equilibria and dynamic deformations are again indicated with solid lines and dashed lines, respectively. The variations of the mode shapes during the loop path transition are similar to those observed in the symmetry path. The mode shapes again exhibit localization when the maximum deflected shape of the beam is shifted away from $x = 0.49$.

5.4 Effects of Actuation Region

The effects of changing the length of the actuation region are considered here for symmetry path transitions of the unloaded beam. The beam is actuated from sp_1 percent of span to sp_3 percent of span such that $sp_1 + sp_3 = 100\%$. This creates an active region that is centered about the beam's mid-point. A voltage V_1 is applied from sp_1 percent of span to 50% of span and the opposite voltage ($V_2 = -V_1$) is applied to the other half of the active region. The first four natural frequencies squared are shown for various actuation regions in Fig. 5.7 for select values of $|\sigma|$.

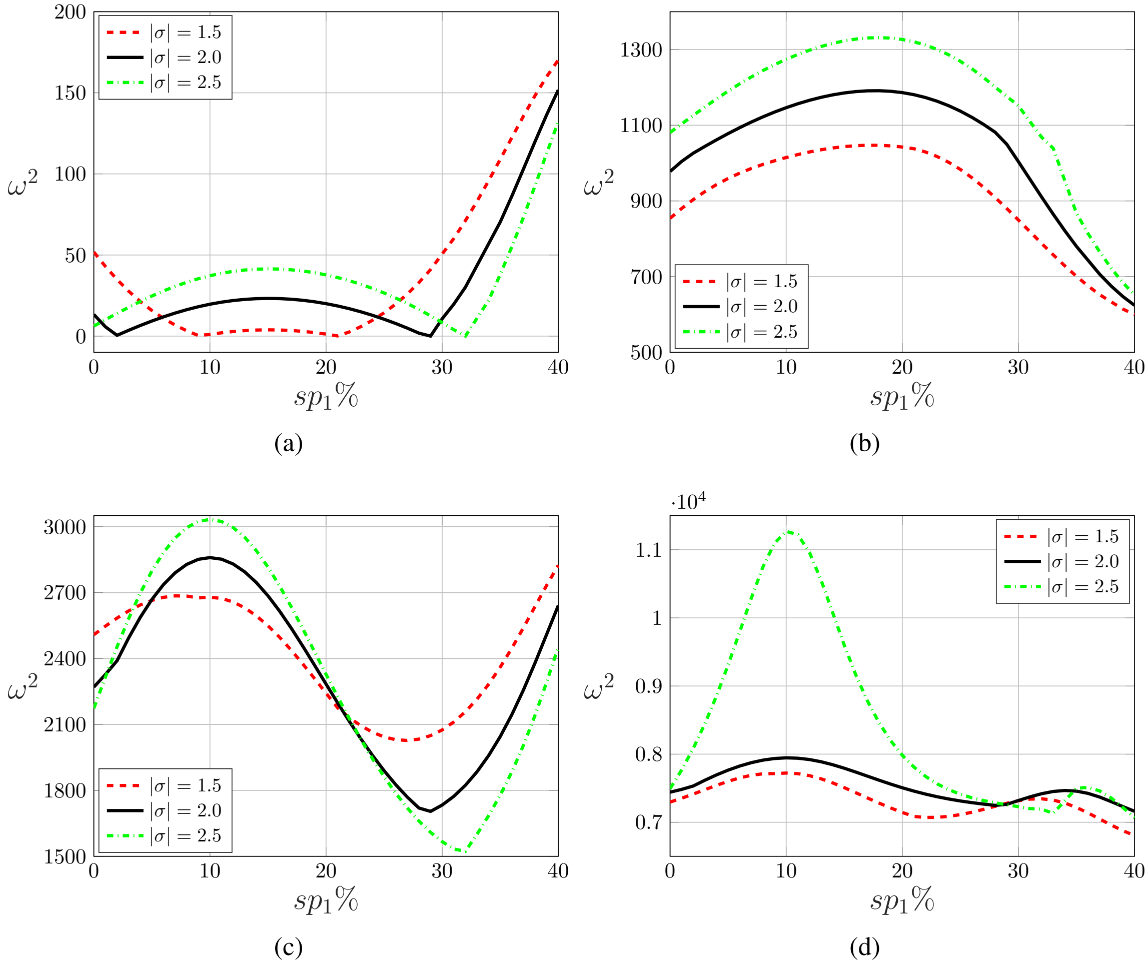

Figure 5.7. Non-dimensional natural frequency squared, ω^2, versus the start of the actuation region, $sp_1\%$, for $|\sigma| = 1.5$, 2.0, and 2.5. (a) First, (b) second, (c) third, and (d) fourth natural frequency.

Each of the first four natural frequencies shows a distinct and sensitive dependence on changes to the actuation length and actuation level. Information about the beam's underlying equilibrium shape and its stability can be inferred from the first natural frequency (Fig. 5.7(a)). The local maxima near $sp_1 = 15\%$ suggest that actuating the beam from 15% to 85% corresponds to a minimum in the actuation levels required to achieve a stable transition between remote equilibira. This is consistent with results in Ref. [130]. The marked increase in the first natural frequency when $sp_1 > 33\%$ suggests that the actuation levels being considered are not sufficient to deform the beam into an anti-symmetric 'S' shape. Rather, the actuated beam takes on a more stable equilibrium resembling its primary post-buckled shape. This result is also consistent with those in Chapter 4, where it is shown that short actuation regions need high levels of actuation to place the beam into the anti-symmetric shape required to execute stable transitions. In general, the changes in the higher-order natural frequencies are more pronounced at higher actuation levels. With $|\sigma| = 2$, the higher-order natural frequencies can be changed by as much as 20 to 30 percent by changing the length of the actuation region.

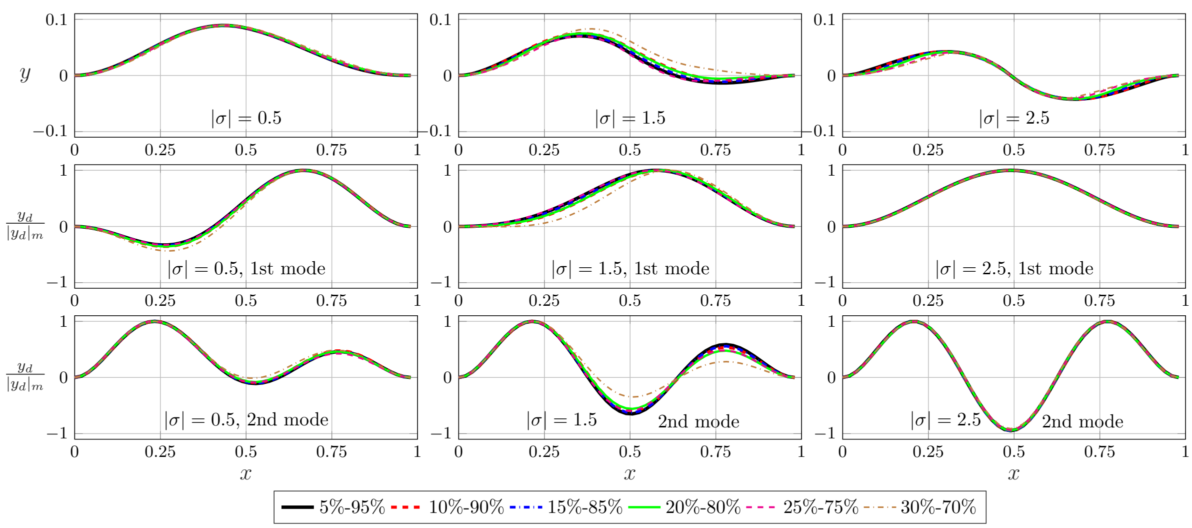

Figure 5.8. Equilibrium shapes and first two mode shapes of the beam for different actuation regions with $|\sigma| = 0.5$, 1.5, and 2.5.

Fig. 5.8 shows the equilibrium and mode shapes of an unloaded beam for different actuation regions with $|\sigma| = 0.5$, 1.5, and 2.5. Here, the piezoelectric material is actuated from 5%-95%, 10%-90%, 15%-85%, 20%-80%, 25%-75%, and 30%-70% of span. Considering the equilibrium shapes for $|\sigma| = 0.5$ and $|\sigma| = 1.5$ in Fig. 5.8, changing the length of the actuation region produces only minor changes in the beam's equilibrium shape, except for the case of the anti-symmetric equilibrium shape when the beam is actuated from 30%-70% of span. In this case, the mid-point of the beam has a larger deflection than it does in the other cases. This is consistent with the finding from Chapter 4 that it requires approximately 40% more actuation voltage to stabilize the anti-symmetric equilibrium shape in the 30%-70% case relative to other actuation regions. Similarly, Fig. 5.8 also shows that the mode shapes in the 30%-70% case are noticeably different from the other cases. At relatively high level of actuation ($|\sigma| = 2.5$), changing the actuation region has some minor effects on the equilibrium shapes, but practically no effect on the first two mode shapes. Considering the results in Figs 5.7 and 5.8 overall, it is concluded that changing the length of the actuation region has a significant effect on the beam's natural frequencies, but only minor effects on the corresponding mode shapes.

5.5 Experimental Validation

5.5.1 Experimental Setup

To experimentally determine the natural frequencies and mode shapes of a post-buckled and piezoelectrically activated beam, a test setup is devised and is shown in Fig. 5.9. A 50 cm $\times$ 2 cm $\times$ 0.25 mm strip of spring steel ($\rho_s =$ 7700 kg/m^3, $Y_s =$ 200 GPa) is clamped on both end and shortened by a desired distance. The beam is bonded with two patches of P1-type MFC (8.5 cm $\times$ 1.4 cm $\times$ 0.3 mm, $\rho_p =$ 5440 kg/m^3, $Y_p =$ 30.34 GPa, $d_{33} =$ 460 pm/V), and covers from 25% to 75% of the beam's span. One patch is bonded to the front of the beam and the other is bonded to the back. A high voltage amplifier (Smart Materials AMT2012-CE3) can supply -500 to 1500 volts to the patches. The beam is excited by a small modal hammer (PCB Model 086E80) to induce free vibration, and a laser optical displacement measurement sensor (Micro-Epsilon optoNCDT 1320) is used to measure the resulting time history.

Since the MFC covers only a portion of the test beam, the flexural rigidity and mass density are not constant along its length. To non-dimensionalize the natural frequencies obtained in test, an effective flexural rigidity and mass density is used. These effective values are calculated by taking a weighted average of the material properties, i.e.,

$$YI_{eff} = a_1 YI + a_2 YI_s, \quad \mu_{eff} = a_1 \mu + a_2 \mu_s, \tag{5.1}$$

where a_1 and a_2 are the portion of the beam bonded with and without MFC, respectively. The flexural rigidity of the substrate is $YI_s = Y_s b h_s^3/12$, and the mass per unit length of the substrate is given by

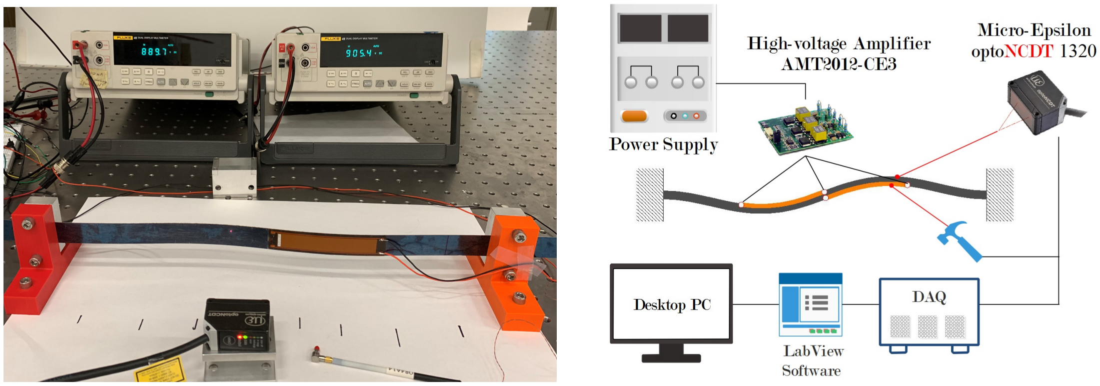

(a) (b)

Figure 5.9. (a) Photo, and (b) schematic of the experimental setup with one MFC patch placed on either side of the beam. The patches cover roughly the middle 50% of span.

$\mu_s = \rho_s b h_s$. The effective flexural rigidity and mass density of the test article is shown in Table 5.1 along with other pertinent parameters. Also included in Table 5.1 is a comparison between the first two numerical and experimental natural frequencies of the unactuated beam. The predicted results are within 1.4% of the experimental results, indicating that the use of effective properties is a justified approximation.

Table 5.1. Properties, natural frequencies, and damping of the unactuated test article

	25%-75% of span	
Length l (cm)	38.60	
End shortening e	0.02	
Fraction of beam with MFC a_1	0.50	
Effective flexural rigidity (Nm^{-2})	0.0109	
Effective mass ratio (kg/m)	0.0548	
	1st mode	2nd mode
Theory f^* (Hz)	21.37	35.99
Experiment f^* (Hz)	21.46	36.47
Experiment ζ	0.0142	0.0073

The modal hammer strikes the beam at locations near 7%, 21%, 32%, 43%, 50%, 57%, 68%, 79% and 93% of span. After the experimental displacement time history is obtained, it is converted to an amplitude spectrum using a fast Fourier transform (FFT), and the half-power point method is used to estimate the

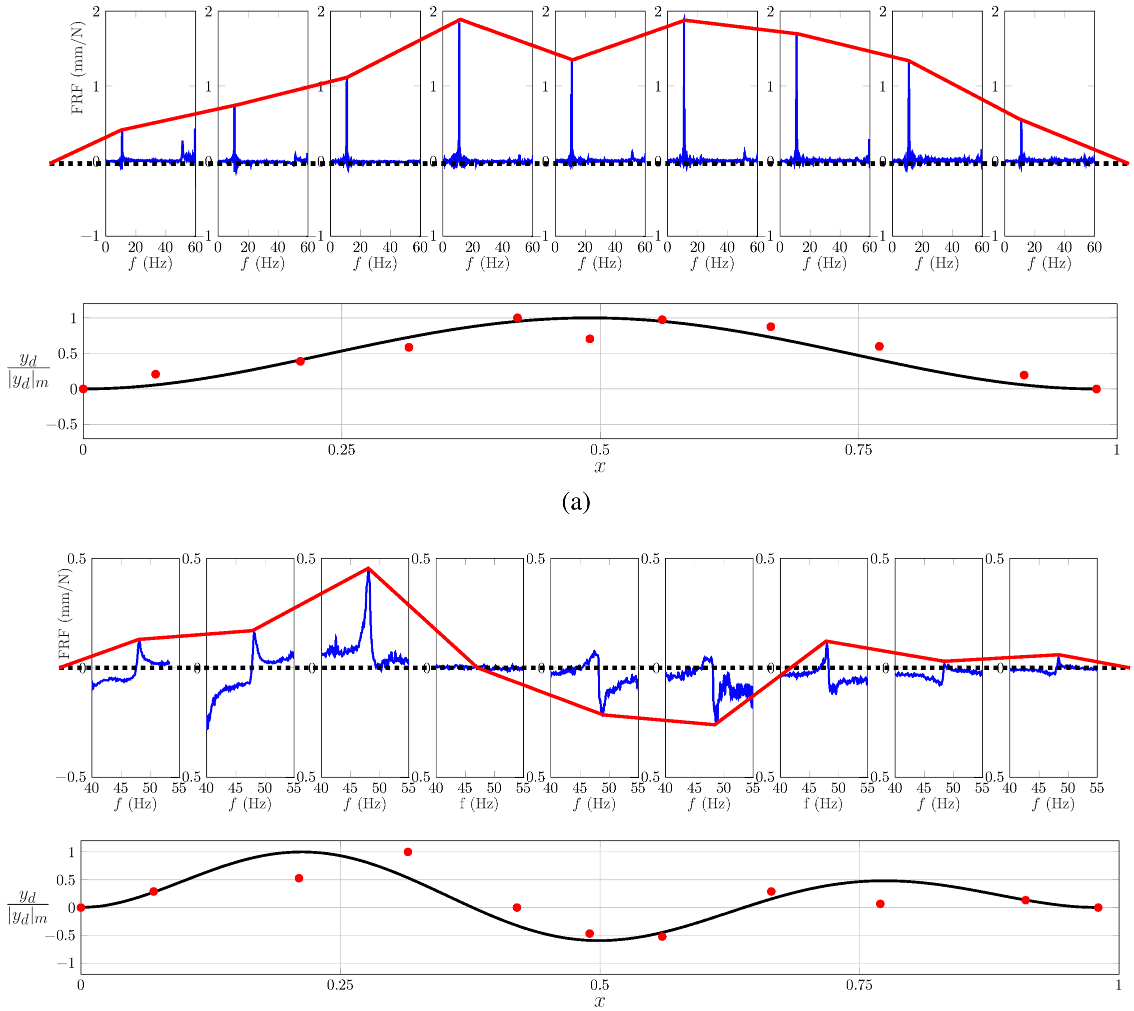

(a)

(b)

Figure 5.10. Example experimental FRF data and mode shapes. (a) The first mode shape of the beam with $|\sigma| = 2$ at a frequency of 8.09 Hz, and (b) the second mode shape of the beam with $|\sigma| = 1.5$ with a frequency of 48.22 Hz. In the lower plot in each part, the experimental mode points (markers) are overlaid on the numerical prediction (solid line).

viscous damping ratio, ζ, associated with each mode [131]. The theoretical dimensional natural frequency is calculated by $f^* = \omega\sqrt{YI_{eff}/(4\mu_{eff}l^4)}$ and the experimental natural frequency is calculated from $f^* = \bar{f}/\sqrt{1-\zeta^2}$, where $\bar{f}$ is the damped natural frequency [129]. Frequency response functions (FRFs) are calculated by dividing the FFT of the response by the FFT of the modal hammer input signal. At each strike location, the component of a given mode shapes is given by the imaginary part of the FRF at the corresponding natural frequency. Fig. 5.10 show representative FRF results and the corresponding numerical and experimental mode shape. Both the numerical and experimental mode shapes are normalized by their respective maxima. The modal assurance criterion (MAC) [132] comparing the numerical and experimental modes is 0.95 for the first mode, and 0.77 for the second, indicating good agreement between the theory and experiment.

5.5.2 Numerical and Experimental Data Comparison

To experimentally validate how the natural frequencies and mode shapes change as the beam undergoes a stable transition, two actuation schemes are considered. In both schemes, separate positive voltages are applied to frontside and backside MFC patches. Since the patches are on opposite sides of the beam, positive voltages are applied to both patches to obtain oppositely signed values of σ. Both the symmetry and loop paths are considered. Throughout all experimental trials, the voltages are changed in 120 volt increments.

Natural frequency maps of the symmetry and loop transition paths are shown in Fig. 5.11, where data are collected from three experimental trials for each path. Triangles in Fig. 5.11(a) represent the transition from the primary equilibrium shape to the 'S' shape, and dots indicate the other half of the transition. Solid and dashed curves show the numerically identified first and second natural frequencies, respectively, while the markers indicate the experimental data.

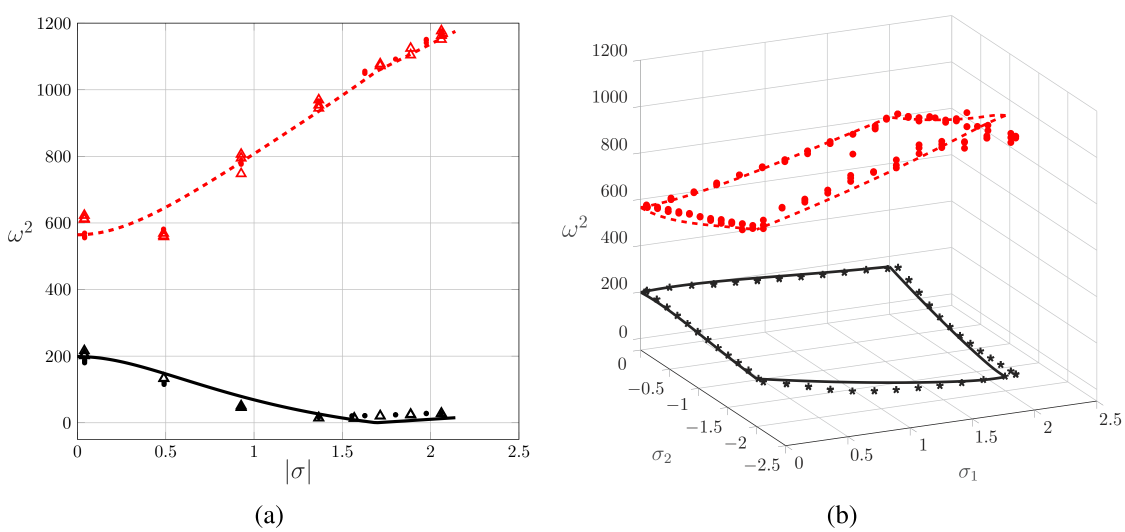

Figure 5.11. Non-dimensional natural frequency squared, ω^2, versus electromechanical coupling parameter for (a) the symmetry path, and (b) the loop path. Solid and dashed curves indicate the numerical first and second natural frequencies, respectively, and markers indicate experimental data.

Fig. 5.11(a) confirms the theoretical results; namely, increasing voltage first reduces the first natural frequency to nearly zero around $|\sigma| = 1.7$, and is followed by a slight increase in natural frequency. Meanwhile, the second natural frequency monotonically increases as the magnitude of the voltage increases. Fig. 5.11(b) shows the first two numerical and experimental natural frequencies associated with the loop path. Across all experimental trials, the natural frequencies correlate well. Overall, the average absolute percent differences between the numerical and experimental natural frequencies are 6.83% and 3.79% for the first and second mode of the symmetry path, and 5.16% and 5.88% for the first and second mode of the loop path.

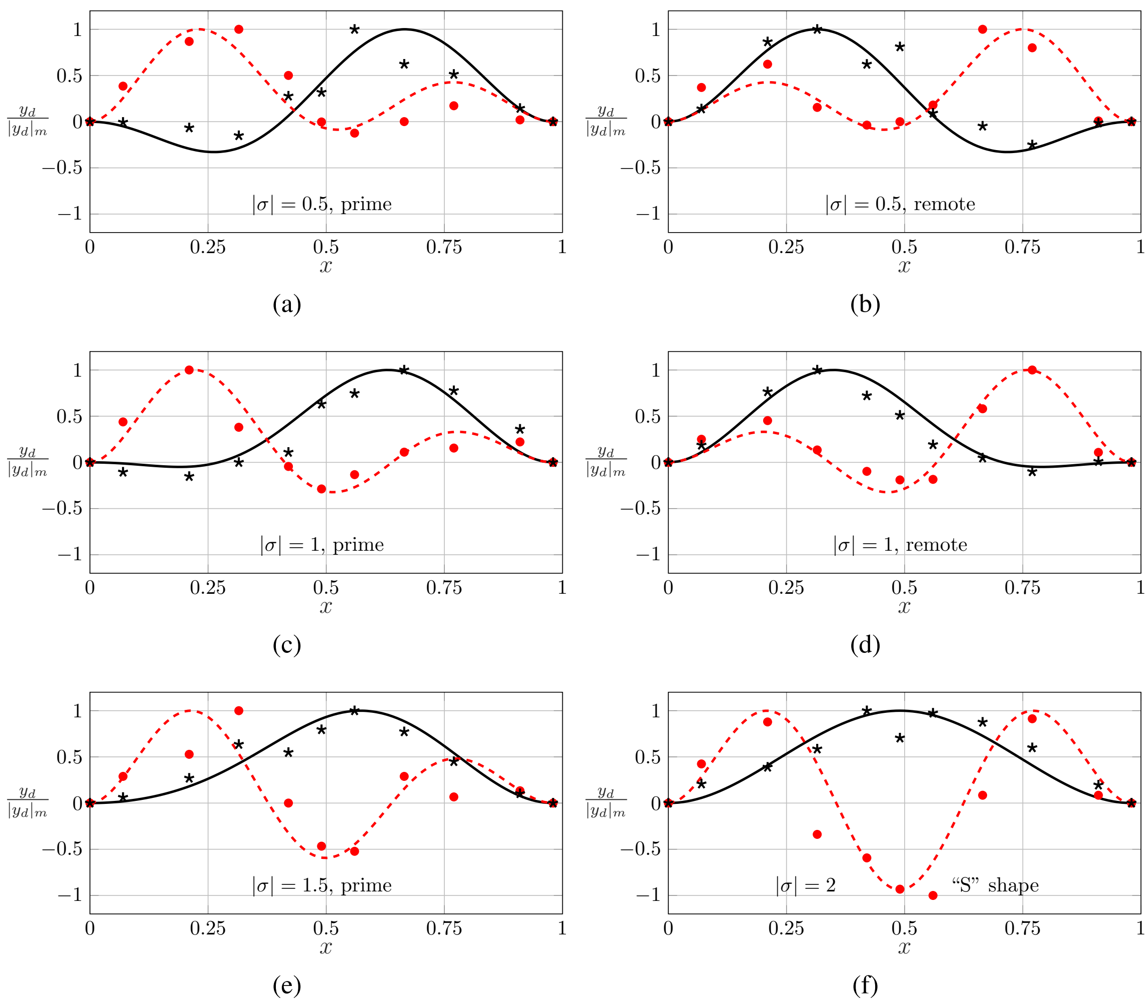

Figure 5.12. Numerical (lines) and experimental (markers) mode shapes from a stable transition along the symmetry path. The beam is at its (a) primary and (b) remote equilibrium position with $|\sigma| = 0.5$, its (c) primary and (d) remote position with $|\sigma| = 1$, its (e) primary equilibrium for $|\sigma| = 1.5$, and in an (f) anti-symmetric shape with $|\sigma| = 2$.

Normalized dynamic deflections of the first two modes with experimental data are shown in Fig. 5.12. Data are recorded from three taps at the each location actuated with $|\sigma| = 0.5$, 1, 1.5, and 2. FRFs from a given response point/strike point pair are averaged and corresponding peaks are then extracted from the averaged FRF results. The mode shapes of the beam are mutually symmetric at the primary and remote equilibria when actuating with the same voltage. Experiments validate the mode shapes well, and they are able to track the changes of mode shapes during the stable transition. The MAC values comparing the spatial similarity of the numerical and experiment modes are shown in Table 5.2. The fact that most of the MAC values are above 0.9 suggests strong agreement between the numerical model and the experiment.

Table 5.2. Modal assurance criterion (MAC) comparing the numerical and experimental modes.

	$\lvert\sigma\rvert = 0.5$	$\lvert\sigma\rvert = 0.5$ (remote)	$\lvert\sigma\rvert = 1.0$	$\lvert\sigma\rvert = 1.0$ (remote)	$\lvert\sigma\rvert = 1.5$	$\lvert\sigma\rvert = 2.0$
First mode	0.86	0.93	0.94	0.97	0.97	0.95
Second mode	0.85	0.92	0.91	0.94	0.77	0.79

5.6 Conclusions

This chapter investigates modal behavior of a clamped-clamped post-buckled beam. Modal analysis of post-buckled structures about given stable equilibria contribute to the understanding of the structural dynamics of post-buckled structures under different loading environments and actuation configurations. Numerical and experimental results validate the changes to natural frequencies and mode shapes of a beam stably transitioning from a primary equilibrium to a remote one. Natural frequency results show the reduction of the first and third natural frequency to a minimum when the beam assumes an anti-symmetric equilibrium, and show a corresponding increase to the second and fourth natural frequencies. The beam exhibits localized mode shapes when it is placed into an asymmetric equilibrium by actuation and/or an applied load. The modes associated with the anti-symmetric equilibrium shape are symmetric about the beam's mid-point, however. The numerical natural frequencies and mode shape predictions are validated with experiments.

Chapter 6

Stabilizing Higher-Order Equilibria of Post-buckled Beams

6.1 Overview

The higher-order static equilibria of post-buckled structures are normally unstable. It has been shown in Chapter 4 that by intelligently actuating two piezoelectric patches bonded to a post-buckled beam, the second-order equilibria can be stabilized and the beam can be made to stably transition from one first-order post-buckled shape to the other, thereby avoiding snap-through. This chapter identifies and determines the stability of higher-order equilibra of clamped-clamped post-buckled beams under piezoelectric actuation. The beam is bonded with distributed patches of piezoelectric films. The conditions giving rise to stable third- and fourth-order equilibrium shapes of the post-buckled beams are investigated. Stable third- and fourth-order equilibria are found under certain conditions. Third-order stable equilibria can be obtained for low activation voltages using a large actuation region; similarly, they can also be attained for high levels of actuation voltage using short actuation regions. Fourth-order stable equilibria are eventually achieved if the actuation voltage exceeds a critical value. Stabilized third- and fourth-order equilibria are demonstrated experimentally and correlate well with numerical predictions.

All beams are assumed to be post-buckled and clamped on both ends. Piezoelectric material covers one side of the beam, as shown in Fig 6.1. Different piezoelectric patches are bonded to the beam for different actuation schemes, and different voltages, V_1, V_2, and up to V_n, are applied to each patch. The structural behavior is expressed in terms of the mid-point deflection, δ, while the applied voltages are the control parameters. The non-dimensional parameters, σ_1 to σ_n, are proportional to the voltage applied to each piezoelectric patch.

To observe equilibrium shapes of higher order, the range of considered σ values is extended to $+/-15$. The piezoelectric material is assumed to cover the entire beam, but only a portion is actuated. Here, cases in which there are three or four piezoelectric patches are considered. In each case, it is assumed that all patches have the same length.

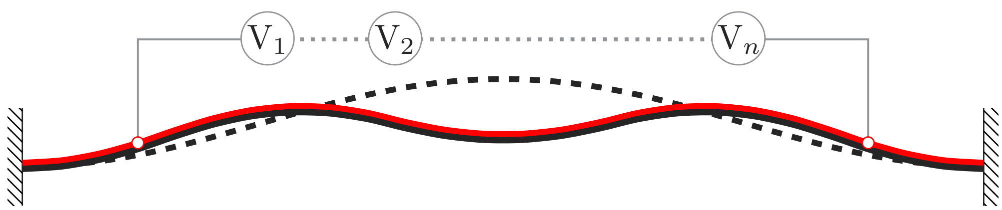

Figure 6.1. Schematic of a clamped-clamped post-buckled beam bonded with piezoelectric patches on its top surface.

Based on a preliminary study, one patch of piezoelectric material can maintain a stable first-order equilibrium shape, and two patches can stabilize the anti-symmetric shape (second-order) [130]. The hypothesis is that higher-order shapes can be achieved when higher numbers of piezoelecric patches are used. The actuation region is specified with the parameters, sp_1 and sp_3, which denote the percent of span between $s = 0$ and the beginning and the end of the actuated region, respectively.

6.2 Third-Order Equilibrium Shapes

To investigate the stability of third-order equilibria, three identical patches of piezoelectric material are assumed to be placed end-to-end and centered on the beam, as shown in Fig. 6.2. A positive voltage (σ_1) is applied to the first and third patches, and a negative voltage (σ_2) is applied to the center patch.

6.2.1 Symmetric Actuation Voltage

The simplest actuation strategy is to actuate the three patches with voltages of equal magnitude. For the case shown in Fig. 6.3, three active patches are assumed from 0% to 33%, from 33% to 67%, and from 67% to 100% of span. The patches are actuated such that the non-dimensional actuation parameters associated with

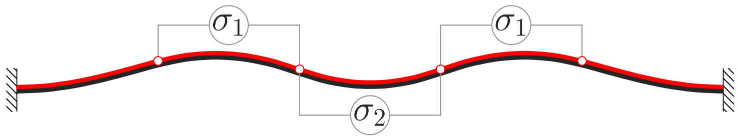

Figure 6.2. Schematic of a clamped-clamped post-buckled beam bonded with three patches of piezoelectric material.

each patch are equal to $+\sigma$, $-\sigma$ and $+\sigma$. Fig. 6.3 shows (a) the normalized mid-point deflections and (b) the corresponding natural frequencies squared versus $|\sigma|$ for a beam with a non-dimensional end shortening of $e = 0.02$. The first-, second-, and third-order equilibrium branches are shown. The mid-point deflections under actuation, δ, are normalized by the mid-point deflections without actuation, δ_0. Only the $+\sigma$, $-\sigma$ and $+\sigma$ results are represented since the deflection versus $|\sigma|$ results for the $-\sigma$, $+\sigma$, and $-\sigma$ case are simply a mirror image about $\delta/\delta_0 = 0$. Further, the natural frequency results for the $-\sigma$, $+\sigma$, and $-\sigma$ case are the same as those shown in Fig. 6.3 (b). Stable and unstable equilibria are indicated by solid and dashed lines, respectively.

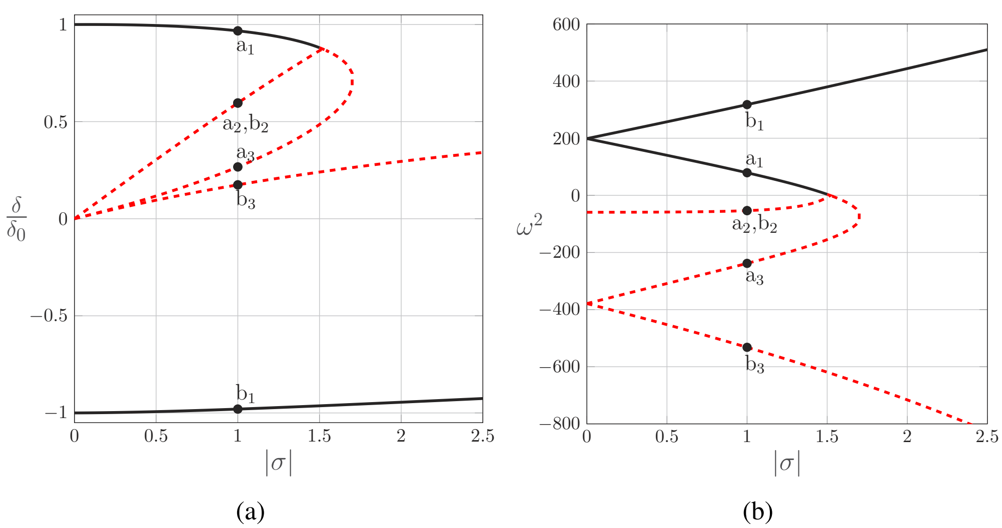

Figure 6.3. (a) Normalized mid-point deflection, δ/δ_0, (b) non-dimensional natural frequency squared, ω^2, versus the magnitude of the non-dimensional actuation parameter, $|\sigma|$, for $e = 0.02$ and the six lowest-order equilibria. Stability is indicated by solid (stable) or dashed (unstable) lines. The symbols a and b indicate upper and lower branches of equilibria, respectively, while the subscript indicates the order.

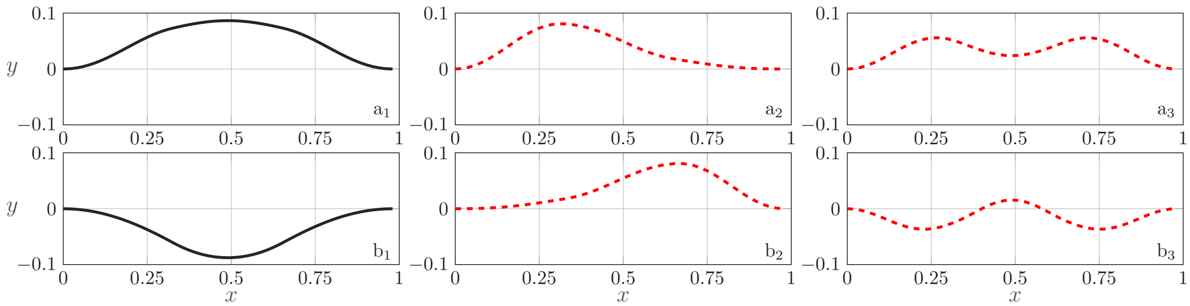

Figure 6.4. Static equilibrium shapes for the first six equilibria with $|\sigma| = 1$. Stability is indicated by solid (stable) or dashed (unstable) lines. For each shape, the corresponding point on the equilibrium curve is indicated in Fig. 6.3. The symbols a and b indicate upper and lower branches of equilibria, respectively, while the subscript indicates the order.

In Fig. 6.3(a), both the primary and remote first-order equilibria are stable for low values of $|\sigma|$. Near $|\sigma| = 1.5$, the primary first-order equilibrium loses stability, and upon an increase in $|\sigma|$, will snap-though to the remote first-order equilibrium. All of the second and third-order equilibria are unstable across the range of $|\sigma|$. As will be shown, this is a consequence of the entire span of the beam being electrically active. Confining the actuation region to a portion of the beam's span gives rise to stable third-order shapes. Fig. 6.4 shows the first-, second-, and third-order equilibrium shapes when $|\sigma| = 1$. The symbols a and b indicate upper and lower branches of equilibria, respectively, while the subscript indicates the order.

Fig. 6.5 focuses primarily on the upper branches of the first- and third-order equilibria for various assumed actuation regions (0% to 100%, 10% to 90%, 20% to 80%, and 30% to 70% of span). The beam has an end-shortening of $e = 0.02$. In each case, the actuation region is divided into three patches of equal length and the patches are actuated according to the $+\sigma$, $-\sigma$, $+\sigma$ scheme. The boundaries between the first and third branches occur at limit points of vertical tangency. In all cases except for the 30% to 70% case, the upper branches of the first- and third-order equilibria converge at some value of $|\sigma|$. Points of interest are indicated with markers and the corresponding equilibrium shapes are shown in Fig. 6.6. The letters a and b again denote upper and lower branches while the first number in the subscript denotes the order of the equilibrium. The second subscript number indicates one of the four considered actuation regions, with one being the 0% to 100% case and four being the 30% to 70% case.

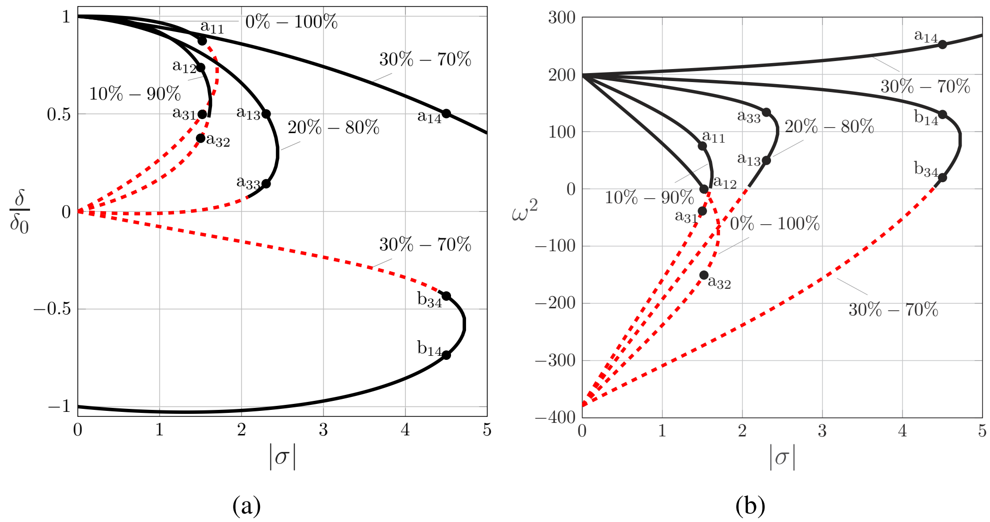

Figure 6.5. (a) Normalized mid-point deflection, δ/δ_0, (b) non-dimensional natural frequency squared, ω^2, versus the magnitude of the non-dimensional electromechanical coupling parameter, $|\sigma|$, for $e = 0.02$. Stable and unstable paths are indicated with solid and dashed lines, respectively. The piezoelectric material is actuated from 0% to 100%, 10% to 90%, 20% to 80%, and 30% to 70% of span. The letters a and b again denote upper and lower branches. The first number in the subscript denotes the order of the equilibrium while the second subscript number indicates considered actuation regions.

In Fig. 6.5, for an actuation region of 0%-100%, the third-order equilibrium shape cannot be stabilized. For the 10% to 90% actuation region, the third-order equilibrium can stabilize over a narrow range of $|\sigma|$ values ($|\sigma|$ =1.6-1.62). Decreasing the actuation region to be between 20% and 80% of span increases the size of this stable range, albeit for higher levels of actuation ($|\sigma|$ =2.08 to 2.44). For the 30% to 70% actuation region, three stable equilibria are observed at high $|\sigma|$ values. With increasing $|\sigma|$, the beam remains stable along the upper first-order branch, and in fact, becomes more stable as $|\sigma|$ increases. This indicates that when the actuation region is from 30% to 70% of span, it is impossible for an unloaded beam to snap-through under the present actuation scheme. Another feature of the 30% to 70% case is that the third-order equilibrium branch stabilizes at high $|\sigma|$ values by converging with the lower first-order branch. There are three stable equilibria that occur at $|\sigma| = 4.5$ and the corresponding shapes are shown in the right-most panel of Fig. 6.6.

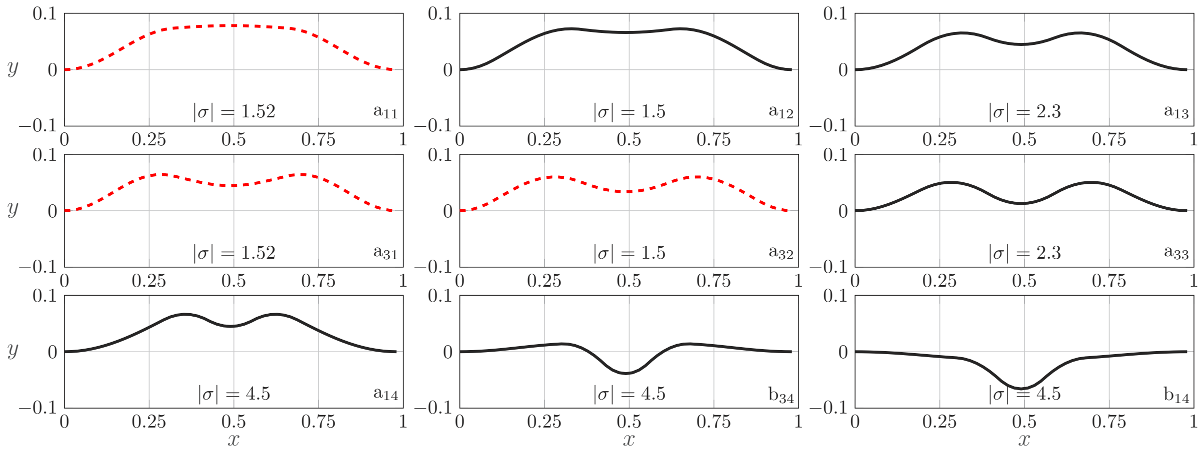

Figure 6.6. Static equilibrium shapes for select values of $|\sigma|$. Solid and dashed lines indicate stable and unstable states, respectively. The a_{11} and a_{31} shapes are the equilibria with $|\sigma| = 1.52$ and the beam actuated across the entire span. The a_{12} and a_{32} shapes belong to the first- and third-order upper branch, respectively, when $|\sigma| = 1.5$ and the beam is actuated from 10% to 90% of span. The a_{13} and a_{33} are both stable third-order shapes with $|\sigma| = 2.3$ and the beam actuated from 20% to 80% of span. The a_{14}, b_{34}, and b_{14} are the three stable equilibria at $|\sigma| = 4.5$ and the beam actuated from 30% to 70% of span.

It is clear from Fig. 6.5 that the length of the actuation region has a considerable effect on the beam's stability under actuation. In Fig. 6.7, the length of actuation region and $|\sigma|$ are varied to generate a surface of normalized mid-point deflections. The length of the actuation region is denoted by sp_1, which indicates the start of the actuation region as a fraction of the beam's span. The end of the actuation region (denoted sp_3 elsewhere) is assumed to be 1-sp_1. Note that only first-order branches that connect to a third-order branch are shown. For $sp_1 \gtrapprox 25\%$, the upper first-order branch no longer connects to the third-order branch (as observed in the 30% to 70% case in Fig. 6.5). Similarly, for $sp_1 \lessapprox 25\%$, the lower first-order branch does not connect to the lower third-order branch. For clarity, these unconnected first-order equilibria are not shown.

Note that a common plotting scheme is used in Figs. 6.7—6.10. In this scheme, gray- and blue-shaded areas represent first-order and third-order equilibria, respectively, with the lighter shade of each color indicating unstable equilibria while the darker shade denotes stable equilibria. Dashed lines are used to indicate the boundary between stable and unstable equlibria and red dotted lines indicate the boundaries of the first- and third-order equilibria. The region of stable third-order equilibria is further sub-classified using green

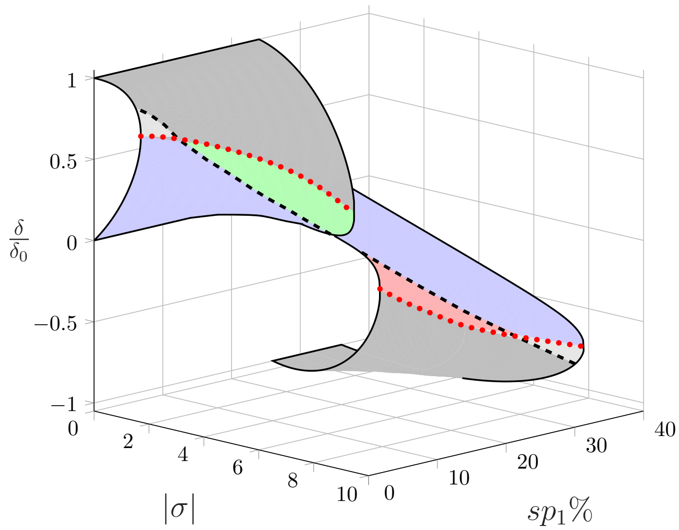

Figure 6.7. Normalized mid-point deflection, δ/δ_0, versus $|\sigma|$, and the start of the actuation region, sp_1, for $e = 0.02$ with three piezoelectric patches of equal length and actuation voltages of equal magnitude. Gray (blue) areas represent first- (third-) order equilibria, with darker shades indicating stable equilibria. Green and red areas are stable third-order equilibria that are adjacent to the upper and lower first-order branches, respectively. Red dotted lines indicate the boundaries of the first- and third-order equilibria and the black dashed line is the boundary between stable and unstable equilibria. This same plotting scheme also applies to Figs. 6.8—6.10.

and red shaded regions. The green region denotes stable third-order equilibria that are adjacent to only the upper first-order equilibrium branch while the equilibria in the red region are adjacent to only the lower first-order branch. Equlibiria that are shaded dark blue are stable third-order equilibria that are adjacent to both the upper and lower first-order branches.

Fig. 6.7 confirms a number of the observations from Fig. 6.5. When the actuation region covers nearly the entire span, the first-order upper branch destabilizes before connecting with the third-order branch. Consequently, stable third-order equilibria are not possible. As the length of the actuation region is reduced (i.e., sp_1 is increased), there is a (green shaded) region of stable third-order equilibria. When $sp_1 \gtrapprox 25\%$, the third-order branch switches such that it connects with the lower first-order equilibrium branch. As sp_1 reaches about 34%, the lower first-order branch destabilizes before connecting with the third-order branch. Thus, under the presumed actuation scheme, stable third-order equilibria are possible for actuation regions with sp_1 values ranging from approximately 8% to 34%. These sp_1 values correspond to actuation regions that comprise the center 84% to 32% of the beam's length. Fig. 6.7 also shows that there are no regions of

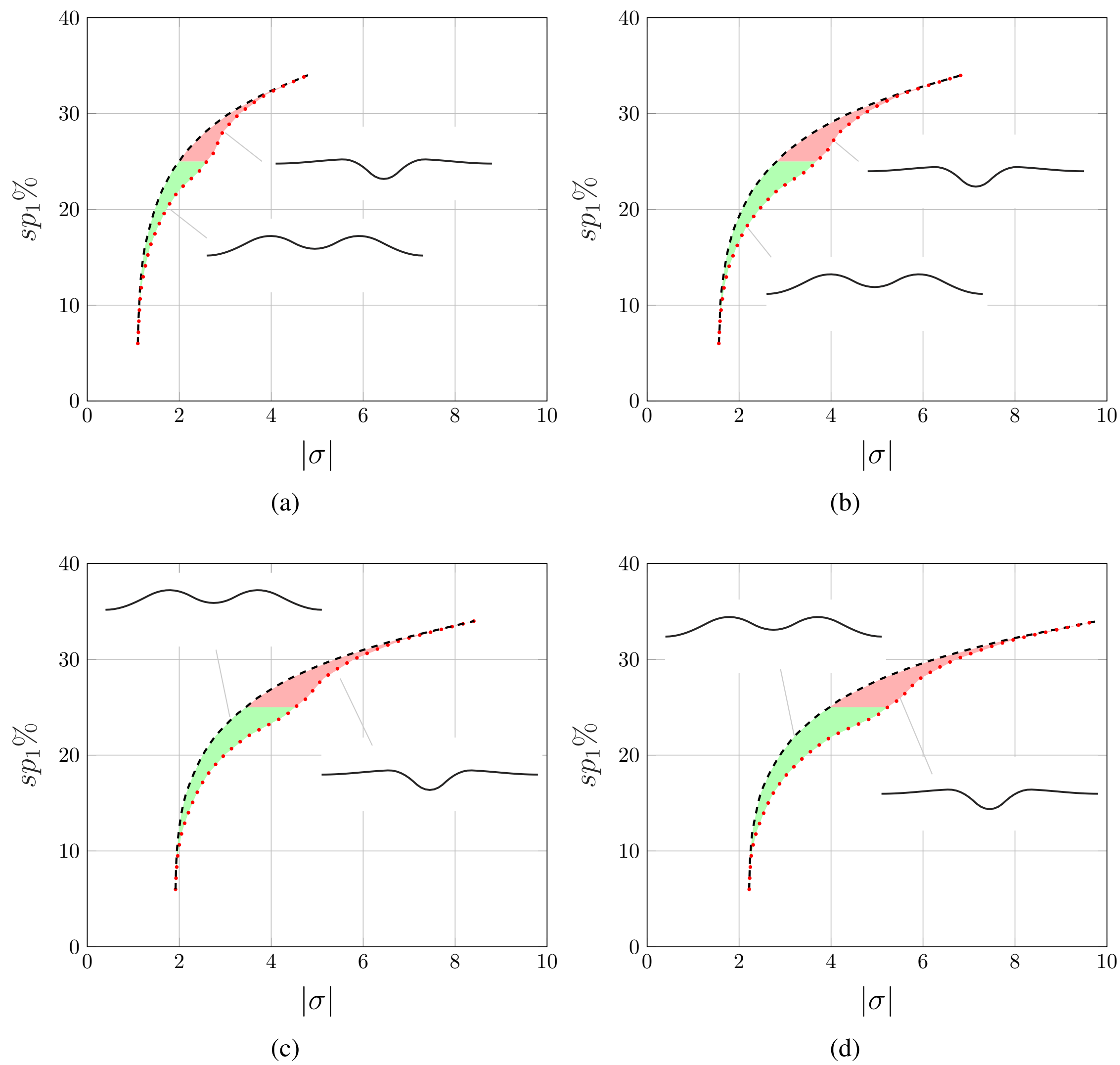

Figure 6.8. Projections of the stable areas of the third-order equilibrium onto the $|\sigma|$-sp_1 plane for (a) $e = 0.01$, (b) $e = 0.02$, (c) $e = 0.03$, and (d) $e = 0.04$. Three piezoelectric patches of equal length and actuation voltages of equal magnitude are assumed.

stable third-order equilibria which connect the upper first-order equilibria to the lower. This indicates that, at least for the present actuation scheme, it is not possible to stably transition from one first-order equilibrium to the other via a third-order shape.

Fig. 6.8 shows projections of the regions of stable third-order equilibria onto the $|\sigma|$-sp_1 plane for four different values of end shortening. The results show that the area of parameter space over which the third-order equilibrium can be stabilized increases slightly with end shortening. However, the minimum actuation voltages required to stabilize the third-order shapes increases slightly as well. For all end shortenings shown here, the third-order branch switches from connecting with the upper first-order branch to connecting with the lower first-order branch when $sp_1 \approx 25\%$.

6.2.2 Asymmetric Actuation Voltage

Now consider an asymmetric actuation scheme in which one of the three patches is actuated with a voltage of a magnitude that is different from the other two. For the cases considered here, a positive voltage (with a corresponding actuation parameter, σ_1) is applied to the first and third patches while a negative voltage (with a corresponding actuation parameter of σ_2) is applied to the center patch. The normalized mid-point deflection is shown against σ_1 and σ_2 in Fig. 6.9 for a beam with $e = 0.02$. The actuation region is from 10% to 90% of span in panel (a), and from 25% to 75% of span in panel (b).

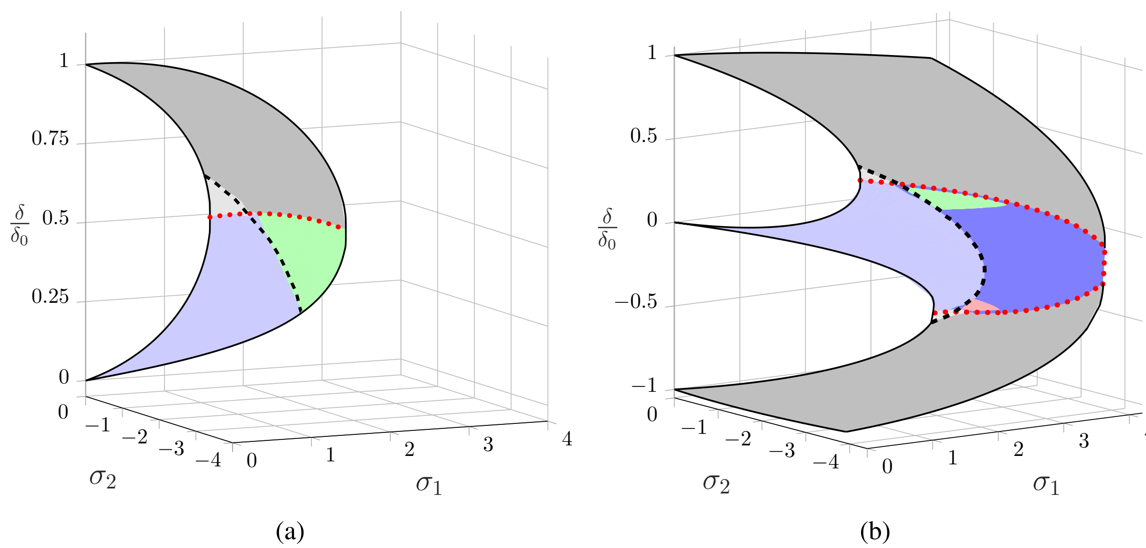

Figure 6.9. Normalized mid-point deflection, δ/δ_0, versus non-dimensional actuation parameters, σ_1 and σ_2 for $e = 0.02$. The piezoelectric material is actuated from (a) 10% to 90% of span and (b) 25% to 75% of span.

With an actuation region from 10% to 90% of span, Fig. 6.9 (a) shows that all possible equilibria of the third-order branch have mid-point deflections greater than zero and converge with the first-order upper branch. There is a relatively small wedge-shape region (shaded in green) in which the given combination of σ_1 and σ_2 results in a stable third-order equilibirium. With an actuation region from 25% to 75% of span, shown in Fig. 6.9 (b), the region of stable third-order equilibria increases in area. This includes a large

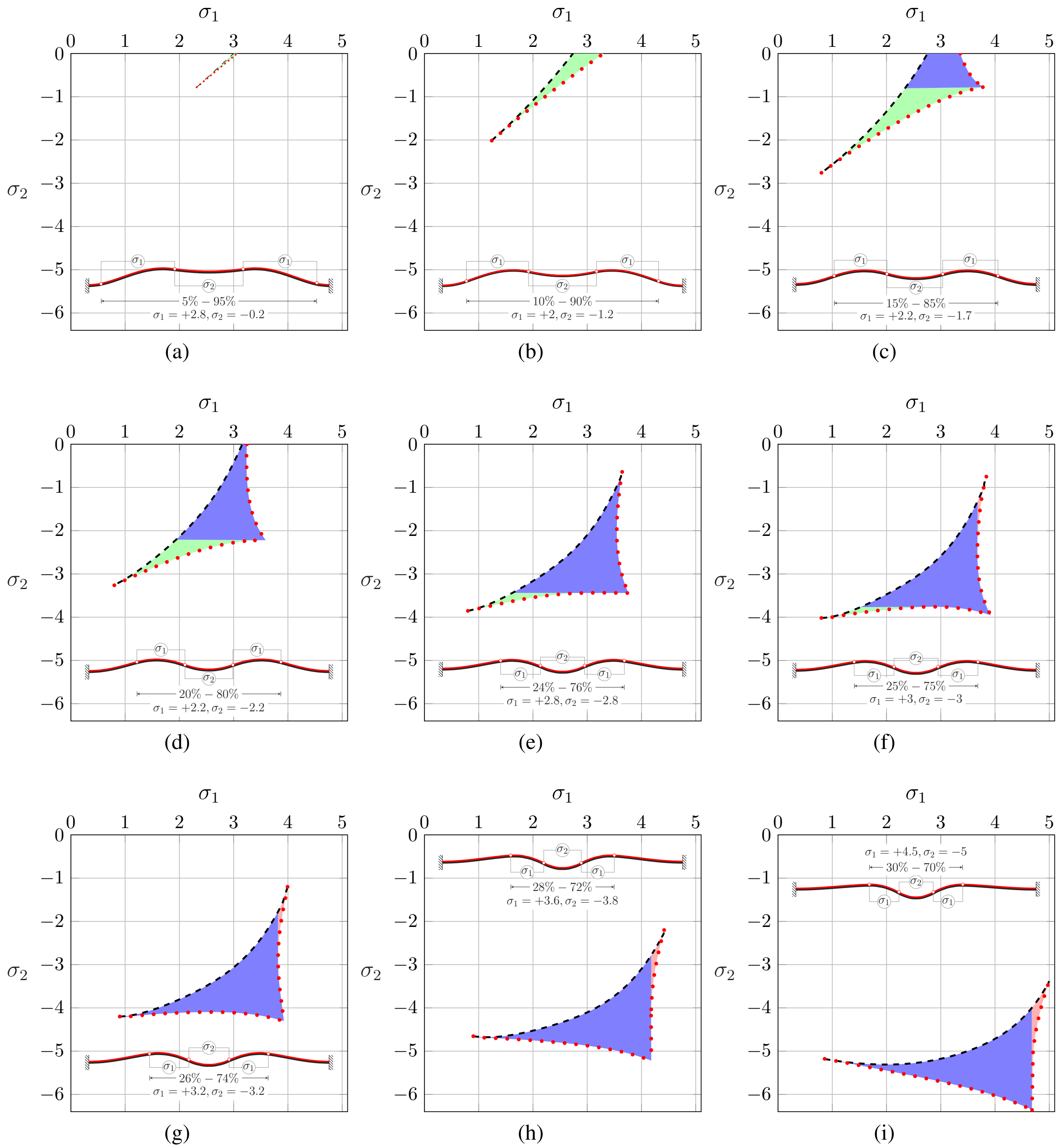

Figure 6.10. Regions of actuation space in which the third-order equilibrium is stable with $e = 0.02$ and piezoelectric patches of equal length. Nine different actuation regions are shown: (a) 5% to 95%, (b) 10% to 90%, (c) 15% to 85%, (d) 20% to 80%, (e) 24% to 76%, (f) 25% to 74%, (g) 26% to 74%, (h) 28% to 72%, and (i) 30% to 70%.

region of points (shaded in dark blue) that connect the upper branch of stable first-order equilibria with the lower branch. This suggests the potential to stably transition from one first-order equilibrium to the other via a stable third-order shape.

Fig. 6.10 shows projections of the regions of stable third-order equilibria onto the σ_1-σ_2 plane with $e = 0.02$. Results show nine different actuation regions ranging from $5\% \leqslant sp_1 \leqslant 30\%$ with $sp_3 = 100\% - sp_1$. Note that Fig. 6.10 (b) and (f) are the projections of Fig. 6.9(a) and (b), respectively. In all cases, a representative stable third-order equilibrium shape is shown along with its corresponding σ_1 and σ_2 values.

The subplots in Fig. 6.10 show that the area in which the third-order equilibrium is stable are sensitive to both the actuation voltages and the actuation region, especially as the actuation region approaches 25%-75% of span. In general, the absolute values of σ_1 and σ_2 that achieve stable third-order equilibria continuously increase as the length of the actuation region decreases. For large actuation regions, the third-order equilibrium can stabilize over a very narrow range of σ values, and all equilibria converge to the upper first-order branch. As the length of the actuation region decreases, the region of stable third-order equilibria becomes larger. When the actuation region decreases to $10\% \leqslant sp_1 \leqslant 15\%$, an area (shaded dark blue) of stable third-order equilibria connecting the two first-order branches appears. Configurations that give rise to these areas thus exhibit entirely stable paths linking the two remote first-order equilibria.

6.3 Fourth-Order Equilibrium Shapes

To investigate the possibility of stabilizing fourth-order equilibria, four patches of piezoelectric material are configured on the beam as shown in Fig. 6.11. Positive voltage (with corresponding actuation parameter, σ_1) is applied to the first and third patches, and negative voltage (with corresponding actuation parameter, σ_2) is applied to the second and fourth patches.

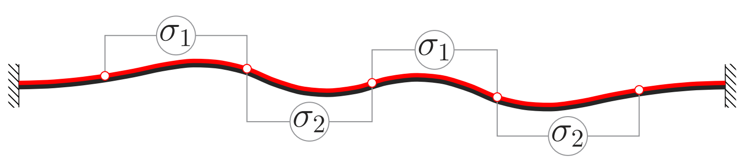

Figure 6.11. Schematic of a clamped-clamped post-buckled beam with four piezoelectric patches.

6.3.1 Symmetric Actuation Voltage

For the symmetric actuation scheme, the actuation region is divided into four patches of equal length with actuation parameters given by $+\sigma$, $-\sigma$, $+\sigma$, and $-\sigma$. Consequently, the absolute value of σ is the only control parameter. Normalized mid-point deflections and the squared natural frequencies are shown in Fig. 6.12 for an end shortening of $e = 0.02$. Four different actuation regions are assumed: from 2% to 98%, from 10% to 90%, from 20% to 80%, and from 30% to 70% of span.

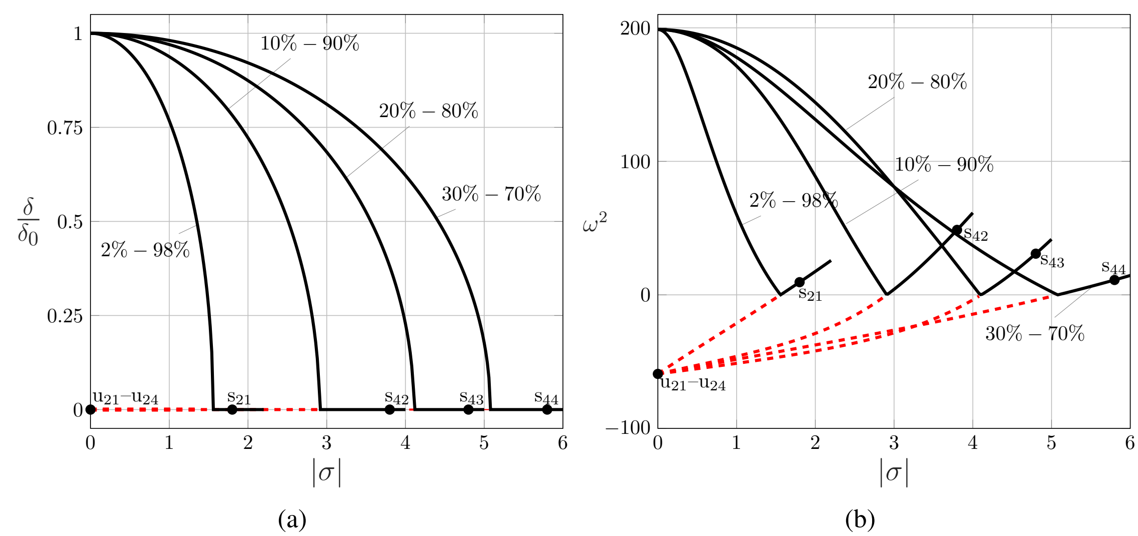

Figure 6.12. (a) Normalized mid-point deflection, δ/δ_0, (b) non-dimensional natural frequency squared, ω^2, versus the non-dimensional actuation parameter, $|\sigma|$, with $e = 0.02$. Stable (unstable) paths are indicated with solid (dashed) lines. The piezoelectric material is actuated from 2% to 98%, 10% to 90%, 20% to 80%, and 30% to 70% of span.

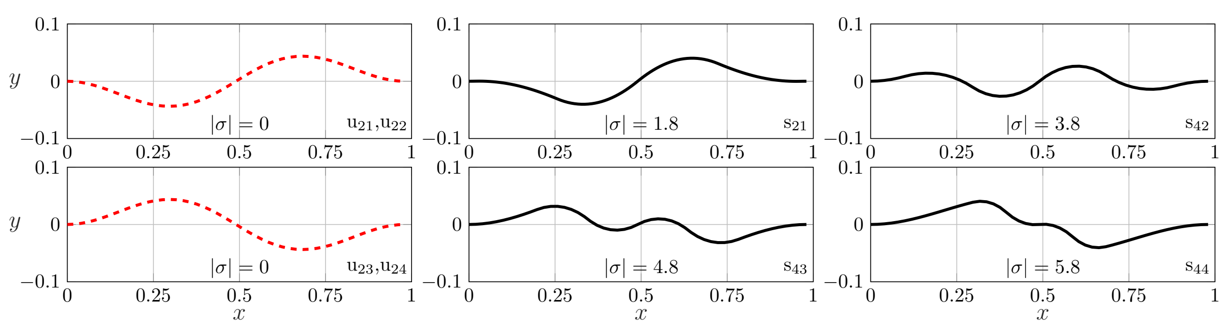

Figure 6.13. Static equilibrium shapes for select values of $|\sigma|$. Solid lines and dashed lines indicate stable and unstable states, respectively.

Fig. 6.12 shows that all the first-order branches remain stable with increasing $|\sigma|$. The second- and fourth-order equilibria have zero mid-point deflection across all actuation voltages. These higher-order equilibria are unstable at low values of $|\sigma|$, but stabilize at higher values. As the length of actuation region reduces, higher levels of voltage are needed to stabilize the higher-order branch. In all cases, the first-order and higher-order equilibrium branches converge at some value of $|\sigma|$. Beyond this value, a stable equilibrium exists and it will have either second-order or fourth-order shape. To distinguish between second-order and fourth-order the number of stationary points (i.e., $dy/dx = 0$) are counted for each candidate shape. A second-order shape has two stationary points and fourth-order shape has four points.

Fig. 6.13 shows static equilibrium shapes at select values of $|\sigma|$ corresponding to Fig. 6.12. Letters s and u indicate the stable and unstable equilibria. The first subscript number indicates the order of the equilibrium and the second number corresponds to the actuation case with the 2% to 98% case given by one and the 30% to 70% case denoted by four. Static equilibria are indicated with solid lines while unstable equilibria are shown with dashed lines.

Fig. 6.14(a)-(c) show stable and unstable areas of second- and fourth-order equilibria with respect to $|\sigma|$ and sp_1 for different values of non-dimensional end shortening ($e = 0.01$, 0.02, and 0.04). Boundaries of stable and unstable equilibria are indicated by black dashed lines, and the red dashed lines are the boundaries between the second- and fourth-order shapes. There are two branches of second-order equilibria and with increasing values of $|\sigma|$, either one may give rise to a stable fourth-order shape. The two shaded areas in Fig. 6.14(a)-(c) are used to distinguish those stable fourth-order shapes that arise from one second-order branch from those arising from the other. The boundary between these two shaded regions consistently occurs near $sp_1 = 15\%$ regardless of the amount of end shortening. For long actuation regions (i.e., low values of sp_1) and increasing $|\sigma|$, the fourth-order shapes start forming before stabilizing. As the length of the actuation region decreases such that $sp_1 \geqslant 30\%$, stable second-order equilibria appear first, and are followed by stable fourth-order shapes at higher levels of actuation voltage.

The boundaries of stability for fourth-order shapes are shown for different amounts of end shortening in Fig. 6.14(d). Not surprisingly, it requires increasing levels of actuation voltage to stabilize the fourth-order shapes when the beam is more severely buckled. The shape of the stability boundary also becomes more complicated as end shortening is increased. The open markers in Fig. 6.14(d) indicate the point at which the stable fourth-order equilibria switch from those that arise from one of the second-order branches to those

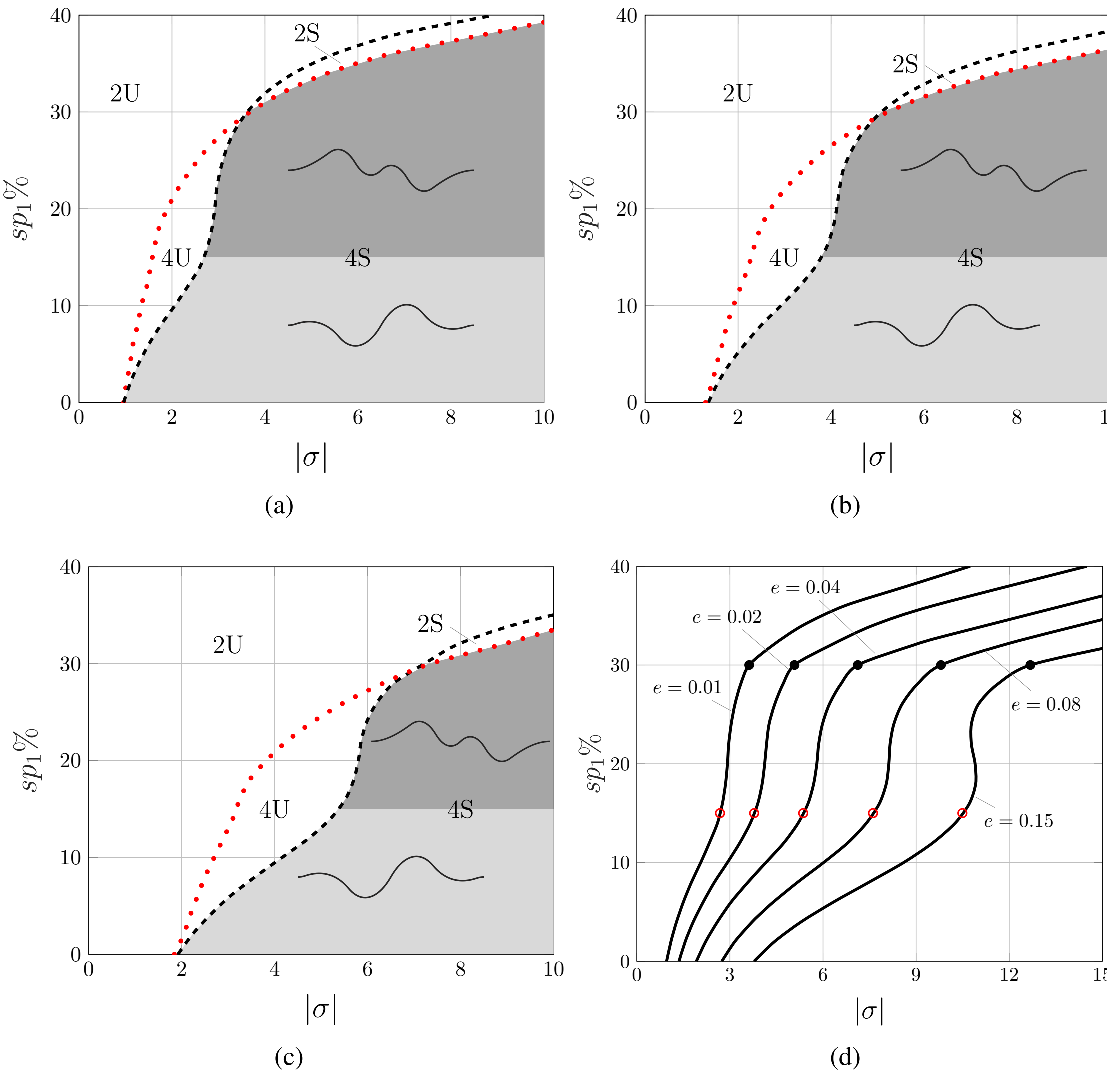

Figure 6.14. Projections of stable/unstable area of the second- and fourth-order equilibria onto the non-dimensional $|\sigma|$ and the beginning location of the actuation region sp_1 plane for (a) $e = 0.01$, (b) $e = 0.02$, and (c) $e = 0.04$ with four identical piezoelectric patches. (d) A boundary between the stable and unstable equilibria for different end shortening cases. Open markers indicate the point at which the stable fourth-order equilibria switch from those that arise from one of the second-order branches to those that arise from the other. The closed markers denote the point above which the stable shapes nearest the stability boundary are second-order.

that arise from the other. The closed markers denote the point above which the stable shapes nearest the stability boundary are second-order. The value of sp_1 at which these points occur is insensitive to changes in end shortening.

6.3.2 Asymmetric Actuation Voltage

For the cases considered here, a positive voltage (with a corresponding actuation parameter, σ_1) is applied to the first and third patches while a negative voltage of a different magnitude (with a corresponding actuation parameter of σ_2) is applied to the second and fourth. Surface plots of normalized mid-point deflections versus σ_1 and σ_2 are shown in Fig. 6.15 for an end shortening of $e = 0.02$ and actuation regions of 10% to 90% and 20% to 80% of span. Stable and unstable equilibra are indicated with orange and magenta shaded regions, respectively.

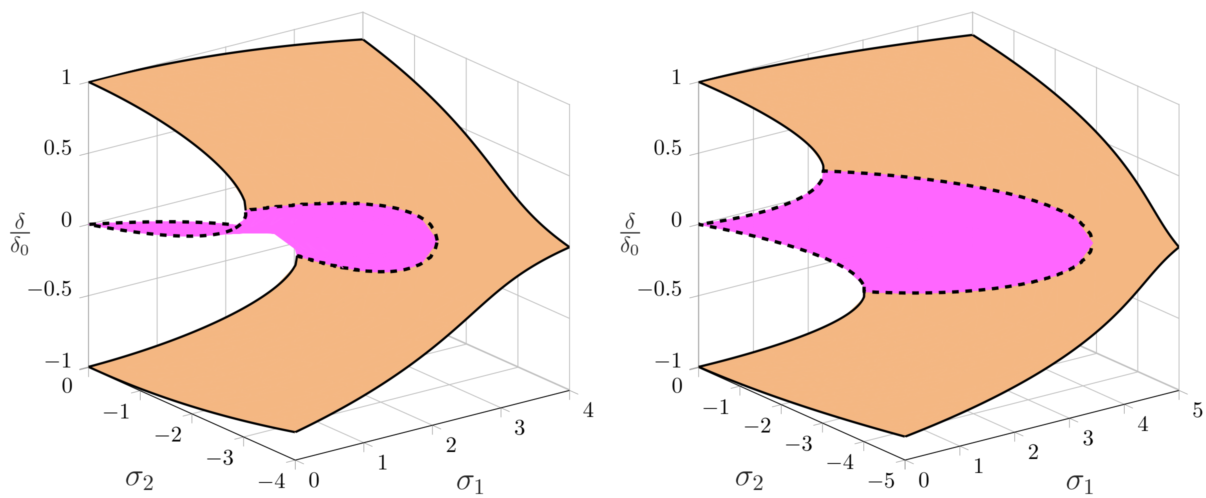

(a) (b)

Figure 6.15. Normalized mid-point deflection, δ/δ_0, versus non-dimensional electromechanical coupling terms, σ_1 and σ_2 for $e = 0.02$. The piezoelectric material is actuated from: (a) 10% to 90% of span; and (b) 20% to 80% of span. Orange (magenta) areas represent stable (unstable) equilibria and dashed lines indicate the boundary between stable and unstable equilibria.

Fig. 6.15 shows that two stable first-order equilibria and one unstable higher-order equlibrium coexist at low values of actuation voltages. When $|\sigma_1|$ or $|\sigma_2|$ is greater than a threshold value, a single stable equilibrium is present. A black dashed curve indicates the boundary between the stable and unstable equilibria. These and other stability boundaries projected on the σ_1-σ_2 plane are shown in Fig. 6.16. The cusps of the boundaries represent the minimum value of σ required to fully execute a stable transition given the present actuation scheme. The σ_1 and σ_2 values associated with these cusps increase monotonically as the actuation region reduces in length.

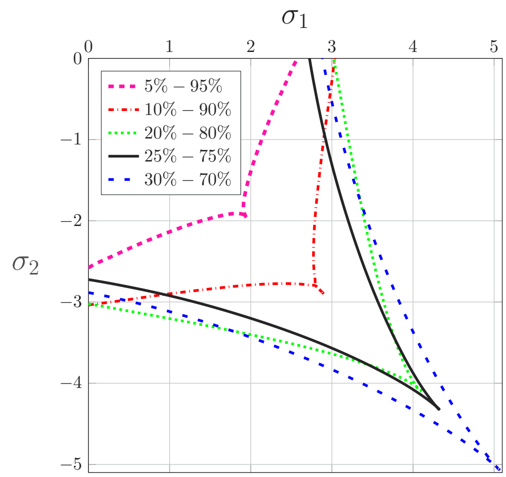

Figure 6.16. Boundaries between the stable and unstable equilibria for different actuation regions.

6.4 Experimental Validation

6.4.1 Experimental Setup

To validate the theoretical results and provide physical demonstrations of stable higher-order equilibrium shapes, an experiment is designed (see Fig. 6.17). The test article is a strip of spring steel ($\rho_s = 7700$ kg/m^3, $Y_s = 200$ GPa) with dimensions of 80 cm $\times$ 2 cm $\times$ 0.25 mm. Two 3D printed fixtures are affixed to the ends of the beam to simulate clamped-clamped boundary condition with a desired amount of end shortening. Three and four piezoelectric patches are bonded to the beam to obtain third- and fourth-order shapes, respectively. Each patch of P1-type MFC ($\rho_p = 5440$ kg/m^3, $Y_p = 30.34$ GPa, $d_{33} = 460$ pm/V) has an active dimension of 8.5 cm $\times$ 1.4 cm $\times$ 0.3 mm. Two patches are adhered to the front of the beam with epoxy, and the other(s) is (are) attached to the back. The frontside and backside patches are alternately distributed and are arranged symmetrically about the beam's midpoint. The MFC patches can be actuated with voltages up to 1500 volts using a high-voltage amplifier (Smart Materials AMT2012-CE3). The equilibrium shapes of the actuated beam are obtained using a high-resolution camera (JVC GC-PX100) and the edge of the beam is extracted using a custom image correlation process.

Since the MFC partially covers the beam, the beam's flexural rigidity is not constant along its length. An effective flexural rigidity is used to calculate the non-dimensional actuation parameter and enable a

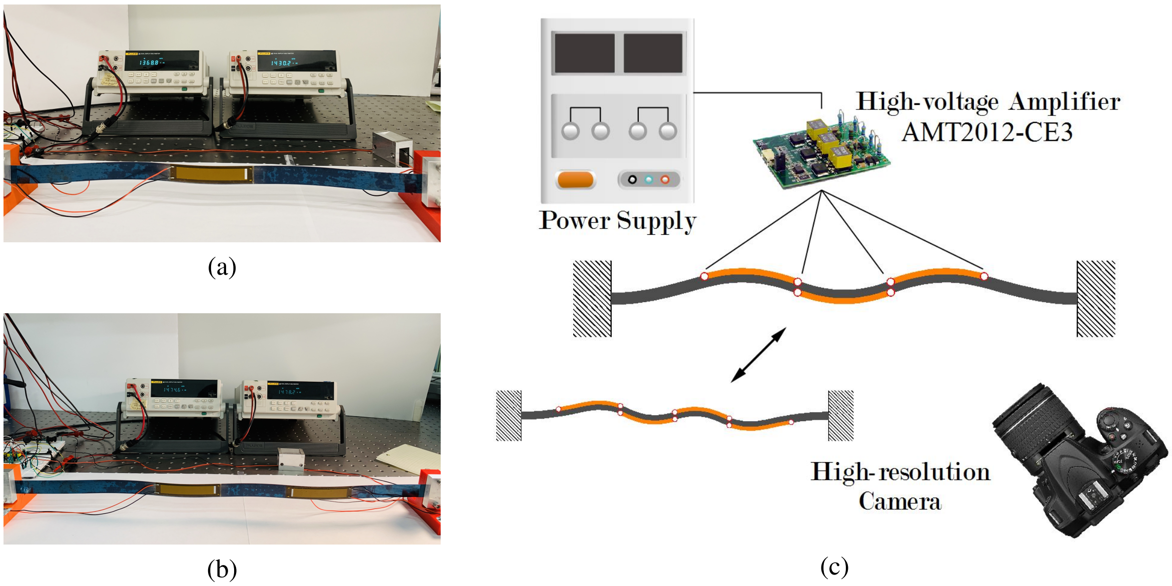

(a) (b) (c)

Figure 6.17. Experimental photos of a beam bonded with (a) three MFC and (b) four MFC. (c) Schematic of the experimental setup with three/ or four MFC patches alternately placed on both sides of the beam.

non-dimensionalization of the test results. The effective flexural rigidity is defined as

$$YI_{eff} = a_1 YI + a_2 YI_s, \tag{6.1}$$

where a_1 is the portion of the beam bonded with MFC, and a_2 is the portion without. The flexural rigidity of the substrate is given by $YI_s = Y_s b h_s^3/12$. Parameters corresponding to test articles bonded with three and four piezoelectric patches are shown in Table 6.1.

Table 6.1. Parameters for the unactuated test articles

Number of Patches	Three	Four
Patch span	15%-85%	20%-80%
End shortening e	0.02	0.01
Length l (cm)	43.7	63.9
Fraction of beam with MFC a_1	0.70	0.60
Effective flexural rigidity (Nm^{-2})	0.0134	0.0121
σ for $V = 1500$ volts	2.07	3.34

Positive voltages are applied to both the frontside and backside MFC patches. However, since the patches on the frontside and backside induce moments with opposite signs, a positive voltage on the frontside patches corresponds to a positive actuation parameter (σ_1) while a positive voltage on the backside patches corresponds to a negative actuation parameter (σ_2). Two different actuation region are considered—one from 15% to 80% of span and one from 20% to 80% of span. In both cases, voltages V_1 and V_2 are controlled separately. For the given configuration, σ values with a magnitude of less than approximately 3.5 are physically obtainable. Thus, relatively low end shortenings are used such that stable higher-order equilibrium shapes are achievable.

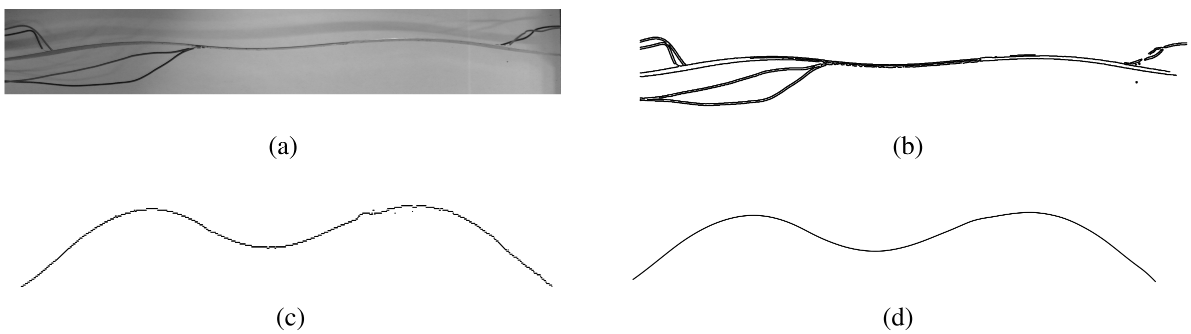

Figure 6.18. Image correlation process of a beam displaying a third-order equilibrium shape with $e = 0.02$, $V_1 = 1480$ volts and $V_2 = -1205$ volts. The piezoelectric material is actuated from 15% to 85% of span. (a) Gray-scale intensity image, (b) contour profile using Canny algorithm, (c) edge of the beam, and (d) final shape of the beam after 50 point moving average.

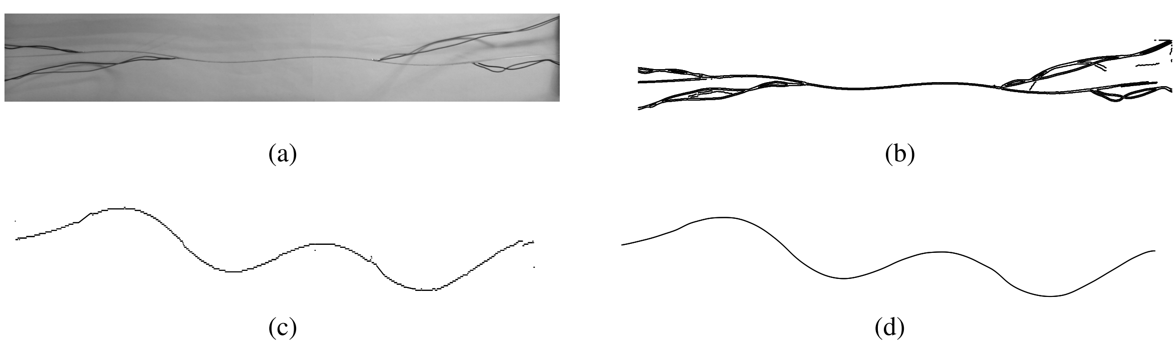

Figure 6.19. Image correlation process of a beam showing a fourth-order equilibrium shape with $e = 0.01$ and $V_1 = -V_2 = 1475$ volts. The piezoelectric material is actuated from 20% to 80% of span. (a) Gray-scale intensity image, (b) contour profile using Canny algorithm, (c) edge of the beam, and (d) final shape of the beam after 50 point moving average.

An image processing algorithm is used to digitize the beam's shape and extract mid-point deflections. Figs. 6.18 and 6.19 respectively show the main steps of image correlation process for the third- and fourth-order shapes of an unloaded and actuated beams. The steps of the image processing are described in more detail in Chapter 3, but in brief, true-color pictures (Figs. 6.18 and 6.19 (a)) are first converted to grayscale intensity images (Figs. 6.18 and 6.19 (b)), and the contour profile of the grayscale image is extracted using a Canny algorithm [125–127]. A user-defined filtering algorithm is then implemented to identify points corresponding to the edge of the beam while ignoring any extraneous points such as electrical wires (Figs. 6.18 and 6.19 (c)). The image of the beam's shape consists of upwards of 1800 digitized data points. To smooth out remaining noise in these data, a 50-point moving average is applied to give the final shape (Figs. 6.18 and 6.19 (d)).

6.4.2 Theoretical and Experimental Data Comparison

Fig. 6.20(a) shows the numerically-derived and normalized mid-point deflections versus σ_1 and σ_2 for $e = 0.02$. Sixteen points of experimental data are overlaid on the surface and indicate strong agreement with the numerical predictions. Three experimental points, denoted A, B, and C, are identified in the inset of part (a) and the corresponding experimental shapes are compared with the numerical prediction in Fig. 6.20(b).

Stable fourth-order equilibria are considered in Fig. 6.21 for an actuation region from 15% to 85% of span. The normalized mid-point deflection versus $|\sigma|$ for $e = 0.01$ is shown in Fig. 6.21(a) and is overlaid with experimental points. Select experimentally derived stable equilibrium shapes (denoted A, B, and C) are shown in Fig. 6.21(b) along with the corresponding numerical predictions. Point A is partway down the first-order branch and corresponds to an equilibrium shape that is a combination of the classical first- and fourth-order shapes. The first- and higher-order branch intersect near $|\sigma| = 2.9$. Since sp_1 in this case is less than 30%, the stable higher-order shape near the point of convergence is fourth-order (see Fig. 6.14). This fourth-order shape persists and becomes more stable with increasing levels of actuation.

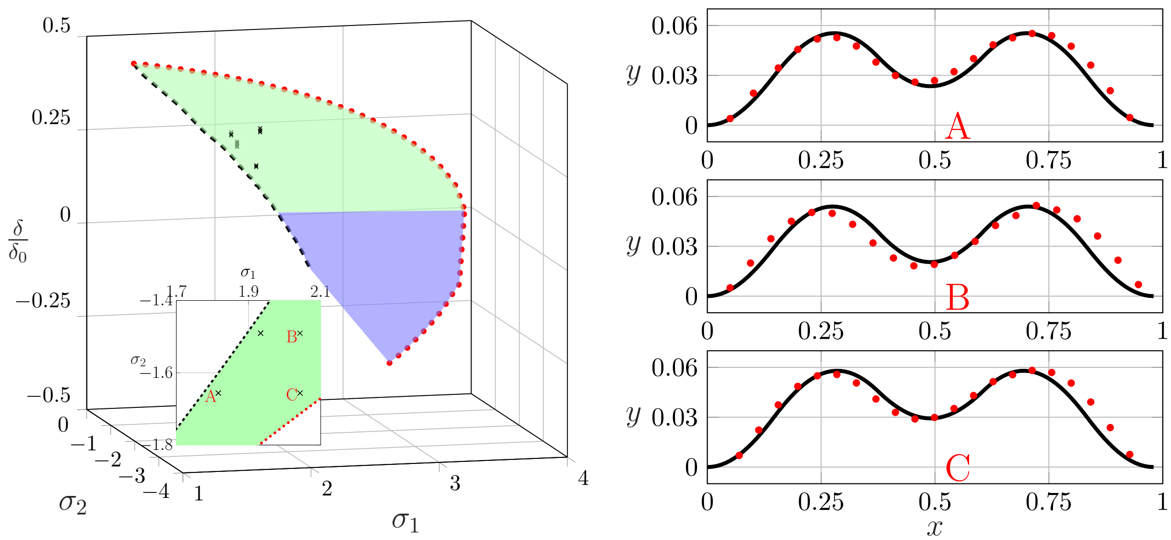

(a) (b)

Figure 6.20. (a) Normalized mid-point deflection, δ/δ_0, versus non-dimensional actuation parameters, σ_1 and σ_2, with the experimental data overlaid (markers). The inset in part (a) is a projection of stable third-order equilibria onto the σ_1-σ_2 plane. The piezoelectric material is actuated from 15% to 85% of span. (b) Numerical (solid line) and experimentally-derived (dots) equilibrium shape of point A ($\sigma_1 = 1.82$, $\sigma_2 = -1.66$), point B ($\sigma_1 = 2.04$, $\sigma_2 = -1.49$), and point C ($\sigma_1 = 2.04$, $\sigma_2 = -1.66$).

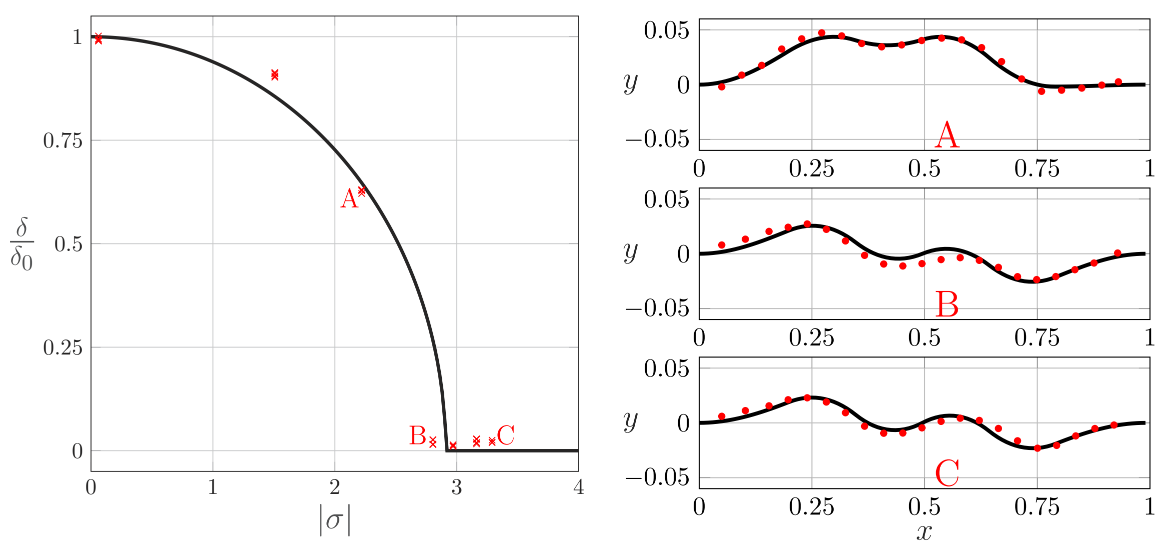

(a) (b)

Figure 6.21. (a) Normalized mid-point deflection, δ/δ_0, versus electromechanical coupling parameters, $|\sigma|$, with experimental data (markers). The piezoelectric material is actuated from 20% to 80% of span. (b) Numerical (solid lines) and experimentally-derived (dots) equilibrium shape of point A ($|\sigma| = 2.22$), point B ($|\sigma| = 2.88$), and point C ($|\sigma| = 3.29$).

6.5 Conclusions

This chapter investigates the viability of stabilizing the third- and fourth-order equilibria of post-buckled beams using piezoelectric actuation. Results indicate that by actuating several elongating piezoelectric patches, the beam can remain in certain positions of its third- and fourth-order equilibrium shapes at relatively high levels of σ. A range of possible actuation regions is also considered. Long actuation regions can lead to stable third-order shapes over relatively low and narrow ranges of σ, whereas shorter actuation regions need higher voltages to achieve third-order shapes. The required value of $|\sigma|$ to obtain fourth-order stable equilibria increases monotonically with deceasing actuation length. Experimental trials involving different actuation regions and voltages for beams with end shortening of $e = 0.01$ and 0.02 validate the theoretical results and physically demonstrate the stabilization of higher-order equilibria.

The results presented here can be used to inform the design of morphing composite structures and may be leveraged for aerospace applications or in adaptive optics. Another possibility is to embed piezoelectric actuators into biological or medical materials to morph an instrument into different configurations as needed. This chapter also considers new approaches for modeling electromechanical structures with multiple actuators. It is anticipated that these modeling efforts can contribute to research involving the exploitation or avoidance of snap-through instability in smart devices.

Chapter 7

Conclusions and Future Directions

7.1 Conclusions

In this dissertation, a series of problems related to circumventing snap-through instability in post-buckled structures have been addressed. One of the main contributions of this work is to build an extended elastica model accounting for the influence of piezoelectric actuation bonded to a post-buckled beam. This new electromechanically coupled framework models highly deformed piezoelectrically actuated structures and uses it to investigate their ability to resist or circumvent snap-through. The experiments presented here represent the first-ever physical demonstrations where piezoelectric actuation is used to increase critical snap-through loads or avoid the phenomenon altogether.

The extended elastica model presented here expresses the piezoelectric coupling effect in terms of a non-dimensional parameter, σ. This value can be calculated for candidate substrate/actuator configurations across a large parameter space to expose actuation strategies that change structural stability most profoundly. The model development begins with the bending moment of the composite beam, and then establishes the non-dimensional equilibrium equations. Static equilibria and their stability are computed using Runge-Kutta numerical integration and a shooting method. The potential energy of the composite is derived to provide another means of assessing the stability of the system.

Subsequently, four research topics are presented in the dissertation based on the piezo-elastica model:

- Theoretically and experimentally investigate the strategic actuation of piezoelectric material to change the loads required to initiate snap-through of clamped-clamped post-bucked beams.

- Study the possibility of using piezoelectric actuation to traverse stable transitions between remote equilibria, thus avoiding snap-through behavior altogether.
- Find the changes to natural frequencies and mode shapes of post-buckled beams during the stable transitions.
- Theoretically and experimentally identify actuation strategies that stabilize third- and fourth-order equilibrium shapes.

In the first topic, the model indicates that the effects of piezoelectric actuation manifest in the equilibrium equations in the same manner as an initial imperfection. Consequently, critical snap-through loads are found to increase linearly with increasing values of σ. Effects of piezoelectric actuation on critical snap-through load depend on the degree to which the beam is buckled, the location of the external load, the placement of the piezoelectric material, and the applied actuation voltage.

Next, in the second topic, the avoidance of snap-through instability is demonstrated by invoking stable transitions between remote equilibria. Through intelligent control of the two actuators, stable transitions between remote equilibria can be traversed, thus circumventing snap-through. The threshold for achieving stable transitions is given by σ_{cr}. The critical threshold increases monotonically as the beam end shortening increases. Given the limitations of existing piezoelectric actuators, stable transitions are only physically realizable in a subset of substrate/actuator configurations.

The third topic is an extension of the second one. It considers the natural frequencies and modes of the beams during the stable transitions. It is found that the direction of the beam's movement in the first two modes changes during a stable transition.

Finally, the fourth topic identifies and determines the stability of higher-order equilibrium shapes of clamped-clamped post-buckled beams under piezoelectric actuation. It is assumed that three or four piezoelectric patches are distributed along the beam. In certain situations, stable third- and fourth-order equilibrium shapes can be achieved with three and four piezoelectric patches, respectively.

7.2 Future Directions

Below are some potential avenues that could be pursued to extend this research.

7.2.1 Extension of Piezo-Elastica Model to Post-Buckled Beam

Preliminary theoretical results indicate that for shallow post-buckled beams (see Fig. 3.11) in certain configurations, the application of a constant voltage to surface piezoelectric material can increase the critical snap-through load by more than 150%, even after adjusting for the additional weight of the piezoelectric material. Increasing critical snap-through load has important implications for many engineering structures in which snap-through is to be avoided. To investigate this idea further, extension of piezo-elastica model of post-buckled beams are proposed.

Modeling: The piezo-elastica modeling approach outlined in Chapter 2 serves as a point of departure for exploring the mechanics of piezoelectrically actuated beams in a variety of configurations. An advantage of this formulation is that the modifications required to model the effects of extensibility, self-weight, initial imperfections, and various boundary conditions are well established. The extension of the model to account for these effects is planned. The piezo-elestica theory also does not place restrictions on rise angle, so deep arches (and even "S" curves and loops [74]) can be readily modeled. More complex extensions to the electromechanically coupled theory will also be pursued. These extensions, in order of priority, are:

1. **P2 type MFC:** The theory will be extended for use with the P2 (bending) type of MFC. Preliminary work on this suggests that P2 MFC is less effective at increasing snap-through loads than the P1 type. However, it is possible that P2 will be more effective in certain configurations, and it is important for the piezo-elastica theory to model either type, or a combination of both.

2. **Bimorphs:** Thus far, the piezo-elastica theory models the piezoelectric material on one side of the substrate. It is hypothesized that more dramatic increases in snap-through load are possible if material is on both sides. The model will be extended to account for this situation.

3. **Displacement control:** Preliminary results are based on a controlled external force. Alternatively, the displacement of a given point on the beam can be the control parameter. Under force control, snap-through occurs in a high force/small deflection condition. In displacement control, the asymmetric path that is unstable in the force controlled case becomes stable and the beam snaps through in a zero force/large deflection condition. It is hypothesized that piezoelectric actuation in the displacement controlled case will increase the deflection at the point of snap-through.

4. **Horizontal Snapping:** Under load, an beam typically assumes an asymmetric shape such that its highest point is shifted to one side of center. By applying a horizontal load in this condition, it is possible to make the beam snap horizontally such the highest point shifts to the other side of center. It is hypothesized that this type of snapping is more easily induced with piezoelectric actuation. If this is the case, it is then not difficult to envision the creation of novel low energy/high displacement actuators that exploit horizontal snapping. To explore this potential, the ability to model horizontal snapping will be incorporated into the piezo-elastica framework.

Parameter Studies: With the model extensions in place, a broad exploration of the configuration space is possible. Theoretical snap-through loads will be obtained for realistic values of σ, arch rise angles, boundary conditions, and piezoelectric patch configuration. For deep curved beams, the load-deflection behavior is quite rich, so it is likely that this relationship will not be straightforward. As discussed in Chapter 3, certain configurations yield increases in snap-through load that more than compensate for the weight introduced by the piezoelectric material. However, the degree to which this is true is highly configuration dependent, and a systematic parameter study will identify the configuration space over which piezoelectric actuation is a weight-advantageous strategy.

7.2.2 Changing Critical Snap-Through Loads of Post-Buckled Plates

Through an approach that involves modeling, parameter studies, optimization, and experiments, the fundamental features that affect piezoelectric stability enhancement in plates could be exposed.

Modeling: A theoretical model of post-buckled plates under quasi-static actuation from an arbitrary placement of piezoelectric patches could be developed. This could be accomplished by augmenting an approach in Ref. [65]. In that research, the von Kármán plate equations were solved using a Galerkin approximation for both the out-of-plane deflection and the Airy stress function. This resulted in a set of nonlinear ODEs that was solved using the AUTO continuation package [77] to determine equilibrium paths and stability. This approach could be expanded to account for electromechanical coupling. As with the piezo-elastica theory, system equations will be cast in non-dimensional terms to enable a more general investigation of the configuration space.

Parameter Studies: As with beams, an exploration of the configuration space could be conducted for piezoelectrically actuated post-buckled plates. Parameters to be varied include plate aspect ratio, in-plane loading, MFC type (P1 or P2), and the placement of the MFC patches.

Optimization: Given the two-dimensional nature of plates, it is hypothesized that certain—perhaps non-obvious—configurations of piezoelectric patches will be relatively more effective at changing critical snap-through loads. To identify these configurations, an optimization scheme can be wrapped around the snap-through analysis to identify desirable conditions. Objective functions that maximize the critical snap-through load, minimize the amount of piezoelectric material required to achieve a desired critical snap-through load, and/or minimize the amount of required actuation energy are all possible.

7.2.3 Avoidance of Snap-Through Instability of Post-Buckled Plates

Traversing stable paths between remote equilibria is an intriguing idea, and preliminary results raise a number of questions requiring deeper inquiry. Chapter 4 and 6 study stable transitions of post-buckled beams using several patches of P1 type MFC based on electromechanically coupled elastica model. Now, modeling and testing stable transitions between remote equilibria in post-buckled plates is much more complex.

Modeling: The electromechanically coupled Galerkin approach discussed previously could be adapted to model active control of the piezoelectronics. As with beams, multiple actuation strategies and topologies will be investigated to fully identify the conditions that give rise to stable transitions.

Optimization: With the expanded parameter space, optimization will be especially necessary in the analysis of plates. As with post-buckled beams, an optimization scheme will be wrapped around the model to identify maximally stable paths, minimal energy paths, and ideal actuator placements. Different unimorph and bimorph placements, MFC types, and actuation schemes will again be considered in the optimization.

Bibliography

[1] A. Pandey, D. E. Moulton, D. Vella, and D. P. Holmes, "Dynamics of snapping beams and jumping poppers," *EPL (Europhysics Letters)*, vol. 105, no. 2, p. 24001, 2014.

[2] C. F. Ng, "Nonlinear and snap-through responses of curved panels to intense acoustic excitation," *Journal of Aircraft*, vol. 26, no. 3, pp. 281–288, 1989.

[3] Y. Chandra, *Transient behavior of curved structures*. PhD thesis, Rice University, 2013.

[4] Y. Chandra, I. Stanciulescu, L. N. Virgin, T. G. Eason, and S. M. Spottswood, "A numerical investigation of snap-through in a shallow arch-like model," *Journal of Sound and Vibration*, vol. 332, no. 10, pp. 2532–2548, 2013.

[5] C. D. Hill, G. E. Blandford, and S. T. Wang, "Post-buckling analysis of steel space trusses," *Journal of Structural Engineering*, vol. 115, no. 4, pp. 900–919, 1989.

[6] M. R. Sheidaii, G. A. R. Parke, K. Abedi, and A. Behravesh, "Dynamic snap-through buckling of truss-type structures," *International Journal of Space Structures*, vol. 16, no. 2, pp. 85–93, 2001.

[7] I. M. Robertson, "Analytical calculations of fatigue loading of submarine hulls," Tech. Rep. MRL-TR-90-26, Materials Research Labs Ascot Vale (Australia), Nov 1990.

[8] J. R. MacKay, F. van Keulen, and M. J. Smith, "Quantifying the accuracy of numerical collapse predictions for the design of submarine pressure hulls," *Thin-Walled Structures*, vol. 49, no. 1, pp. 145–156, 2011.

[9] A. F. Arrieta, P. Hagedorn, A. Erturk, and D. Inman, "A piezoelectric bistable plate for nonlinear broadband energy harvesting," *Applied Physics Letters*, vol. 97, no. 10, p. 104102, 2010.

[10] C. Maurini, J. Pouget, and S. Vidoli, “Distributed piezoelectric actuation of a bistable buckled beam,” *European Journal of Mechanics-A/Solids*, vol. 26, no. 5, pp. 837–853, 2007.

[11] A. Fernandes, C. Maurini, and S. Vidoli, “Multiparameter actuation for shape control of bistable composite plates,” *International Journal of Solids and Structures*, vol. 47, no. 10, pp. 1449–1458, 2010.

[12] S. P. Timoshenko, “Buckling of flat curved bars and slightly curved plates,” *Journal of Applied Mechanics*, vol. 2, no. 1, pp. A17–A20, 1935.

[13] R. Levien, “The elastica: a mathematical history,” Tech. Rep. UCB/EECS-2008-103, University of California, Berkeley, Aug 2008.

[14] J. V. Huddleston, “Finite deflections and snap-through of high circular arches,” *Journal of Applied Mechanics*, vol. 35, no. 4, pp. 763–769, 1968.

[15] J. S. Chen and H. W. Tsao, “Dynamic snapping of a hinged extensible elastica under a step load,” *International Journal of Non-Linear Mechanics*, vol. 59, pp. 9–15, 2014.

[16] S. T. Santillan, *Analysis of the elastica with applications to vibration isolation*. PhD thesis, Duke University, 2007.

[17] R. B. Davis and M. D. McDowell, “Combined euler column vibration isolation and energy harvesting,” *Smart Materials and Structures*, vol. 26, no. 5, p. 055001, 2017.

[18] R. H. Plaut and L. N. Virgin, “Vibration and snap-through of bent elastica strips subjected to end rotations,” *Journal of Applied Mechanics*, vol. 76, no. 4, p. 041011, 2009.

[19] J. S. Chen and W. Z. Lin, “Dynamic snapping of a suddenly loaded elastica with fixed end slopes,” *International Journal of Non-Linear Mechanics*, vol. 47, no. 5, pp. 489–495, 2012.

[20] J.-S. Chen and J.-S. Lin, “Dynamic snap-through of a shallow arch under a moving point load,” *Journal of Vibration and Acoustics*, vol. 126, no. 4, pp. 514–519, 2004.

[21] K. Das and R. C. Batra, "Pull-in and snap-through instabilities in transient deformations of microelectromechanical systems," *Journal of Micromechanics and Microengineering*, vol. 19, no. 3, p. 035008, 2009.

[22] K. Das and R. C. Batra, "Symmetry breaking, snap-through and pull-in instabilities under dynamic loading of microelectromechanical shallow arches," *Smart Materials and Structures*, vol. 18, no. 11, p. 115008, 2009.

[23] H. M. Ouakad and M. I. Younis, "On using the dynamic snap-through motion of mems initially curved microbeams for filtering applications," *Journal of Sound and Vibration*, vol. 333, no. 2, pp. 555–568, 2014.

[24] M. I. Younis, H. M. Ouakad, F. M. Alsaleem, R. Miles, and W. Cui, "Nonlinear dynamics of MEMS arches under harmonic electrostatic actuation," *Journal of Microelectromechanical Systems*, vol. 19, no. 3, pp. 647–656, 2010.

[25] T. J. Beberniss and D. A. Ehrhardt, "High-speed 3D digital image correlation vibration measurement: Recent advancements and noted limitations," *Mechanical Systems and Signal Processing*, vol. 86, pp. 35–48, 2017.

[26] J. Qiu, J. H. Lang, and A. H. Slocum, "A curved-beam bistable mechanism," *Journal of Microelectromechanical Systems*, vol. 13, no. 2, pp. 137–146, 2004.

[27] T. E. Bruns and O. Sigmund, "Toward the topology design of mechanisms that exhibit snap-through behavior," *Computer Methods in Applied Mechanics and Engineering*, vol. 193, no. 36-38, pp. 3973–4000, 2004.

[28] R. L. Harne and K. W. Wang, "A review of the recent research on vibration energy harvesting via bistable systems," *Smart Materials and Structures*, vol. 22, no. 2, p. 023001, 2013.

[29] J. V. Huddleston, "Nonlinear analysis of steep, compressible arches of any shape," *Journal of Applied Mechanics*, vol. 38, no. 4, pp. 942–946, 1971.

[30] J. V. Huddleston, "A numerical technique for elastica problems," *Journal of the Engineering Mechanics Division*, vol. 94, no. 5, pp. 1159–1166, 1968.

[31] D. A. DaDeppo and R. Schmidt, “Large deflections and stability of hingeless circular arches under interacting loads.,” *Journal of Applied Mechanics*, vol. 41, no. 4, p. 989, 1974.

[32] C. Y. Wang, “A critical review of the heavy elastica,” *International Journal of Mechanical Sciences*, vol. 28, no. 8, pp. 549–559, 1986.

[33] A. Magnusson, M. Ristinmaa, and C. Ljung, “Behaviour of the extensible elastica solution,” *International Journal of Solids and Structures*, vol. 38, no. 46-47, pp. 8441–8457, 2001.

[34] J.-S. Chen and H.-W. Tsao, “Static snapping load of a hinged extensible elastica,” *Applied Mathematical Modelling*, vol. 37, no. 18-19, pp. 8401–8408, 2013.

[35] J. S. Chen and S. Y. Hung, “Snapping of an elastica under various loading mechanisms,” *European Journal of Mechanics-A/Solids*, vol. 30, no. 4, pp. 525–531, 2011.

[36] K. Das and R. C. Batra, “Symmetry breaking, snap-through and pull-in instabilities under dynamic loading of microelectromechanical shallow arches,” *Smart Materials and Structures*, vol. 18, no. 11, p. 115008, 2009.

[37] Y. Zhu and J. W. Zu, “Enhanced buckled-beam piezoelectric energy harvesting using midpoint magnetic force,” *Applied Physics Letters*, vol. 103, no. 4, p. 041905, 2013.

[38] Y. Zhu and J. Zu, “A magnet-induced buckled-beam piezoelectric generator for wideband vibration-based energy harvesting,” *Journal of Intelligent Material Systems and Structures*, vol. 25, no. 14, pp. 1890–1901, 2014.

[39] X.-Y. Jiang, H.-X. Zou, and W.-M. Zhang, “Design and analysis of a multi-step piezoelectric energy harvester using buckled beam driven by magnetic excitation,” *Energy Conversion and Management*, vol. 145, pp. 129–137, 2017.

[40] W. K. Wilkie, R. G. Bryant, J. W. High, R. L. Fox, R. F. Hellbaum, A. Jalink, B. D. Little, and P. H. Mirick, “Low-cost piezocomposite actuator for structural control applications,” in *Smart Structures and Materials 2000: Industrial and Commercial Applications of Smart Structures Technologies*, vol. 3991, pp. 323–335, International Society for Optics and Photonics, 2000.

[41] O. Bilgen, Y. Wang, and D. J. Inman, "Electromechanical comparison of cantilevered beams with multifunctional piezoceramic devices," *Mechanical Systems and Signal Processing*, vol. 27, pp. 763–777, 2012.

[42] H. A. Sodano, G. Park, and D. J. Inman, "An investigation into the performance of macro-fiber composites for sensing and structural vibration applications," *Mechanical Systems and Signal Processing*, vol. 18, no. 3, pp. 683–697, 2004.

[43] J. M. Lloyd, "Electrical properties of macro-fiber composite actuators and sensors," Master's thesis, Virginia Polytechnic Institute and State University, 2004.

[44] D.-K. Kim, H.-I. Kim, J.-H. Han, and K.-J. Kwon, "Experimental investigation on the aerodynamic characteristics of a bio-mimetic flapping wing with macro-fiber composites," *Journal of Intelligent Material Systems and Structures*, vol. 19, no. 3, pp. 423–431, 2008.

[45] R. Paradies and P. Ciresa, "Active wing design with integrated flight control using piezoelectric macro fiber composites," *Smart Materials and Structures*, vol. 18, no. 3, p. 035010, 2009.

[46] Y. Yang, L. Tang, and H. Li, "Vibration energy harvesting using macro-fiber composites," *Smart Materials and Structures*, vol. 18, no. 11, p. 115025, 2009.

[47] O. Bilgen, K. Kochersberger, E. Diggs, A. Kurdila, and D. Inman, "Morphing wing micro-air-vehicles via macro-fiber-composite actuators," in *48th AIAA/ASME/ASCE/AHS/ASC Structures, Structural Dynamics, and Materials Conference*, p. 1785, 2007.

[48] F. Lanza Discalea, H. Matt, I. Bartoli, S. Coccia, G. Park, and C. Farrar, "Health monitoring of UAV wing skin-to-spar joints using guided waves and macro fiber composite transducers," *Journal of Intelligent Material Systems and Structures*, vol. 18, no. 4, pp. 373–388, 2007.

[49] H. Wang and L. Tang, "Modeling and experiment of bistable two-degree-of-freedom energy harvester with magnetic coupling," *Mechanical Systems and Signal Processing*, vol. 86, pp. 29–39, 2017.

[50] S. M. Corp., "MFC–MicroFiberComposite." https://www.smart-material.com/index.html, 2020. Online; modified March 22, 2020.

[51] S. M. Jung and K. S. Yun, "A wideband energy harvesting device using snap-through buckling for mechanical frequency-up conversion," in *2010 IEEE 23rd International Conference on Micro Electro Mechanical Systems (MEMS)*, pp. 1207–1210, IEEE, 2010.

[52] D. N. Betts, H. A. Kim, C. R. Bowen, and D. J. Inman, "Optimal configurations of bistable piezo-composites for energy harvesting," *Applied Physics Letters*, vol. 100, no. 11, p. 114104, 2012.

[53] A. J. Sneller, P. Cette, and B. P. Mann, "Experimental investigation of a post-buckled piezoelectric beam with an attached central mass used to harvest energy," *Proceedings of the Institution of Mechanical Engineers, Part I: Journal of Systems and Control Engineering*, vol. 225, no. 4, pp. 497–509, 2011.

[54] W. A. Jiang and L. Q. Chen, "Snap-through piezoelectric energy harvesting," *Journal of Sound and Vibration*, vol. 333, no. 18, pp. 4314–4325, 2014.

[55] C. Xu, Z. Liang, B. Ren, W. Di, H. Luo, D. Wang, K. Wang, and Z. Chen, "Bi-stable energy harvesting based on a simply supported piezoelectric buckled beam," *Journal of Applied Physics*, vol. 114, no. 11, p. 114507, 2013.

[56] A. Syta, C. R. Bowen, H. A. Kim, A. Rysak, and G. Litak, "Responses of bistable piezoelectric-composite energy harvester by means of recurrences," *Mechanical Systems and Signal Processing*, vol. 76, pp. 823–832, 2016.

[57] A. J. Lee and D. J. Inman, "A multifunctional bistable laminate: Snap-through morphing enabled by broadband energy harvesting," *Journal of Intelligent Material Systems and Structures*, vol. 29, no. 11, pp. 2528–2543, 2018.

[58] F. Dai and D. Pan, "Piezoelectric energy harvesting based on bi-stable composite laminate," in *Energy Harvesting* (R. Manyala, ed.), ch. 5, p. 63, London: IntechOpen, 2018.

[59] S. A. Emam and D. J. Inman, "A review on bistable composite laminates for morphing and energy harvesting," *Applied Mechanics Reviews*, vol. 67, no. 6, p. 060803, 2015.

[60] M. R. Schultz and M. W. Hyer, “Snap-through of unsymmetric cross-ply laminates using piezoceramic actuators,” *Journal of Intelligent Material Systems and Structures*, vol. 14, no. 12, pp. 795–814, 2003.

[61] M. R. Schultz, M. W. Hyer, R. B. Williams, W. K. Wilkie, and D. J. Inman, “Snap-through of unsymmetric laminates using piezocomposite actuators,” *Composites Science and Technology*, vol. 66, no. 14, pp. 2442–2448, 2006.

[62] P. Cazottes, A. Fernandes, J. Pouget, and M. Hafez, “Actuation of bistable buckled beams with macro-fiber composites,” in *Intelligent Robots and Systems, 2008. IROS 2008. IEEE/RSJ International Conference on*, pp. 564–569, IEEE, 2008.

[63] M. R. Schultz and M. W. Hyer, “A morphing concept based on unsymmetric composite laminates and piezoceramic MFC actuators,” in *45 th AIAA/ASME/ASCE/AHS/ASC Structures, Structural Dynamics and Materials Conference*, vol. 1806, pp. 19–22, ARC, 2004.

[64] C. R. Bowen, R. Butler, R. Jervis, H. A. Kim, and A. T. Salo, “Morphing and shape control using unsymmetrical composites,” *Journal of Intelligent Material Systems and Structures*, vol. 18, no. 1, pp. 89–98, 2007.

[65] C. G. Diaconu, P. M. Weaver, and F. Mattioni, “Concepts for morphing airfoil sections using bi-stable laminated composite structures,” *Thin-Walled Structures*, vol. 46, no. 6, pp. 689–701, 2008.

[66] D. V. Murray and O. J. Myers, “Modeling bistable composite laminates for piezoelectric morphing structures,” *ISRN Materials Science*, vol. 2013, p. 428624, 2013.

[67] A. F. Arrieta, O. Bilgen, M. I. Friswell, and P. Hagedorn, “Dynamic control for morphing of bi-stable composites,” *Journal of Intelligent Material Systems and Structures*, vol. 24, no. 3, pp. 266–273, 2013.

[68] Z. Zhang, Y. Li, X. Yu, X. Li, H. Wu, H. Wu, S. Jiang, and G. Chai, “Bistable morphing composite structures: A review,” *Thin-Walled Structures*, vol. 142, pp. 74–97, 2019.

[69] N. Hu and R. Burgueño, “Buckling-induced smart applications: recent advances and trends,” *Smart Materials and Structures*, vol. 24, no. 6, p. 063001, 2015.

[70] S. M. Corp., “MFC P1, F1 and S1 types (d33 effect), Elongator.” https://www.smart-material.com/MFC-product-P1.html, 2020. Online; modified February 19, 2020.

[71] A. F. Arrieta, D. J. Wagg, and S. A. Neild, “Dynamic snap-through for morphing of bi-stable composite plates,” *Journal of Intelligent Material Systems and Structures*, vol. 22, no. 2, pp. 103–112, 2011.

[72] G. Giannopoulos, J. Monreal, and J. Vantomme, “Snap-through buckling behavior of piezoelectric bimorph beams: I. analytical and numerical modeling,” *Smart Materials and Structures*, vol. 16, no. 4, p. 1148, 2007.

[73] G. Giannopoulos, J. Monreal, and J. Vantomme, “Snap-through buckling behavior of piezoelectric bimorph beams: II. experimental verification,” *Smart Materials and Structures*, vol. 16, no. 4, p. 1158, 2007.

[74] S. Sridharan and S. Kim, “Piezoelectric control of columns prone to instabilities and nonlinear modal interaction,” *Smart Materials and Structures*, vol. 17, no. 3, p. 035001, 2008.

[75] J.-S. Park and J.-H. Kim, “Suppression of aero-thermal large deflections and snap-through behaviors of composite panels using macro fiber composite actuators,” *Smart Materials and Structures*, vol. 13, no. 6, p. 1448, 2004.

[76] S. Aimmanee and K. Tichakorn, “Piezoelectrically induced snap-through buckling in a buckled beam bonded with a segmented actuator,” *Journal of Intelligent Material Systems and Structures*, vol. 29, no. 9, pp. 1862–1874, 2018.

[77] T. C. Lyman, L. N. Virgin, and R. B. Davis, “Application of continuation methods to uniaxially loaded postbuckled plates,” *Journal of Applied Mechanics*, vol. 81, no. 3, p. 031010, 2014.

[78] D. N. Betts, H. A. Kim, and C. R. Bowen, “Modeling and optimization of bistable composite laminates for piezoelectric actuation,” *Journal of Intelligent Material Systems and Structures*, vol. 22, no. 18, pp. 2181–2191, 2011.

[79] C. R. Bowen, P. F. Giddings, A. I. Salo, and H. A. Kim, “Modeling and characterization of piezoelectrically actuated bistable composites,” *IEEE Transactions on Ultrasonics, Ferroelectrics, and Frequency Control*, vol. 58, no. 9, pp. 1737–1750, 2011.

[80] A. J. Lee, A. Moosavian, and D. J. Inman, “Control and characterization of a bistable laminate generated with piezoelectricity,” *Smart Materials and Structures*, vol. 26, no. 8, p. 085007, 2017.

[81] A. F. Arrieta, V. van Gemmeren, A. J. Anderson, and P. M. Weaver, “Dynamics and control of twisting bi-stable structures,” *Smart Materials and Structures*, vol. 27, no. 2, p. 025006, 2018.

[82] S. Zareie, A. Zabihollah, and A. Azizi, “Buckling control of morphing composite airfoil structure using multi-stable laminate by piezoelectric sensors/actuators,” in *Behavior and Mechanics of Multifunctional Materials and Composites 2011*, vol. 7978, p. 79781Z, International Society for Optics and Photonics, 2011.

[83] R. Vos, R. Barrett, R. de Breuker, and P. Tiso, “Post-buckled precompressed elements: a new class of control actuators for morphing wing UAVs,” *Smart Materials and Structures*, vol. 16, no. 3, p. 919, 2007.

[84] R. Vos, R. D. Breuker, R. M. Barrett, and P. Tiso, “Morphing wing flight control via postbuckled precompressed piezoelectric actuators,” *Journal of Aircraft*, vol. 44, no. 4, pp. 1060–1068, 2007.

[85] R. W. Roe and U. N. Gandhi, “Smart material trailing edge variable chord morphing wing,” Oct. 4 2016. U.S. Patent 9,457,887.

[86] F. Nicassio, G. Scarselli, F. Pinto, F. Ciampa, O. Iervolino, and M. Meo, “Low energy actuation technique of bistable composites for aircraft morphing,” *Aerospace Science and Technology*, vol. 75, pp. 35–46, 2018.

[87] R. Vos, R. Barrett, and D. Zehr, “Magnification of work output in PBP class actuators using buckling/converse buckling techniques,” in *49th AIAA/ASME/ASCE/AHS/ASC Structures, Structural Dynamics, and Materials Conference*, p. 1705, Aerospace Research Central, 2008.

[88] H. T. Pham and D. A. Wang, "A quadristable compliant mechanism with a bistable structure embedded in a surrounding beam structure," *Sensors and Actuators A: Physical*, vol. 167, no. 2, pp. 438 – 448, 2011.

[89] F. Dai, H. Li, and S. Du, "A multi-stable lattice structure and its snap-through behavior among multiple states," *Composite Structures*, vol. 97, pp. 56 – 63, 2013.

[90] N. Lajnef, R. Burgueño, W. Borchani, and Y. Sun, "A concept for energy harvesting from quasi-static structural deformations through axially loaded bilaterally constrained columns with multiple bifurcation points," *Smart Materials and Structures*, vol. 23, no. 5, p. 055005, 2014.

[91] A. Pirrera, X. Lachenal, S. Daynes, P. M. Weaver, and I. V. Chenchiah, "Multi-stable cylindrical lattices," *Journal of the Mechanics and Physics of Solids*, vol. 61, no. 11, pp. 2087–2107, 2013.

[92] S. J. Hwang and N. C. Perkins, "Supercritical stability of an axially moving beam part i: model and equilibrium analysis," *Journal of Sound and Vibration*, vol. 154, no. 3, pp. 381–396, 1992.

[93] S. J. Hwang and N. C. Perkins, "Supercritical stability of an axially moving beam part ii: vibration and stability analyses," *Journal of Sound and Vibration*, vol. 154, no. 3, pp. 397–409, 1992.

[94] J. Wickert, "Non-linear vibration of a traveling tensioned beam," *International Journal of Non-Linear Mechanics*, vol. 27, no. 3, pp. 503–517, 1992.

[95] D. W. Raboud, A. W. Lipsett, M. G. Faulkner, and J. Diep, "Stability evaluation of very flexible cantilever beams," *International journal of non-linear mechanics*, vol. 36, no. 7, pp. 1109–1122, 2001.

[96] A. H. Nayfeh and S. A. Emam, "Exact solution and stability of postbuckling configurations of beams," *Nonlinear Dynamics*, vol. 54, no. 4, pp. 395–408, 2008.

[97] S. A. Emam and A. H. Nayfeh, "Postbuckling and free vibrations of composite beams," *Composite Structures*, vol. 88, no. 4, pp. 636–642, 2009.

[98] H. Sehitoglu and M. Karasek, "Observations of material behavior under isothermal and thermo-mechanical loading," *Journal of Engineering Materials and Technology*, vol. 108, no. 2, pp. 192–198, 1986.

[99] J. A. Shaw, “Simulations of localized thermo-mechanical behavior in a NiTi shape memory alloy,” *International journal of plasticity*, vol. 16, no. 5, pp. 541–562, 2000.

[100] T. Murmu and S. C. Pradhan, “Thermo-mechanical vibration of a single-walled carbon nanotube embedded in an elastic medium based on nonlocal elasticity theory,” *Computational Materials Science*, vol. 46, no. 4, pp. 854–859, 2009.

[101] F. Pitié, C. Y. Zhao, and G. Caceres, “Thermo-mechanical analysis of ceramic encapsulated phase-change-material (PCM) particles,” *Energy & Environmental Science*, vol. 4, no. 6, pp. 2117–2124, 2011.

[102] S. Narendar and S. Gopalakrishnan, “Critical buckling temperature of single-walled carbon nanotubes embedded in a one-parameter elastic medium based on nonlocal continuum mechanics,” *Physica E: Low-dimensional Systems and Nanostructures*, vol. 43, no. 6, pp. 1185–1191, 2011.

[103] C.-Y. Lee and J.-H. Kim, “Thermal post-buckling and snap-through instabilities of FGM panels in hypersonic flows,” *Aerospace Science and Technology*, vol. 30, no. 1, pp. 175–182, 2013.

[104] Z. Zhang, G. Ye, H. Wu, H. Wu, D. Chen, and G. Chai, “Thermal effect and active control on bistable behaviour of anti-symmetric composite shells with temperature-dependent properties,” *Composite Structures*, vol. 124, pp. 263–271, 2015.

[105] A. Przekop and S. A. Rizzi, “Dynamic snap-through of thin-walled structures by a reduced-order method,” *AIAA journal*, vol. 45, no. 10, pp. 2510–2519, 2007.

[106] M. Mirzaei and Y. Kiani, “Snap-through phenomenon in a thermally postbuckled temperature dependent sandwich beam with FG-CNTRC face sheets,” *Composite Structures*, vol. 134, pp. 1004–1013, 2015.

[107] F. Mattioni, P. M. Weaver, K. D. Potter, and M. I. Friswell, “Analysis of thermally induced multistable composites,” *International Journal of Solids and Structures*, vol. 45, no. 2, pp. 657–675, 2008.

[108] I. Stanciulescu, T. Mitchell, Y. Chandra, T. Eason, and M. Spottswood, “A lower bound on snap-through instability of curved beams under thermomechanical loads,” *International Journal of Non-Linear Mechanics*, vol. 47, no. 5, pp. 561–575, 2012.

[109] E. Eckstein, A. Pirrera, and P. M. Weaver, “Thermally driven morphing and snap-through behavior of hybrid laminate shells,” *AIAA Journal*, vol. 54, no. 5, pp. 1778–1788, 2016.

[110] J. H. Kweon and C. S. Hong, “An improved arc-length method for postbuckling analysis of composite cylindrical panels,” *Computers & Structures*, vol. 53, no. 3, pp. 541–549, 1994.

[111] R. De Borst, M. A. Crisfield, J. J. C. Remmers, and C. V. Verhoosel, *Nonlinear finite element analysis of solids and structures*. John Wiley & Sons, 2012.

[112] M. L. Dano, M. Gakwaya, and B. Jullière, “Compensation of thermally induced distortion in composite structures using macro-fiber composites,” *Journal of Intelligent Material Systems and Structures*, vol. 19, no. 2, pp. 225–233, 2008.

[113] M. L. Dano and B. Jullière, “Active control of thermally induced distortion in composite structures using macro fiber composite actuators,” *Smart Materials and Structures*, vol. 16, no. 6, p. 2315, 2007.

[114] S. G. O’Keeffe, D. E. Moulton, S. L. Waters, and A. Goriely, “Growth-induced axial buckling of a slender elastic filament embedded in an isotropic elastic matrix,” *International Journal of Non-Linear Mechanics*, vol. 56, pp. 94–104, 2013.

[115] M. Brissaud, S. Ledren, and P. Gonnard, “Modelling of a cantilever non-symmetric piezoelectric bimorph,” *Journal of Micromechanics and Microengineering*, vol. 13, no. 6, p. 832, 2003.

[116] A. Erturk and D. J. Inman, *Piezoelectric energy harvesting*. John Wiley & Sons, 2011.

[117] A. Erturk, O. Bilgen, M. Fontenille, and D. J. Inman, “Piezoelectric energy harvesting from macro-fiber composites with an application to morphing-wing aircrafts,” in *19th International Conference on Adaptive Structures and Technologies 2008, ICAST 2008*, pp. 339–359, Citeseer, 2008.

[118] L. N. Virgin, *Vibration of axially-loaded structures*. Cambridge University Press, 2007.

[119] S. P. Timoshenko and J. M. Gere, *Theory of elastic stability*. Courier Corporation, 2009.

[120] P. Patricio, M. Adda-Bedia, and M. B. Amar, “An elastica problem: instabilities of an elastic arch,” *Physica D: Nonlinear Phenomena*, vol. 124, no. 1-3, pp. 285–295, 1998.

[121] J. E. Sidbury, “Analysis of buckled and pre-bent columns used as vibration isolators,” Master’s thesis, Virginia Tech, 2003.

[122] J. Lemaitre and J.-L. Chaboche, *Mechanics of solid materials*. Cambridge University Press, 1994.

[123] “MFC Engineering Properties.” https://www.smart-material.com/MFC-product-properties.html.

[124] R. H. Plaut, “Influence of load position on the stability of shallow arches,” *Zeitschrift für angewandte Mathematik und Physik ZAMP*, vol. 30, no. 3, pp. 548–552, 1979.

[125] J. Canny, “A computational approach to edge detection,” in *Readings in Computer Vision* (M. A. Fischler and O. Firschein, eds.), pp. 184–203, San Francisco (CA): Morgan Kaufmann, 1987.

[126] J. S. Lim, *Two-dimensional signal and image processing*. Englewood Cliffs: Prentice Hall, 1990.

[127] J. R. Parker, *Algorithms for image processing and computer vision*. John Wiley & Sons, 2010.

[128] A. Deraemaeker, H. Nasser, A. Benjeddou, and A. Preumont, “Mixing rules for the piezoelectric properties of macro fiber composites,” *Journal of Intelligent Material Systems and Structures*, vol. 20, no. 12, pp. 1475–1482, 2009.

[129] L. Meirovitch, *Principles and techniques of vibrations*, vol. 1. Prentice Hall, 1997.

[130] H. Xiu and R. B. Davis, “Stable transitions between remote equilibria of post-buckled beams using piezoelectric actuation,” *Smart Materials and Structures*, vol. 28, no. 11, p. 115007, 2019.

[131] C. W. De Silva, *Vibration: fundamentals and practice*. CRC press, 2006.

[132] M. Pastor, M. Binda, and T. Harčarik, “Modal assurance criterion,” *Procedia Engineering*, vol. 48, pp. 543–548, 2012.